博士学位论文
DOCTORAL DISSERTATION

博 士 学 位 论 文

在RHIC能区质子-质子和金-金原子核对撞中重味夸克产额

论文作者： 白晓智

指导教师： 杨纯斌，叶震宇

申请学位： 理学博士

专业名称： 理论物理

研究方向： 重味物理

华中师范大学物理科学与技术学院

二零一七年五月

博士学位论文
DOCTORAL DISSERTATION

A Dissertation for Doctor of Philosophy in Physics

Measurements of open heavy flavor production in p+p and Au+Au collisions at RHIC energy

by

Xiaozhi Bai

Supervisor: Chunbin Yang, Zhenyu Ye
Specialty: Theoretical Physics
Research Area: Heavy Flavor (Quark and Nuclear Matter) Physics

College of Physical Science and Technology

Central China Normal University

May 2017

原创性声明

本人郑重声明：本人所呈交的学位论文，是在导师的指导下独立进行研究所取得的成果。学位论文中凡引用他人已经发表或未发表的成果、数据、观点等，均已明确注明出处。除稳重已经注明引用的内容外，不包含任何其他个人或集体已经发表或撰写过的研究成果。对本文的研究成果做出重要贡献的个人和集体，均已在论文中以明确方式标明。

本声明的法律结果由本人承担。

论文作者签名：　　　　日期：

摘 要

相对论重离子碰撞的一个主要目的是研究在非常高的温度和能量密度下，解禁闭的夸克和胶子等离子体（QGP)的形式和性质，以及它们和硬部分子之间的相互作用。位于布鲁克海文国家实验室（BNL）的相对论重离子对撞机（RHIC）和欧洲的大型强子对撞机（LHC）的实验结果表明，这种新的物质形态可以通过超高能相对论重离子碰撞产生。但是在实验上很难直接观察这种新的物质形态，因为夸克和胶子带色荷，因此它们会禁闭在强子内部。在实验上观测到的是末态的冷却的粒子，这种末态的粒子受到冷核和热核效应的影响，所以很难从末态粒子观测早期的QGP的演化过程。

重夸克被认为是研究QGP的完美探针，因为它们在重离子碰撞初期通过部分子的硬散射过程产生，而且质量很大，在RHIC能级下很难在QGP的演化中再产生。因此重夸克携带了系统的早期阶段的碰撞信息和QGP的热介质信息。在系统的演化过程中，重味夸克穿过介质并且和QGP相互作用，因此重夸克的性状中携带有QGP演化的信息，因此精确地分别测量charm 夸克和bottom 夸克的产额对于理解重夸克与介质的相互作用，以及介质的性质，部分子的能量损失机理是非常重要的。

由于重味夸克质量（charm和bottom夸克，$m_c \approx 1.3$ GeV/c^2 and $m_b \approx 4.2$ GeV/c^2）远高于量子色动力学QCD标度（大约200 MeV），所以重味夸克的产生过程伴随着较高的横动量转移。由于QCD的渐近自由，这个过程可以很好地用微扰QCD描述。在试验中精确的测量重味夸克的产生可以很好地检验微扰QCD计算，而且为模型计算提供较准确的参数。

在2014年，STAR实验组安装了一个重味夸克劲迹探测器（HFT），这是一个新的硅探测器，具有非常好的位置分辨率用于测量衰变顶点和碰撞顶点之间的最近距离（DCA）。由于charm 和bottom强子的寿命不一样,通过DCA的差异，就能够分开charm 和bottom强子半轻子衰变产生的电子。半轻子衰变道可以通过测量重味介子衰变产生的电子来测量重味夸克，尽管这是一种间接测量的办法，但也是一种非常有效的测量方法。在RHIC能区下重味夸克的产生截面比较小，所以测量一直受统计量的影响。和强子衰变道相比，半轻子衰变道衰变的电子有较好的统计量。在本论文中，除非有特别说明，所有的电子包括正电子和负电子。

我们最新的实验数据是在质心系200 GeV质子-质子对撞中charm 和bottom强子半

轻子衰变产生的电子的产额，分析结果和微扰QCD的次领头阶（FONLL）计算在误差范围内一致。电子在质子-质子对撞的产额可以作为原子核对撞电子产额的基线，来研究热部分子在高温高密的介质中的能量损失。我们测量结果表明，非光电子的核修正因子在所有的中心度区间，高横动量（4 GeV/c < p_{T} ）范围有比较大的压低，且压低随着中心度的增加而不断减少，在低横动量区间核修正因子有加强，但是系统误差很大。我们分别测量了charm 和bottom强子通过半轻子衰变道产生的电子在质心系200 GeV金-金对撞的产额。本次测量结果表明bottom强子半轻子衰变产生的电子的核修正因子压低比charm强子衰变产生的电子要小，这一结果被认为bottom夸克和charm夸克相比，在热部分子中损失的能量要小。

关键词： 相对论重离子碰撞，质子质子对撞，量子色动力学（QCD），夸克胶子等离子体, 重味物理，半轻子衰变

Abstract

The primary motivation for relativistic heavy-ion collisions is to study the formation of theoretically predicted plasma of deconfined quarks and gluons (QGP) and the properties of the strongly interacting matter at extremely high temprature and energy density. Both the Relativistic Heavy Ion Collider (RHIC) at Brookhaven National Laboratory (BNL) and the Large Hadron Collider (LHC) experimental results suggest that such matter could be created in the relativistic heavy-ion collisions, however, such a medium can not be directly observed in the experiment, since the quarks and gluons with the color charges and can not exist from others, therefore, they can not be directly observed in the experiment, the only observation is the final state chemical freeze-out particles, however, the final states particles are affected by both the initial and final states nuclear matter effects.

Heavy flavor quarks are suggested to be an excellent probe of the QGP, because they are produced very early in the heavy-ion collisions, therefore they carry the information about the early stages of the system evolution. They are expected to interact with the QGP differently from light quarks and their production is sensitive to the dynamics of the mediums. Measurements of the charm and bottom quark production are crucial for understanding the nature of interactions of heavy quarks with the surrounding partonic medium, and the partons energy loss mechanism. Precise measurements of charm and bottom quark production separately in heavy-ion collisions is crucial for understanding the flavor dependent parton energy loss mechanism, and improve our understanding of the properties of the QGP.

Because heavy quarks masses (charm and bottom quarks, $m_c \approx 1.3$ GeV$/c^2$ and $m_b \approx 4.2$ GeV$/c^2$) are much higher than the typical QCD scale 200 MeV, heavy flavor quarks production is expected to be well described by the perturbative QCD. High precision measurements of heavy flavor production in proton-proton collisions are instrumental to test the validity and constrain the parameters of perturbative QCD calculations.

The Heavy Flavor Tracker (HFT), installed at the STAR experiment since 2014, pro-

vides excellent resolution to measure the Distance of Closest Approach (DCA) between primavry vertices and secondary decay vertex. It enables the separation of non-photonic electron (NPE) produced from D- and B-meson decays. Electrons from semi-leptonic decays of heavy flavor hadrons (non-photonic electrons, NPE) are good proxies for heavy quarks. Although the kinematics information of parent heavy flavor hardrons is incomplete, NPE is still the most feasible tool so far to study heavy quark production at RHIC energies, especially at high p_{T} , and dedicated triggers for such electrons can be used in the experiment to largely enhance the statistics. Unless specified otherwise, electrons referred here include both electrons and positrons.

The latest data analysis results extend the p_{T} coverage to lower and higher values than previous STAR measurements with significantly better precision is consistent with the FONLL calculations, moreover,it provides a baseline for the interpretation of heavy flavor production in nucleus-nucleus collisions. The measured nuclear modification factors R_{AA} indicate an significant suppression at $p_{\mathrm{T}} > 4$ GeV/c in the most central Au+Au collisions, and reduces gradually towards more peripheral collisions, enhancement at low p_{T} across all centrality bins but with large systematic uncertainties. Nuclear modification factors R_{AA} for D- and B-decayed electrons are obtained, suggesting less suppression for B-decayed electrons than D-decayed electrons and consistent with the mass hirechy of parton energy loss $\Delta E_b < \Delta E_c$.

Keywords: Relativistic heavy-ion collision, Quantum chromodynamics (QCD), Quark gluon plasma, Heavy flavor physics, Semi-lepton decay

Table of Contents

Presentations and publication List 118

List of Figures

List of Tables

CHAPTER 1

Introduction

1.1 Introduction to Quantum Chromodynamics

What is the fundamental particles in our universe? How do these particles interact with each other? The answers to these questions can be found in the standard model of particle physics. Up to now, as we all know, 12 fundamental particles have been discovered: six quarks and six leptons showing on Fig. 1.1. Quarks are suggested be to the fundamental elementary building blocks of the universe. As shown in Fig. 1.1, there are six different quarks and leptons: up, down, charm, strange, top, and bottom, their mass increases from left to the right and their charge are +2/3 of an electron's charge in the top row, in the second row, their charges are -1/3 of electron's charge (electrons's charge = 1.9 x 10^{-19} C) [1, 2]. Due to the color confinement, quarks cannot be directly observed or found in the universe, they are constrained within hadrons, such as baryons and mesons. In Fig. 1.1, two lower rows shows the three generation of the leptons ($e^{\pm}$, $\mu^{\pm}$, $\tau^{\pm}$ and it's corresponding neutrinos).

The quarks and leptons have spin 1/2, known as fermions, and quarks have different color states: red(anti-red), green(anti-green), and blue(anti-blue). Their interactions are mediated by exchanging the gluons, called the strong interactions, which is one of the four fundamental interactions in the nature. The Quantum Chromodynamics theory which describe the strong interaction together with the unification of electroweak theory, composes the Standard Model (SM). The SM theory was developed around the latter half of the twenty century, by a lot of efforts of scientists all over the world. Over time and through many experiments, the Standard Model has become a well-tested physics

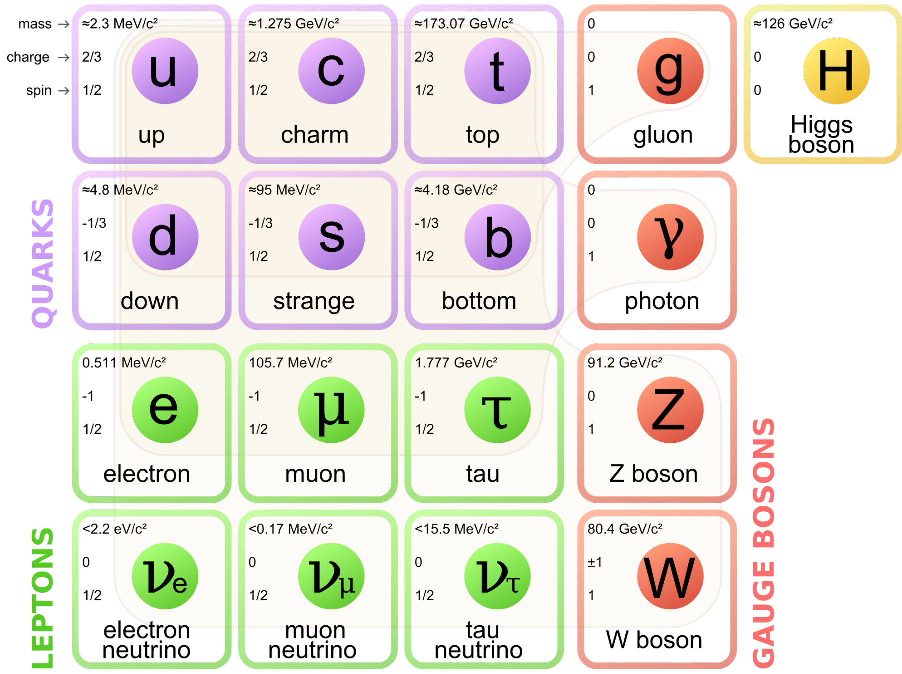

Fig. 1.1: Three generations of quarks and leptons in the Standard model.

theory. Because of it's success in explaining a wide variety of experimental results, the Standard Model is sometimes regarded as the "theory of almost everything".

There are four different fundamental interactions force in the universe: the strong, weak, electromagnetic, and gravitational force. These force effectively work in different range scales with different strengths. Three of these fundamental forces exchanging boson particles: the strong interaction is carried by exchanging gluons, the electromagnetic force by changing photons, the weak force by exchanging W and Z boson.

The Standard Model includes the electromagnetic, strong and weak forces and all their mediated particles, and explains well how these forces act on all of the matter particles as shown in Fig. 1.2.

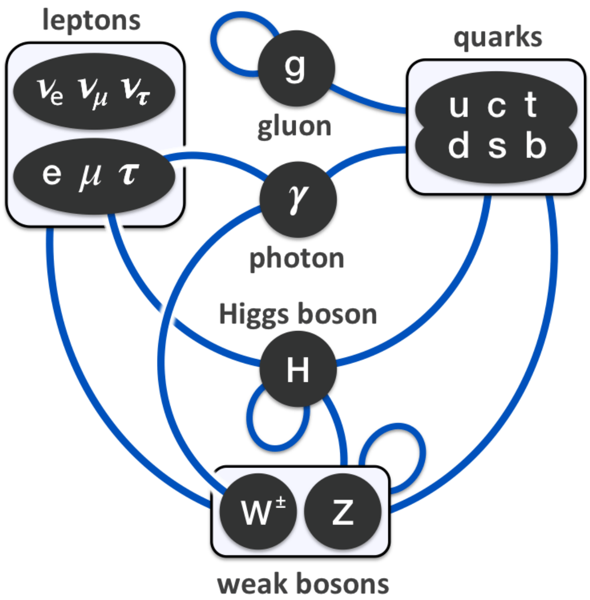

Fig. 1.2: Summary of interactions between elementary particles described by the Standard Model.

In the Standard Model of the particle physics, one of the four fundamental force describing the interactions between quarks and gluons, is called Quantum chromodynamics (QCD). QCD is described by the quantum field theory [3], which is a non-abelian gauge theory with symmetry group SU(3) [2]. Since the color charge, carried by the quarks and gluons cannot be isolated in the universe, they cannot be directly observed from the experiments. The strong interaction constrained the quarks and gluons together as hadrons (mesons and baryons). when you try to separate a quark from other quarks, the energy in the gluons field is enough to create another quark pairs, they are thus forever bound into hadrons, the confinement has been demonstrated in lattice QCD theory. which has been widely used for reliable QCD calculations, however, the precision of lattice QCD calculation is limited by the lattice spacing or the computing power [4]. We call this phenomenon as confinement, which means one cannot separate the free quarks. Because of the phenomenon of the confinement.

Usually, as the strength of the force can be described by the coupling constant in the interaction of the field theory, the strong interaction described by the renormalized QCD coupling constant, which is a scale dependent parameter $\alpha_s(\mu)$ (running coupling). Due to the gluons self-interactions, the QCD has a different behavior compared with QED field theory, the $\alpha_s(\mu)$ can be written as Eq. 1.1:

$$\alpha_s(\mu) = \frac{g_s^2(\nu)}{4\pi} \approx \frac{4\pi}{\beta_0 \ln(\mu^2/\Lambda_{QCD}^2)} \tag{1.1}$$

When $\beta_0 > 0$, this solution indicate the asymptotic freedom property: at the higher momentum transfer $\mu \to \infty$, $\alpha_s(\mu) \to 0$ which means the strength of the force of the strong interaction will be very small, so the QCD can be calculated. On the other hand, when $\mu << \Lambda_{QCD}$, the item $\ln(\mu^2/\Lambda_{QCD}^2)$ in Eq. 1.1 will go to 0, so there is a very strong coupling at $\mu << \Lambda_{pQCD}$, so QCD is non-perturbative in this case. $\alpha_s(mu)$ can be determined by the experiments. Fig. 1.3 shows the measured α_s from the different experiments measurements as a function of the transfer momentum μ and compared with lattice QCD calculations [5]. Fig. 1.3 shows with the higher momentum transfer μ, the effective coupling becomes smaller, so a lot of physics process can be calculated using perturbative method [6], like Leading Order (LO), Next- to-Leading Order (NLO), Fixed-Order Next-to-Leading Logarithm (FONLL). There are plenty of high energy experiments (like LHC, RHIC etc.) [7, 8, 9], which can quantitatively test the validation of these calculations.

1.1.1 Deconfinement and phase diagram

Due to the color confinement, quarks are constrained in the hadrons, inside the hadrons in normal condition. However, with sufficient high temperature or energy density, the distances between quarks are very short, the effective coupling is very small. The quarks will be deconfined, and the (color) degrees of freedom will appear, leading to a state of Quark-Gluon Plasma, which is suggested as the early universe one micro seconds after the Big Bang [10, 11, 12]. This is the so-called deconfinement phase transition. Meanwhile, the broken chiral symmetry in normal QCD matter will be restored and consequently, masses of scalar mesons and vector mesons will decrease [13]. Lattice QCD calculations provide quantitative predictions on this phase transition: the critical temperature of this phase transition T_c is about 150-180 MeV [14]. Lattice QCD calculations predict

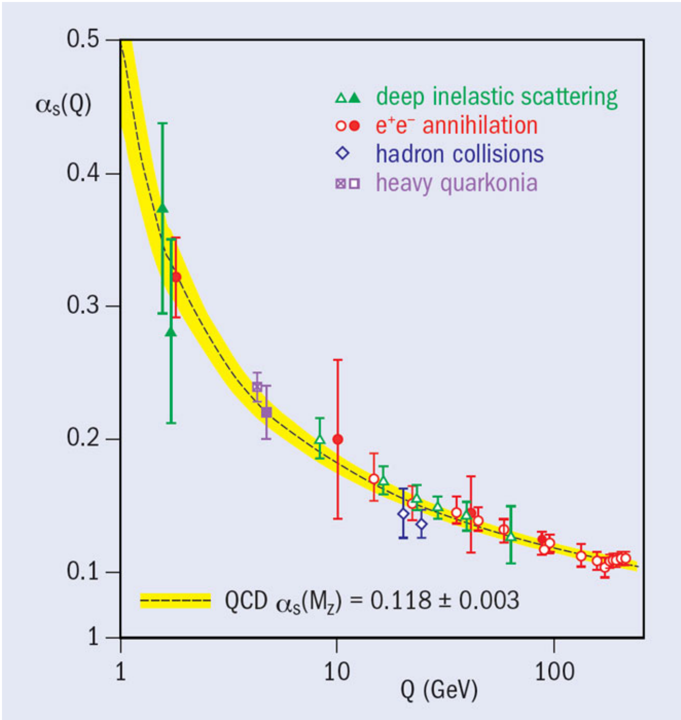

Fig. 1.3: Measured QCD running coupling constant α_s as a function of the transfer momentum μ in different experiments and compared with the lattice QCD calculations.

a phase transition from a confined phase, hadronic matter, to a deconfined phase, or Quark-Gluon Plasma (QGP), at a temperature of approximately T_c 150-180 MeV. Fig. 1.4 shows the phase diagram of the hadronic and partonic matter. A phase transition from the confined hadronic matter to the deconfined QGP matter is expected to happen at either high temperature or large baryon chemical potential μ_B.

1.2 Heavy Ion Collisions and Quark-Gluon Plasma(QGP)

In 1974, T. D. Lee and G. C. Wick proposed that one may produce the abnormal nuclear state by increasing the nuclear density through high energy collisions between heavy nuclei [15, 16]. In the latter 1970 and earlier 1980, at the Bevalac accelerator at Lawrence Berkeley National Laboratory(LBNL), a milestone phenomenon called "collective flow" was discovered, indicating that the nuclear matter can indeed be compressed in nuclear collisions [17, 18]. Ultra-relativistic heavy-ion collisions are suggested to be a possible

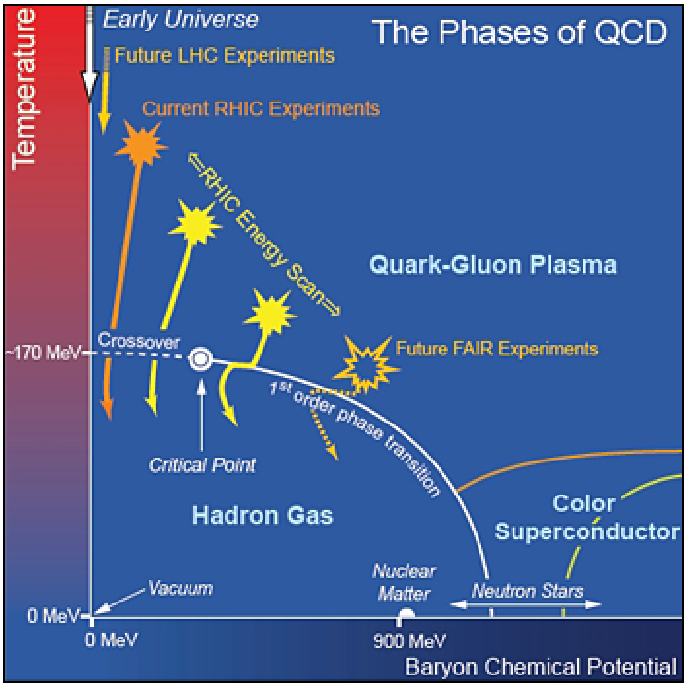

Fig. 1.4: The QCD phase diagram with boundaries in the nuclear matter.

way to explore the QGP [19, 20]. If the energy density is high enough, such QCD matter phase can be created [21]. When the system expands and cools down, quarks from the deconfined phase are hadronized into hadron phase [22]. The system continues to expand until the energy density is lower enough that hadrons have no any interaction with each other. All the hadrons will evolve into stable particles, like pions, protons, kaons. After that moment, these particles can be detected by particle detectors as shown in Fig. 1.5.

In the past ten years, the Relativistic Heavy Ion Collider (RHIC) at Brookhaven National Lab (BNL) obtained a lot of exciting physics results, which reveal that the new state of QCD matter is indeed created at RHIC, and the created QCD matter with high energy density and high temperature cannot be described by the hadronic degrees of freedom. This is a demonstration of the signatures for QGP. Some of the evidences from the measurements will be discussed in the following.

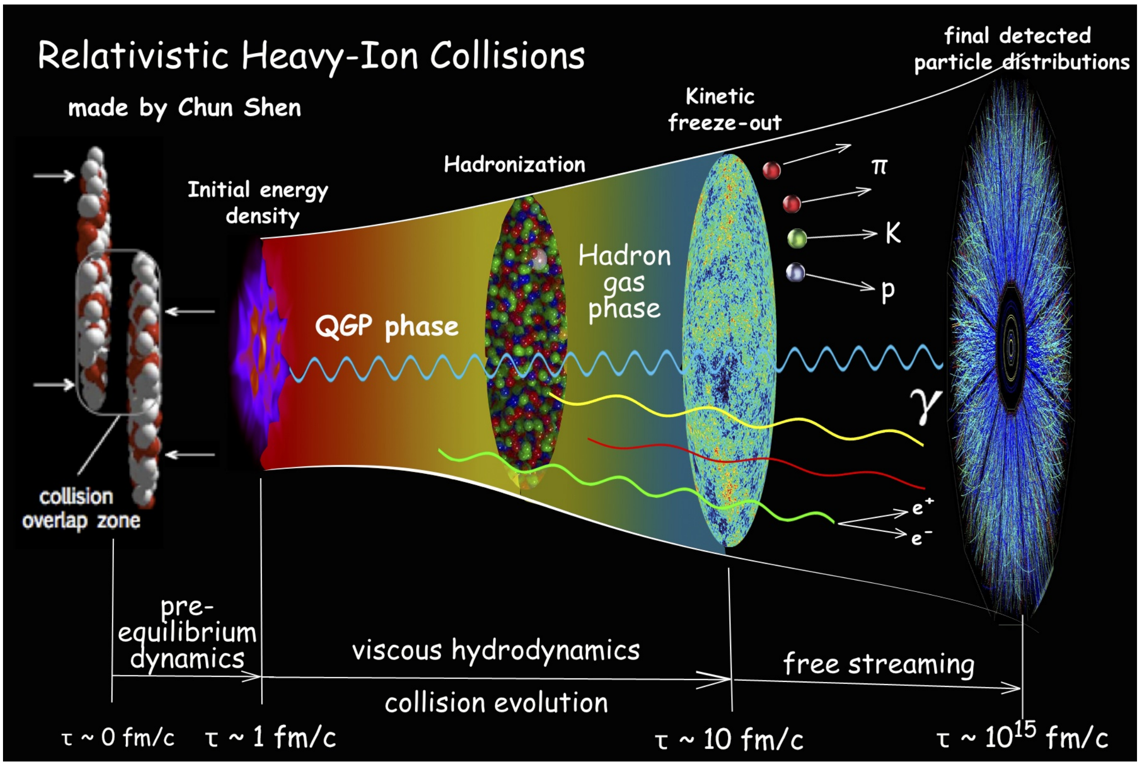

Fig. 1.5: The evolutions of different state in the heavy-ion collisions.

1.2.1 Jet quenching

In heavy ion collisions, particles with high transverse momentum are suggested to be produced dominantly during initial hard parton scatterings. These particles are excellent probes to study parton interactions with the hot QGP medium. These particles are created in the earlier stage, so they undergo the whole QGP evolution, leading to significantly reduce their energy losses. The first evidence of parton energy loss has been observed at RHIC from the suppression of high p_{T} particles by studying the nuclear modification factors [23] and the suppression of back-to-back $\Delta\phi$ correlations of the final state particles [24]. In order to describe the medium effect qualitatively, the nuclear modification factor R_{AA} was defined to reflect the interactions between the high energy partons and the medium. The nuclear modification factor is the ratio of the invariant yield in A+A collisions and p+p collisions scaled by the number of binary (nucleon) collisions N_{coll}, which is defined in Eq. 1.4, N_{coll} can be calculated from the Glauber model [25, 26, 27], which is shown on Fig. 1.6, A and B represent two heavy-ions beams,

$\vec{b}$ is impact parameter, $\hat{T}(\vec{b})$ from Eq. 1.3, gives the joint probability per unit area of nucleons being located in the respective overlapping target and projectile of differential area $d^2s.\hat{T}(\vec{a})$ and $\hat{T}(\vec{b})$ are the nuclear thickness function describing the nuclear profile [27]. If there is no interactions between partons and the medium, the nuclear modification factor R_{AA} should be equal to one. If R_{AA} greater (smaller) than one, it means the final states of high $p_{\rm T}$ particles have some enhancement (suppression) from hot medium.

$$N_{coll}(\vec{b}) = AB\hat{T}_{AB}(\vec{b})\sigma_{inel}^{NN} \tag{1.2}$$

$$\hat{T}(\vec{b}) = \int \hat{T}_A(\vec{s})\hat{T}_B(\vec{s}-\vec{b})d^2s \tag{1.3}$$

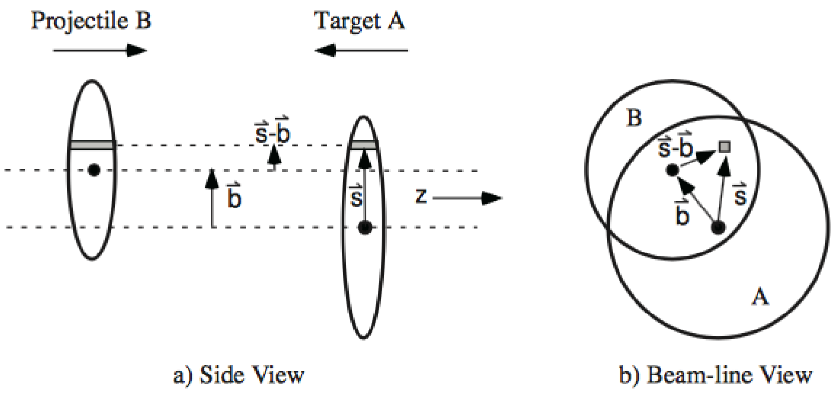

Fig. 1.6: Schematic representation of the Optical Glauber Model geometry, with transverse (a) and longitudinal (b) views.

$$R_{AA}(p_T) = \frac{dN_{AA}^2/(dp_T dy)}{< N_{coll} > dN_{pp}^2/(dp_T dy)} \tag{1.4}$$

The strong suppression has been observed from both the experiment measurements and the theoretical calculations, Fig. 1.7, $R_{AA} < 1$ for high $p_{\rm T}$ (4 GeV/c $< p_{\rm T}$), in various collision systems by different experiments. The result is suggest as a good signal for the discoveries of QGP, however, the R_{AA} was affected by both the initial and final states nuclear matter effects, so it's not sufficient to draw the conclusion that the discoveries of the QGP.

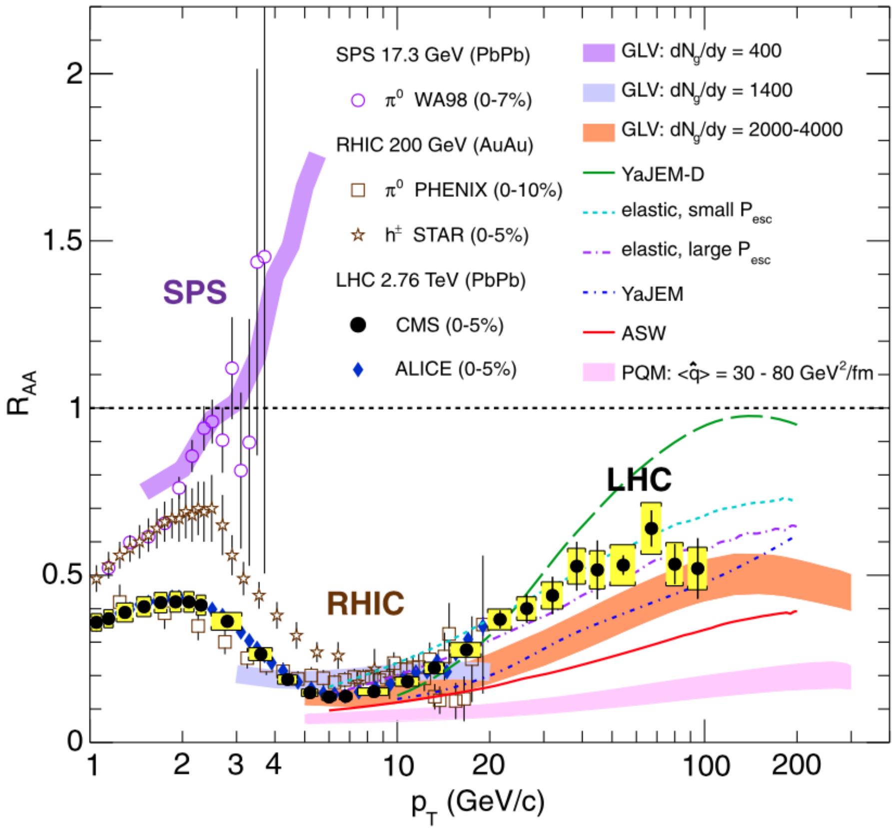

Fig. 1.7: The experiment measurements and the theoretical calculations of the nuclear modification factor R_{AA} as a function of the transverse momentum p_{T} in different central bins from heavy-ion collisions at three different center of mass energies, as a function of p_{T} .

Another important method for jet quenching is the high p_{T} hadron-hadron azimuthal correlation. In different collisions systems(p+p, d+A and Au+Au) from the STAR experiments, shown on Fig. 1.8, from this plots, the flavor dependent medium interaction can be obtained, for the triggered particles, there is a minimum p_{T} cuts required, those particles's parents partons are created mostly in the initial hard scatterings in the early stage. the created pair of partons go through the medium in opposite directions in the transverse plane. In Fig. 1.8, there is a clear peak on the away side ($\Delta\phi = \pi$), $\Delta\phi$ is calculated based on the Eq. 1.5, in both p+p and d+Au collisions. However, peak disappeared in central Au+Au collisions, this can be explained as one of the partons loses all of its energy in the hot QCD medium. In Au+Au collisions, due to strong interaction with the medium when undergoing the hot QCD medium.

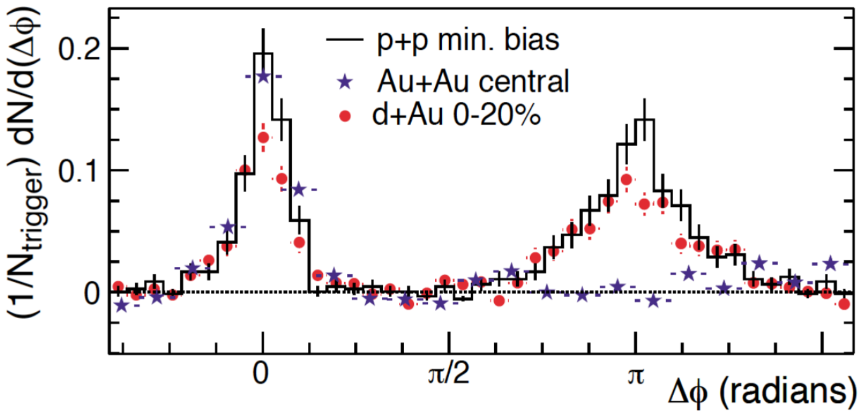

Fig. 1.8: Comparison of two particles azimuthal distributions for central d+Au collisions to those seen in p+p and central Au+Au collisions. The respective pedestals have been subtracted.

$$D(\Delta\phi) = \frac{1}{N_{trigger}}\frac{1}{\varepsilon}\frac{d_N}{d(\Delta\phi)} \tag{1.5}$$

1.2.2 Collective motion

In semi-central or peripheral Au+Au collisions, the overlapping area of two ions is an ellipsoid shape, which will lead to the spatial space asymmetry and will be transferred into the momentum space asymmetry by the asymmetry of pressure gradients which is shown on 1.9.

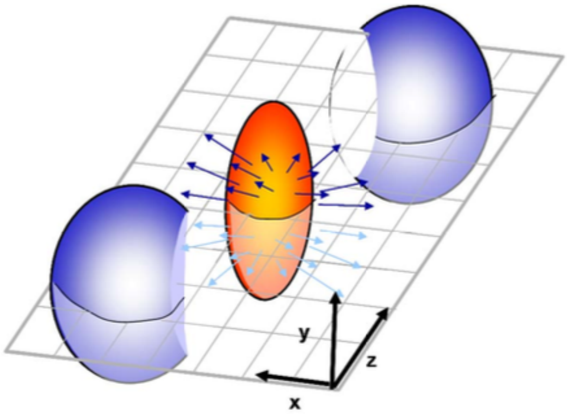

Fig. 1.9: The overlapping area of two near spherical shape in the non-central Au+Au collision at RHIC.

The final state particles production can be expanded in a form of fourier series Eq.1.6 azimuthal particle distributions in momentum space. The coefficient v_n of the fourier series Eq. 1.6 can be found in the Eq. 1.7.

$$E\frac{d^3N}{d\vec{p}^3} = \frac{1}{2\pi}\frac{d^2N}{p_T dp_T dy}\{1+\sum_{i=1}^{\infty}2v_n\cos[n(\phi-\Psi_r)]\} \tag{1.6}$$

$$v_n =< cos[n(\phi-\Phi_{RP})] > \tag{1.7}$$

here the Ψ_r is the reaction plane angle, fourier decomposition has often been applied to the differential particle production spectra with respect to the azimuthal angle, in the equation of the form of fourier series. The fist term coefficient v_1 is called the direct flow, and the second harmonic term is the most significant term representing the azimuthal anisotropy in momentum space, called v_2 as the elliptic flow, the elliptic flow is produced mainly during the highest asymmetry of pressure gradients of the density phase of the evolution before the initial geometry asymmetry of the plasma disappears [28]. In the real case, the azimuthal angle should be written with respect to the true reaction plane Ψ_r in each event, which is defined by the impact parameter and the beam line z direction. However, the impact parameter cannot be measured directly in the experiment, so that we cannot get the true reaction plane in the experiment, therefore, approximately estimation usually been used, based on the angular distribution of all the final state particles in every event, so the event plane resolution should be corrected in the final physics results.

Fig. 1.10 shows the elliptic flow v_2 as a function of transverse momentum p_{T} for the various charge hadrons (π, K, proton) in Au+Au collisions at 200 GeV [29], the top-left panel shows the negatively charged particles, while the top-right panel shows positively charged particles, the bottom-left panel shows the combined positive and negative particles together and compared with the hydrodynamical calculations that was including a first-order phase transition [30], the bottom-right panel shows both the elliptic flow v_2 and p_{T} have been divided by the number of quarks, various hadron species are scaled by the different number of constituent quarks n_q in the hadrons, n_q i.e. =2 for mesons and 3 for baryons, the motivation described in the Ref. [31] called quark-coalescence mechanism, the scaled elliptic flows v_2 for different types of hadrons consistent with each other, this is a very strong evidence that the constituent quarks number scaling can be explained as the elliptic flow of intermediate p_{T} hadrons come from the combination of the constituent quarks, this exciting results indicate that the partonic degrees of freedom in the QCD medium, and the final state hadrons came from the constituent quarks recombination.

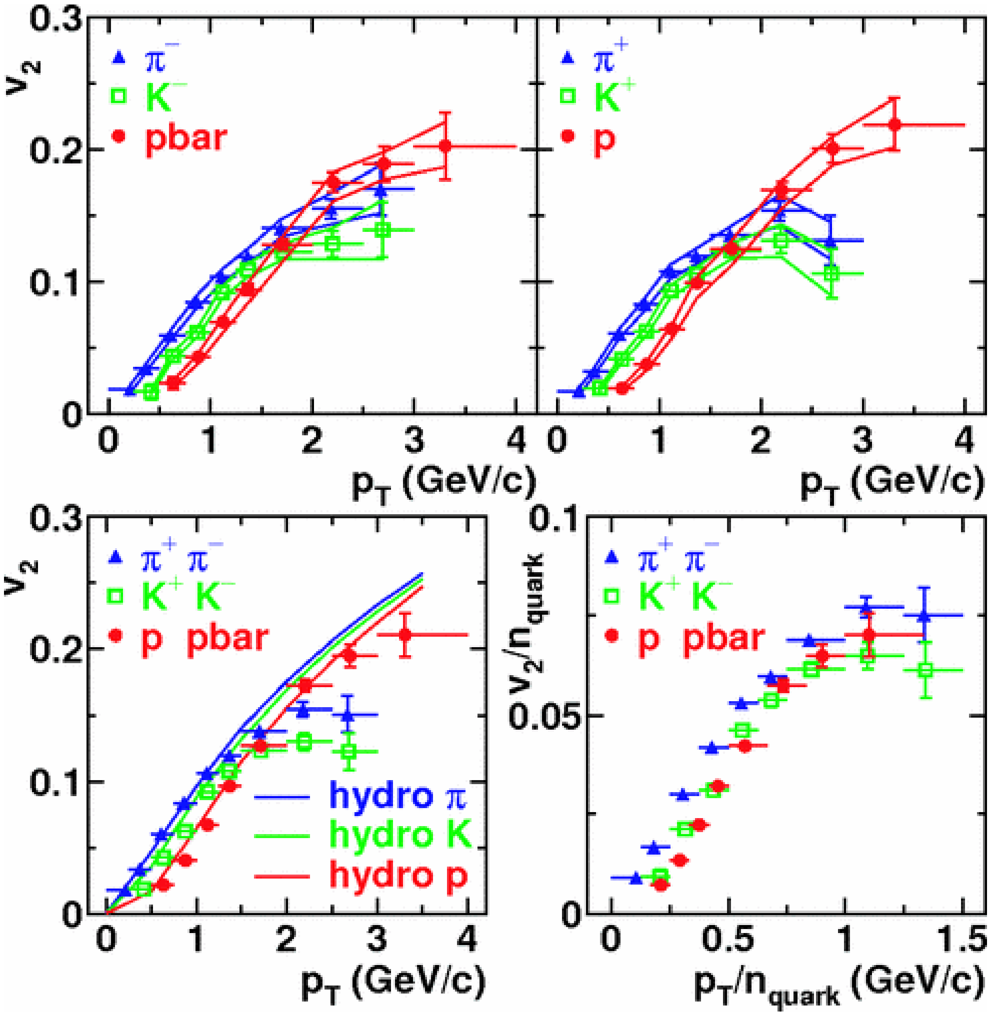

Fig. 1.10: Top left panel shows the transverse momentum dependence of v_2 for different particles, (π^-, K^-, proton); Top right panel shows the transverse momentum dependence of v_2 for the anti-particles, (π^-, K^-, anti-proton); The bottom-left panel shows the combined positive and negative particles together and compared with the hydrodynamical model calculations; The bottom-right panel shows both the elliptic flow v_2 and p_T have been divided by the constituent number of quarks.

1.3 Heavy flavor production at RHIC energies

The Charm and bottom quarks, its mass (charm and bottom quarks,$m_c \approx 1.3$ GeV/c^2 and $m_b \approx 4.2$ GeV/c^2) is higher than the typical QCD mass 200 MeV [32]. They are the important tools for the studying of the QCD matter in high energy hadronic collisions. Since from the production mechanisms, heavy flavor quarks are produced via the initial hard scattering. Therefore, the heavy quarks production is expected to be well calculated by perturbative QCD [33]. Therefore, high precision measurements of heavy flavor production in proton-proton collisions are instrumental to test the validity and constrain the parameters of perturbative QCD calculations of heavy quark production. Fig. 1.11 shows the charm quark production cross section as a function of transverse momentum p_{T} in p+p collisions at $\sqrt{s}$ = 200 GeV [34]. The black triangle present for D^0 and point for D^*, respectively. Charm quarks production obtained by the charm quark fragmentation ratios 0.565±0.032(c→ D^0) and 0.224±0.028(c→ D^*), the charm fragmentation ratio from the measurements of CLEO and BELLE experiments [35], the red curve is the power-law fit of the measured data points. The p_{T} integrated $c\bar{c}$ cross section at mid-rapidity has been obtained on Eq. 1.8. The measured charm-pair cross section at mid-rapidity in p+p collisions is consistent with STAR' s measurement in d+Au collisions [36].

$$\frac{d\sigma}{dy}\Big|_{y=0}^{c\bar{c}} = 170 \pm 45(stat)^{+38}_{-59}(sys)\mu b \tag{1.8}$$

Blue dashed lines are the upper and lower edges for the FONLL pQCD calculation calculations [33]. The STAR results are consistent with the upper limit of the FONLL pQCD calculation. On the other hand, the quarkonium bound state process is non-perturbative process, which is based on the long distances and soft momentum scales, the studying of heavy flavor quarkonium production and comparing the calculation to the experiments data can test the non-perturbative QCD calculations as well.

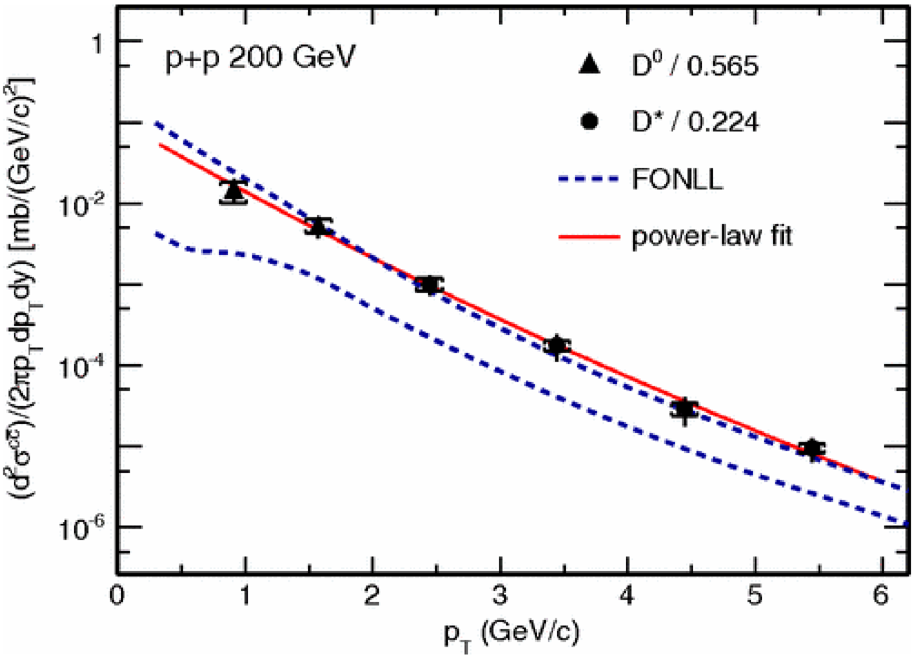

Fig. 1.11: Charm quarks production from proton-proton collisions at $\sqrt{s}$ = 200 GeV and compared with FONLL calculations.

Studying heavy flavor production in heavy-ions collisions can help understand properties of QGP and partons interactions with hot medium. The strong modification of heavy flavor production in Au+Au collisions compared with p+p collisions suggests strong interaction of heavy flavor partons with hot medium. Fig. 1.12 shows the D^0 nuclear modification factors R_{AA} as a function of the momentum p_{T} at Au+Au collisions at $\sqrt{s_{NN}}$ = 200 GeV by the STAR experiment. Different panels are for different centrality bins of 40-80%, 10-40% and 0-10% [37], the statistical and systematic uncertainties are represented by the vertical lines and brackets, respectively. The nuclear modification factors R_{AA} at high p_{T} indicate a significant suppression in the most central collisions compared with p+p collisions, In central collisions, the suppression level is consistent with the that the light hadrons [38] and the electrons from open heavy flavor hadrons decay [39]. The measured results are compared with the different model calculations from the TAMU (solid curve), SUB-ATECH (dashed curve), Torino (dot-dashed curve), Duke (long-dashed and long-dot-dashed curves), and LANL groups (filled band). Both the measurements and the models have a strong suppression, which means the heavy quarks lose energy in the medium at central Au+Au collisions at RHIC energies.

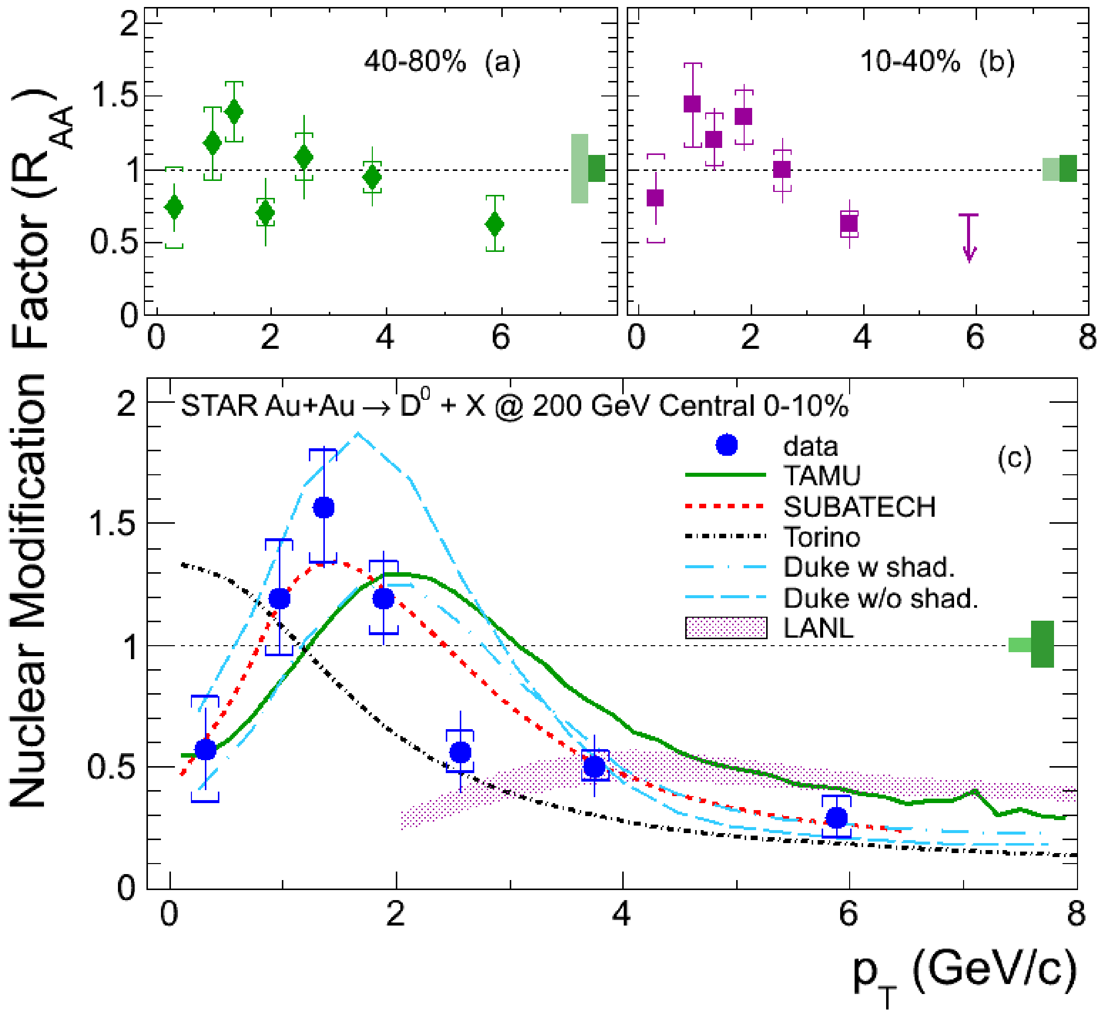

Fig. 1.12: Top two panels shows the D^0 R_{AA} for peripheral 40-80% and semi-central 10-40% collisions; Bottom panel shows the D^0 R_{AA} for centrality 0-10% (blue points) compared with different model calculations. The vertical lines and boxes around the data points present the statistical and systematic uncertainties, the vertical bars around unity denote the overall normalization uncertainties in the Au+Au and p+p data, respectively.

1.3.1 Previous non-photonic electron measurements at RHIC

Experimentally, there are two different ways to measure the open heavy flavor production: direct mesons hadron reconstruction in hadronic decay channels and electrons from semi-leptonic decay channels. The statistics is always very hungry for the heavy flavor measurements, particularly in the RHIC energies, since the production cross section is much lower than the light flavor hadrons. The electrons from semi-leptonic decays of heavy flavor hadrons (NPE) have better statistics than direct reconstruction in hadronic channels, although the decay leptons provide only limited information on the original kinematics of the heavy flavor parton. The electrons can be trigged efficiently with on-line triggers and can extend the kinematic range to higher p_{T} . so NPE is still a good method to study the heavy quark production at RHIC energies, especially at higher p_{T} .

The semi-leptonic decay electrons production has been measured from STAR [40], Fig. 1.13 shows the non-photonic electron invariant cross section as a function of p_{T} , in p+p collisions at 200 GeV, based on STAR Run 2008 and Run2005 data, the black curve is the FONLL calculations [33] , bottom panel shows the ratio of the data and FONLL calculations, FONLL is able to describe the STAR measurements within its theoretical uncertainties.

Fig. 1.14 shows the PHENIX measurement of the non-photonic electrons production [41] in p+p collisions at 200 GeV. The results have been compared with the FONLL pQCD calculation. The measurements are consistent with the central values of the FONLL calculation with the data uncertainty. The calculation indicate the contributions of charm and bottom decay to electrons, respectively, for higher p_{T} (4 GeV/c < p_{T}), the bottom decay contribution are larger than the charm hadron decay electrons [33].

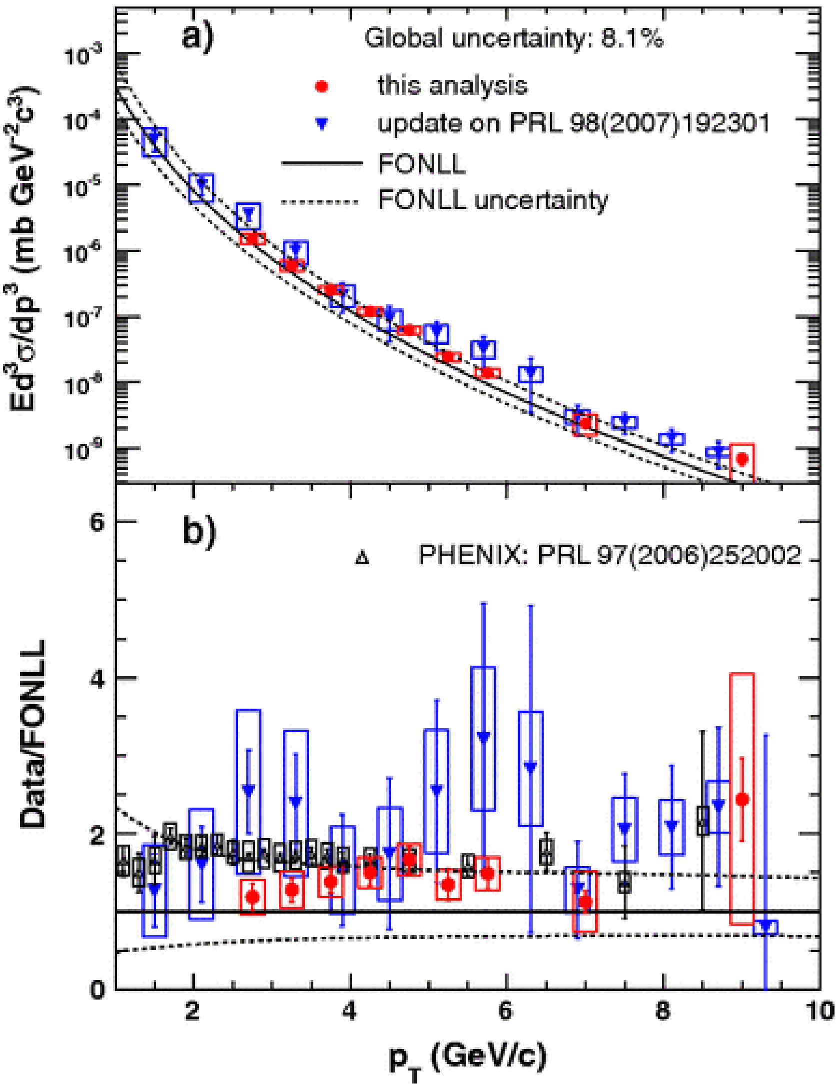

Fig. 1.13: Top panel shows the cross sections of the electrons from heavy flavor hadrons decays in proton-proton collisions at 200 GeV STAR measurements, the curves are from the FONLL calculations, bottom panel shows the ratio of the data and the FONLL calculation.

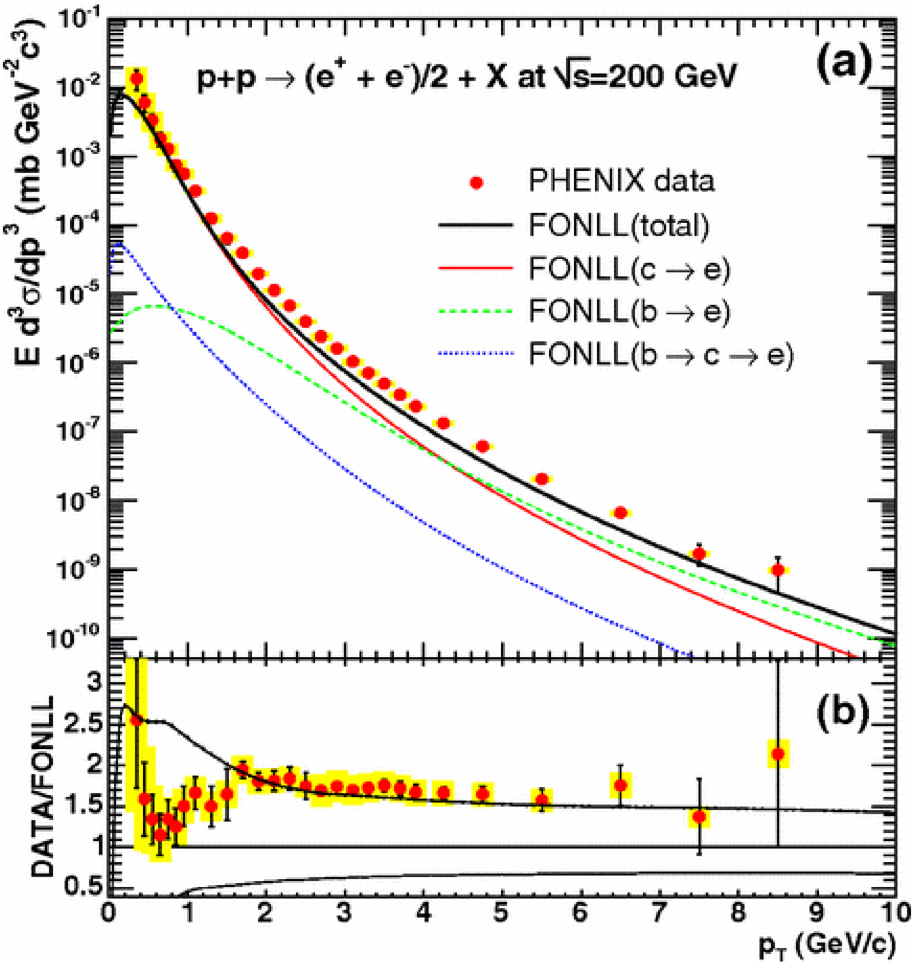

Fig. 1.14: Top panel shows the cross sections of the electrons from heavy flavor hadrons decays in proton-proton collisions at 200 GeV PHENIX measurements, the curves are from the FONLL calculations, bottom panel shows the ratio of the data and the FONLL calculation.

Fig.1.15 shows the nuclear modification factor R_{AA} as a function of p_{T} for d+Au and Au+Au collisions at 200 GeV from STAR experiment. The R_{AA} in central Au+Au collisions from the measurements are compared with the model calculations of heavy quark energy loss. The DGLV radiative energy loss model via few hard scatterings [42] with initial gluon density dN_g/dy=1000, the results are consistent with the light quark suppression. The BDMPS radiative energy loss model via multiple soft collisions [43, 39].

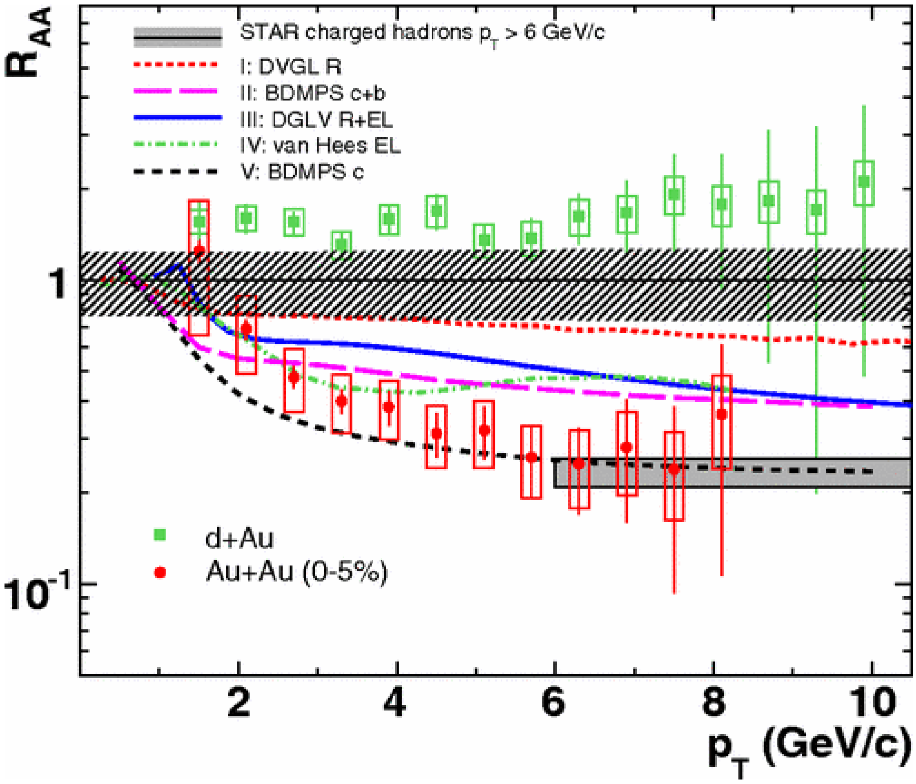

Fig. 1.15: The open heavy flavor hadrons decay electrons nuclear modification factor R_{AA} as a function of p_{T} for d+Au and Au+Au collisions at 200 GeV from STAR experiment.

Fig. 1.16 shows the elliptic flow v_2 for electron from open heavy flavor decay as a function of p_{T} from STAR and compared with model calculations [44]. The heavy flavor electrons production at low p_{T} is dominated by charm hadron decays [45], the calculation based on the partonic transport model BAMPS (Boltzmann approach to multi-parton scatterings) [46, 47]. As we can see, the partonic transport model BAMPS can describe the data.

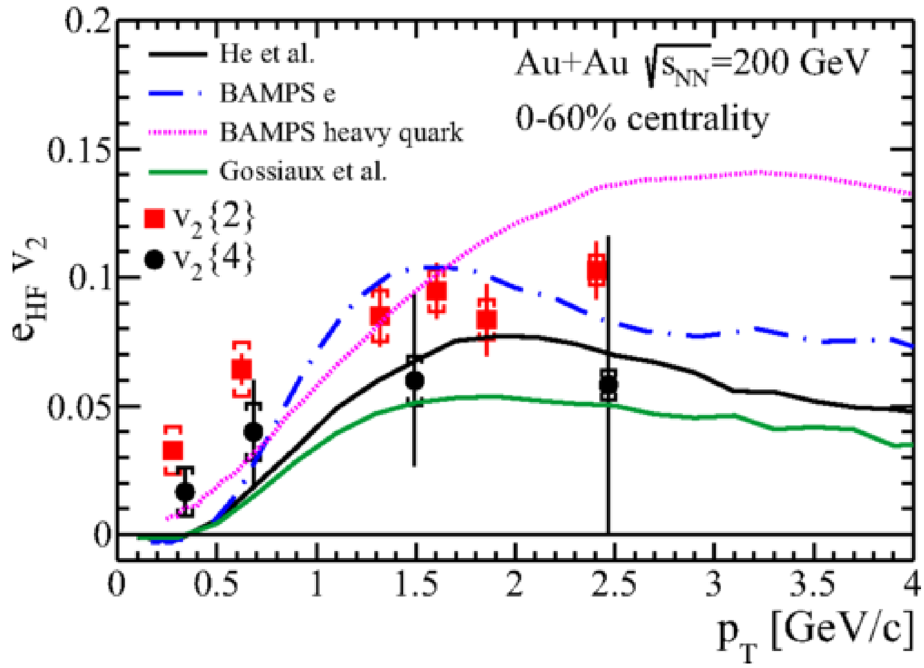

Fig. 1.16: The open heavy flavor hadrons decay electrons elliptic flow v_2 as a function of p_{T} in Au+Au collisions at 200 GeV from STAR experiment, the results compared with different model calculations.

The PHENIX experiment measured the nuclear modification factor R_{AA} and elliptic flow v_2 for electron from open heavy flavor decay as a function of p_{T} in Fig. 1.17 . [48]. Both the measured R_{AA} and v_2 are compared with the van Hees model [49, 39] calculation, the model can describe the data at higher p_{T} , but still some challenge at low p_{T} to match with the data.

As we can see both STAR and PHENIX measured R_{AA} in Au+Au collisions indicate a significant suppression in the most central collisions, which can be explained as the heavy quark energy loss during transport the mediums.

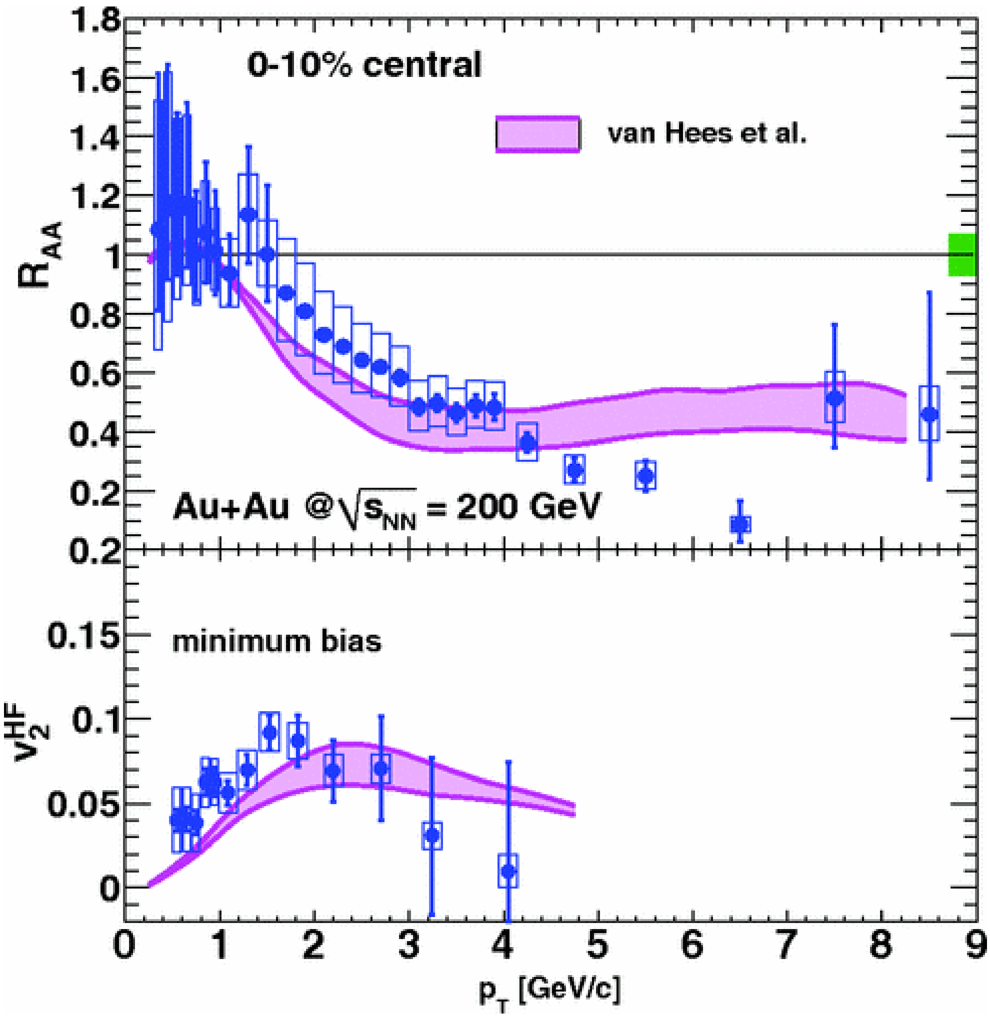

Fig. 1.17: Top panel shows the open heavy flavor hadrons decay electrons nuclear modification factor R_{AA} as a function of p_{T} for d+Au and Au+Au collisions at 200 GeV. Bottom panel shows the open heavy flavor hadrons decay electrons elliptic flow v_2 as a function of the p_{T} and compared to model calculations.

The open bottom production can be measured by b-jets or bottom hadrons. B-quark production cross section is small in RHIC energies, STAR has already measured the bottom production in p+p collisions via semi-leptonic decays channels. The measurement was based on the the azimuthal correlations between non-photonic electrons and charged hadrons. Fig. 1.18 shows the relative contribution of electrons from bottom hadron decays to the inclusive heavy flavor hadron decay electrons. The result is compared with FONLL calculations, which are consistent within uncertainties [45].

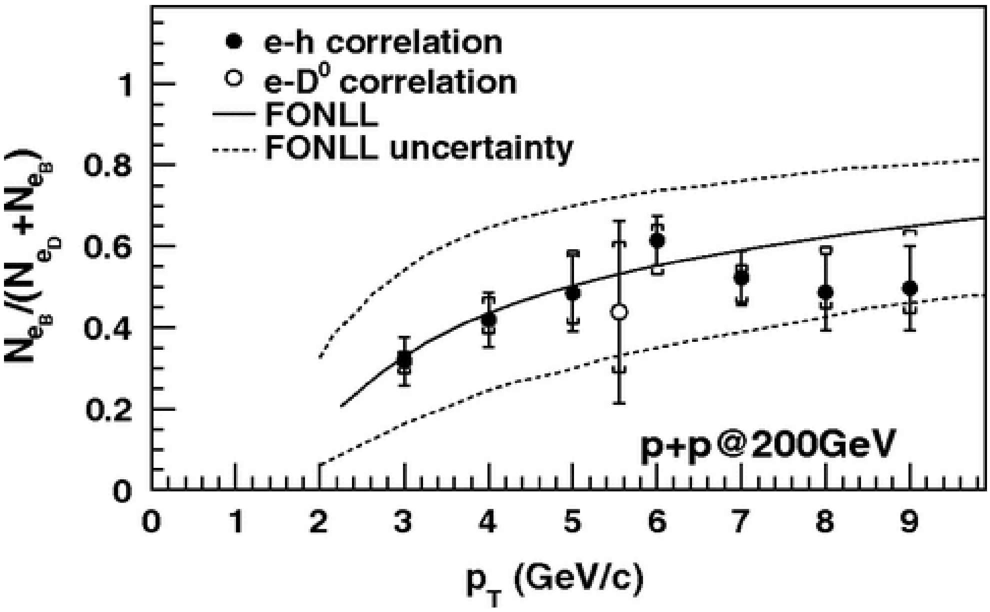

Fig. 1.18: The B hadrons decay electron relative contribution to the inclusive heavy flavor hadron decay electrons as a function of p_{T} , the black curve is the FONLL calculations.

1.4 Thesis outline

In this thesis, we will present measurements of electrons from semi-leptonic decays of open heavy flavor hadrons with the STAR experiment. Chapter 2 will introduce the RHIC and STAR detectors. Chapter 3 will present measurement of the non-photonic electron production in p+p collisions at $\sqrt{s}$=200 GeV. Chapter 4 will present separation of the charm and bottom production in Au+Au collisions at $\sqrt{s_{NN}}$ =200 GeV. Chapter 5 will give a summary and outlook.

CHAPTER 2

Experiment Set-Up

2.1 Relativistic Heavy Ion Collider (RHIC)

The Relativistic Heavy Ion Collider (RHIC) at Brookhaven Nation Laboratory (BNL) in Upton, New York, was built in the year of 1999. It was deigned to accelerate and collide heavy ions and proton beams, It is the only polarized proton collider at relativistic energy with high luminosity [50, 51]. The top center of mass collision energy is 200 GeV per nucleon pair for heavy-ion collisions and 510 GeV for polarized proton collisions. The basic design parameters of the collider are listed in Table 2.1. The main physics goal of RHIC is to investigate the phase transition from hadronic phase to QGP phase and properties of QGP.

RHIC has two accelerator/storage rings, one (Blue Ring) for clockwise and the other (Yellow Ring) for anti-clockwise beam. They are in the same horizontal plane but opposite directions, in a tunnel with a circumference of about 3.8 km. There are six interaction sections with collision points along the circumference. In every collision point, two beams could overlap with each other. Currently, there are two major experiments, STAR and PHENIX , located at 6 o' clock and 8 o' clock, and two minor ones PHOBOS and BRAHMS were located at 10 o' clock and 2 o' clock, respectively. Only one of them STAR is still in operation. RHIC has successfully conducted the p+p, d+Au, Au+Au, Cu+Cu, Cu+Au and U+U collisions with different collision energies [51].

Table 2.1: RHIC design parameters

Parameter	Value
Top beam energy (Au)	100 GeV/u
Top beam energy (proton)	250 GeV/u
per bunch (Au)	10^9
per bunch (proton)	10^{11}
Beam life time	8-10 hours
Ring circumference	3833.845 m

BNL is planning to construct a high intensity electron beam facility for electron and heavy-ion collisions, a upgrade program known as eRHIC. The eRHIC program aims to provide collisions of electrons with ions or protons in the center of mass energy range from 30 to 100 GeV with high luminosity. The heavy-ion beam can make use of the existing RHIC machine. This upgrade program can allow to study the structure and interactions of gluon-dominated matter, parton distribution function in nucleus [52] and the spin program [53].

2.2 STAR experiment

The Solenoidal Tracker at RHIC (STAR) is one of the two largest experiments at RHIC [54]. The detector was designed for the study of the QGP formation and its properties. The STAR detector provides high precision tracking, momentum measurement, and particle identification at the mid-rapidity region.

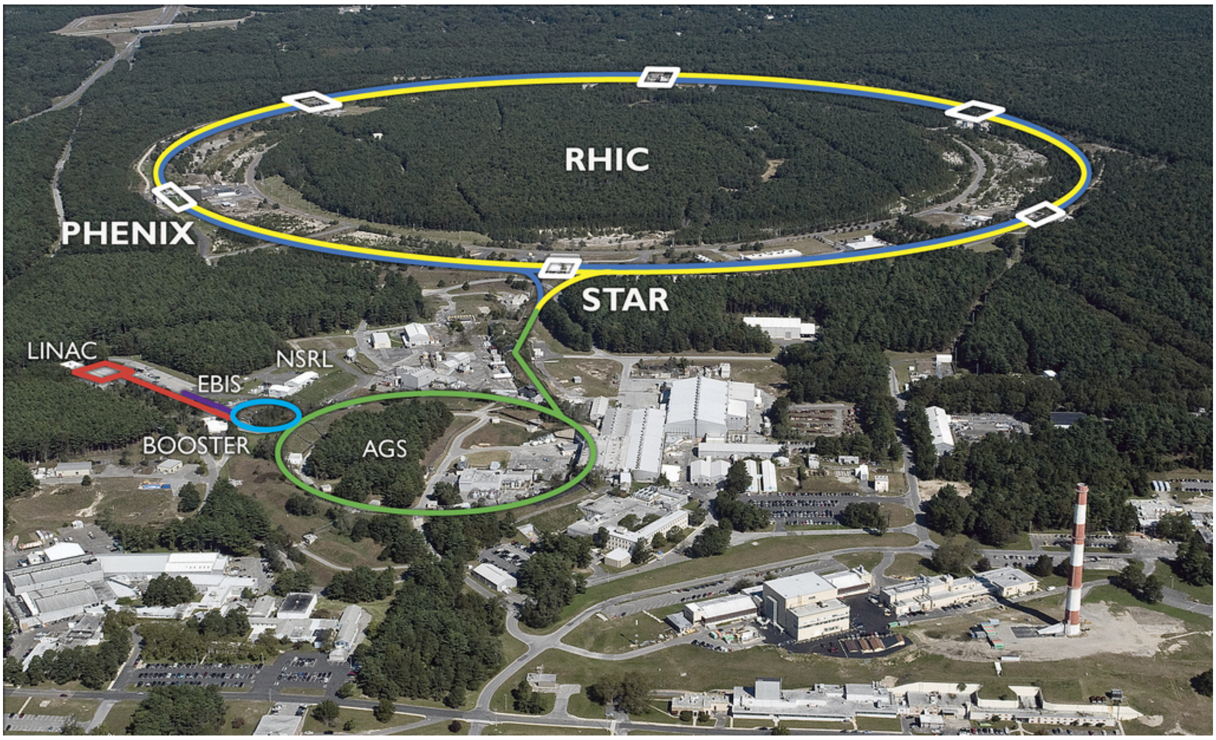

Fig. 2.1: The RHIC accelerator complex: The particle smashups recreating early universe conditions at RHIC depend on a chain of accelerators to bring ions up to speed. BRAHMS and PHOBOS have been decommissioned. PHENIX and STAR which are located at 6 o' clock and 8 o' clock are still operating.

2.3 STAR detectors

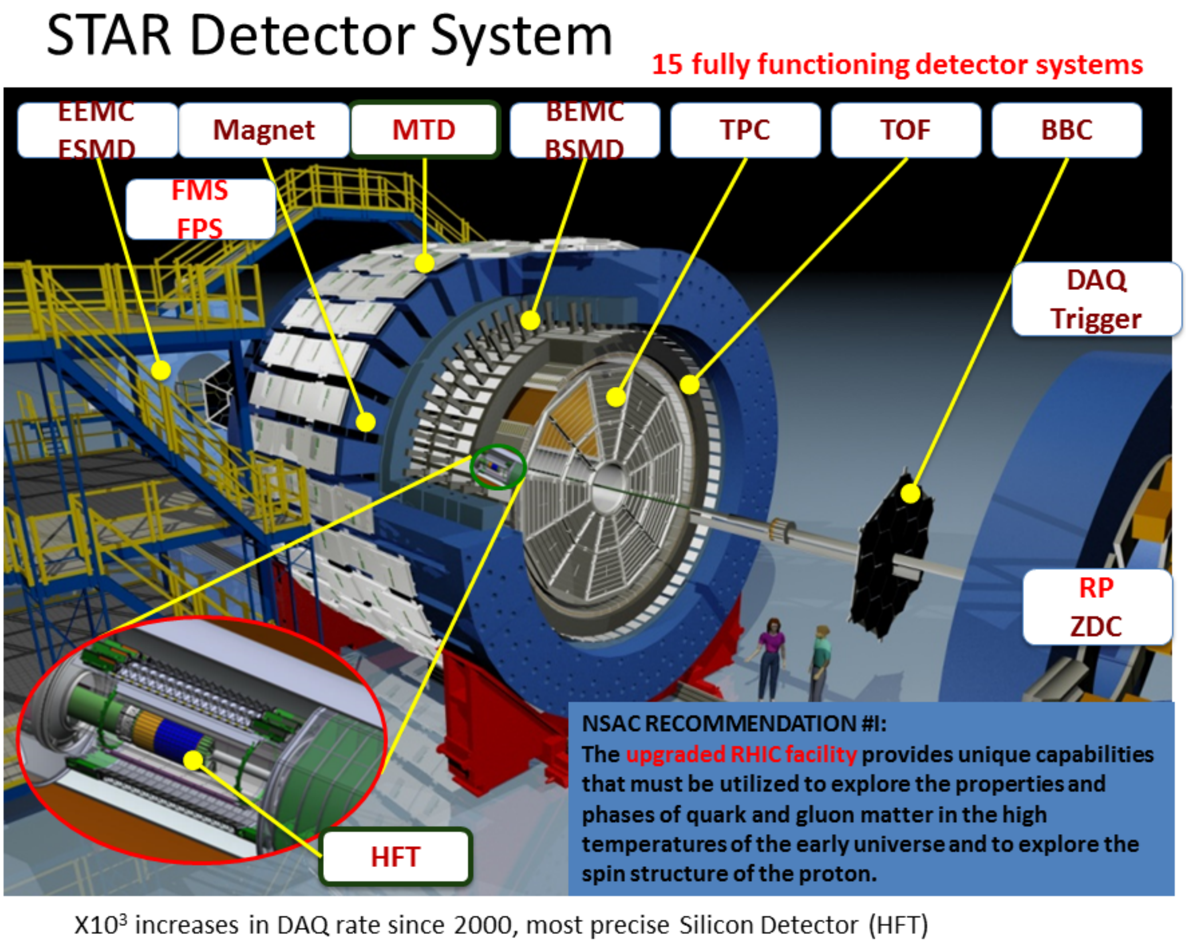

Fig. 2.2: The STAR detector system

STAR detector have a large coverage acceptance and excellent particles identification capability [55]. Fig. 2.2 shows the STAR detector systems. In the heart of STAR detector is the Heavy Flavor Tracker (HFT), which was installed in 2014. The HFT is designed for heavy flavor measurements. The Time Projection Chamber (TPC) is the main tracking at STAR. It has a coverage of $|\eta|$ < 1.3 and 2π in azimuthal direction. The TPC is designed to reconstruct the tracking of the charge particles, and perform measure the particles momentum, particle identification through ionization energy loss (dE/dx). The Time Of Flight (TOF) detector is outside of the TPC. It has a coverage of $|\eta| < 0.9$ and 2π in azimuthal direction. The TOF is designed for charged particles identification through the time of flight. The Barrel Electro-Magnetic Calorimeter (BEMC) surrounded the

TOF. It has a coverage of $|\eta| < 1$ and 2π in azimuthal direction. The BEMC is used for electron the high p_{T} identification and triggering. The STAR magnet provides a uniform magnetic field parallel to the beam direction. The Muon Telescope Detector (MTD) detector is also a new detector, installed in 2014. It can detect high p_{T} muons for quarkonium measurements.

Details for detectors that are used in this analysis, will be discussed in following.

2.3.1 Heavy Flavor Tracker (HFT)

The Heavy Flavor Tracker (HFT) is a new silicon detector designed to improve heavy flavor measurement precision [56, 57]. It can reconstruct open charm hadrons , such as D^0, $D^{\pm}$ and Λ_c [58, 59], via the reconstruction of their secondary decay vertices through the hadronic decays channels. The HFT can also measure the bottom production by an indirect way, through the non-photonic electrons, non-prompt J/ψ, non-prompt D^0 [60].

The HFT consists of three sub-systems shown in figure 2.3. The Silicon Strip Detector (SSD), a double-sided strip detector, is the outer-most layer of the HFT. The Intermediate Silicon Tracker (IST), consisting of a layer of single-sided strip-pixel detector, it is located inside the SSD, the inner most is the two layers of silicon pixel detector (PXL) are inside the IST. The PXL is made from state-of-the-art ultra-thin CMOS Monolithic Active Pixel Sensors (MAPS). This is the first time the CMOS MAPS detector is used in a collider experiment. The basic design parameters are for different parts are list on the table. 2.2, The HFT has excellent resolution for DCA and secondary decayed vertex reconstruction. The DCA resolution for DCA and as a function of the momentum shows on Fig. 2.4 [61]. With the HFT, combined with the TPC, TOF and the BEMC, STAR can measure precisely for the heavy flavor production both hadronic and simi-leptonic decay channels

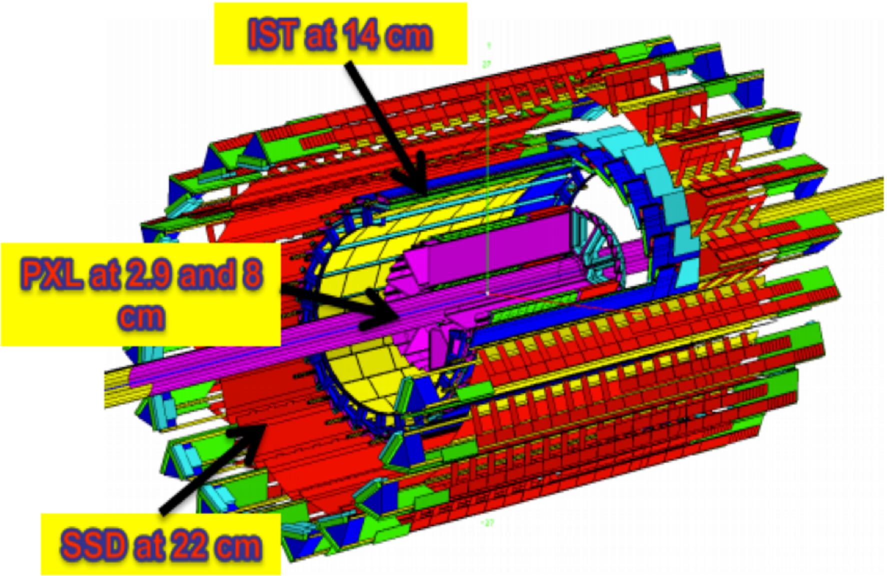

Fig. 2.3: Sub-system of the HFT detectors, the SSD is the out most detector, the IST inside the SSD and the PXL closest to the beam pipe.

Table 2.2: Pointing resolution of the HFT sub-detectors

Detectors	Radius (cm)	Hit Resolution R/ϕ-Z(μm-μm)	Radiation length
SSD	22	20/740	1% X_0
IST	14	170/1800	<1.5% X_0
PIXEL layer 2	8	12/12	0.6% X_0
PIXEL layer 1	2.9	12/12	0.4% X_0

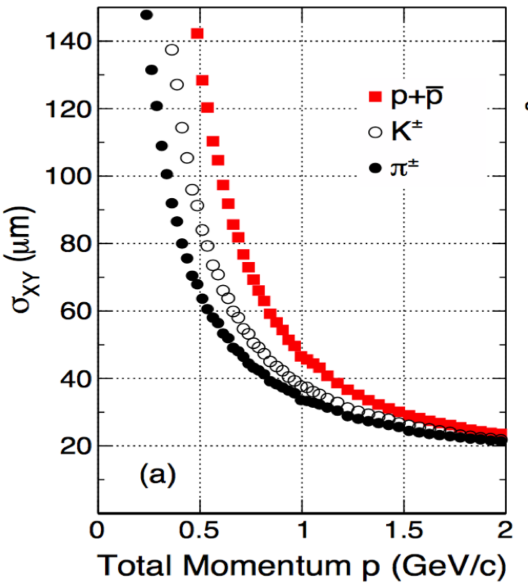

Fig. 2.4: Identified particle DCA$_{XY}$ resolution in the transverse plane as a function of particle momentum.

2.3.2 Time Projection Chamber (TPC)

The Time Projection Chamber (TPC) is the primary tracking device for the STAR experiment [62]. It is designed for the reconstruction of the tracks for the charge particles, momentum measurements [63, 64], particle identification through the ionization energy loss (dE/dx). Fig. 2.5 shows the STAR TPC geometry structures. It is a cylinden shape with a length of 4.2 m, an outer diameter of 4 m and inner diameter of 1 m. The TPC is located inside the STAR magnet system [65], which provides a magnetic field of 0.5 T along the beam direction. Charged particles momenta can be calculated based on the track curvature measured by TPC in the magnetic field. The TPC can measure the charged particles momentum over a range of 100 MeV/c to 30 GeV/c.

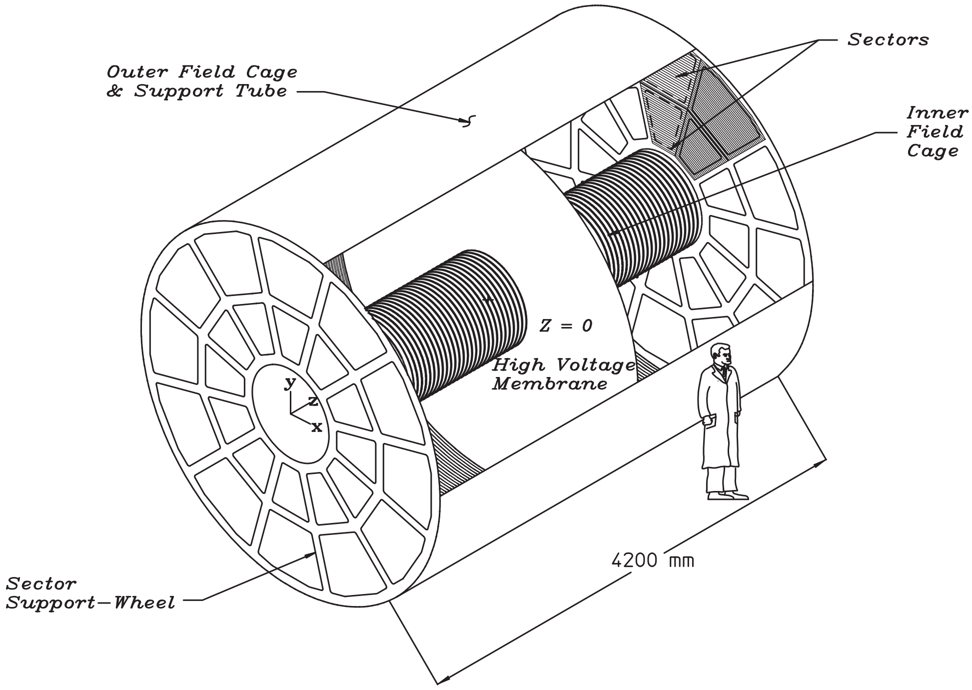

Fig. 2.5: The STAR TPC is 4.2 meters in length, along the beam line surrounding a beam-beam interaction region. Collisions take place near the center of the TPC.

When the charge particles go though the TPC gas volume (mixed 10% methane and 90% argon), negatively charged electrons and positively charged ions will be created by the interactions between charged particles and TPC gas. Because of the high voltage between cathode and anode. Typical potential is 28 kV, ionized secondary electrons drift to the readout end caps at the ends of TPC. The position on transverse plane are decided by the position of the readout pads in both ends of the TPC, while the Z position can be calculated based on the drift time and drift velocity, Trajectories of the charge particles can be reconstructed on 3-D space based on these drift positions.

There are 12 readout sectors for every side of the TPC end caps. These 12 sectors are arranged uniformly to cover the full azimuthal of 2π. Fig. 2.6, the inner section is on the right side and the outer section in the left side. Every readout sector is divided into pads for different readout channels. There are 136608 readout channels in total. The pads in both the inner and outer sections are organized into 45, 32 rows for the inner and 13 rows for outer. Therefore, when the charged particles go through the TPC, there will be at most 45 hits for a single track. The read out pads size for the outer and inner section is different, inner section is smaller than the outer, the pad size for the inner section is 2.85 $\times$11.5 mm^2, while for the outer section is 6.2 $\times$19.5 mm^2, the motivation for this design is to increase the hits resolution for the inner section, since the track multiplicity for low momentum is higher than the high momentum, the good hits resolution can make sure to reconstruct the high multiplicity tracks. The read out electronics of the inner section and outer section are different as well, the difference can be found in the Ref. [65].

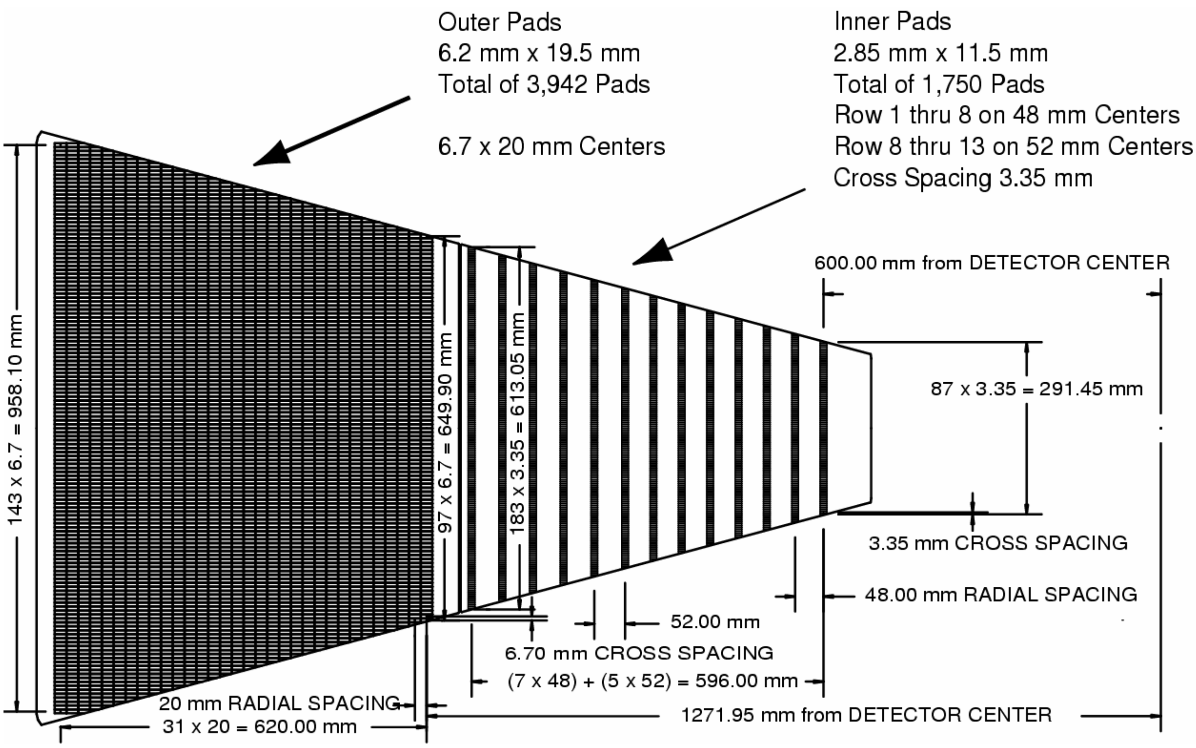

Fig. 2.6: The anode pad plane with one full sector shown, the inner sub-sector is on the right and it has small pads arranged in widely spaced rows, the outer sub-sector is on the left and it is densely packed with larger pads

The TPC for particle identification is based on ionization energy loss (dE/dx). In principle the dE/dx information can be extracted from the signal from up to 45 pad rows, However, the pad length is too short to average out the ionizations energy loss (dE/dx) fluctuations, so it is not possible to measure the average (dE/dx) including all pads. In experiment, typically 30% of the pad raws with the largest signals are removed. The average energy loss ($< dE/dx >$) can be estimated by the Bethe-Bloch Eq. 2.1 [66]:

$$-\frac{dE}{dx} = Kz^2\frac{Z}{A}\frac{1}{\beta^2}[\frac{1}{2}\ln\frac{2m_ec^2\beta^2\gamma^2T_{max}}{I^2} - \beta^2 - \frac{\delta}{2}] \tag{2.1}$$

The ionization energy loss (dE/dx) as a function of particle momentum is shown in Fig. 2.7, where the dE/dx resolution is indicated by the width of the color bands. S it can be seen, the particles can be identified by the ionization energy loss (dE/dx) measured by the TPC.

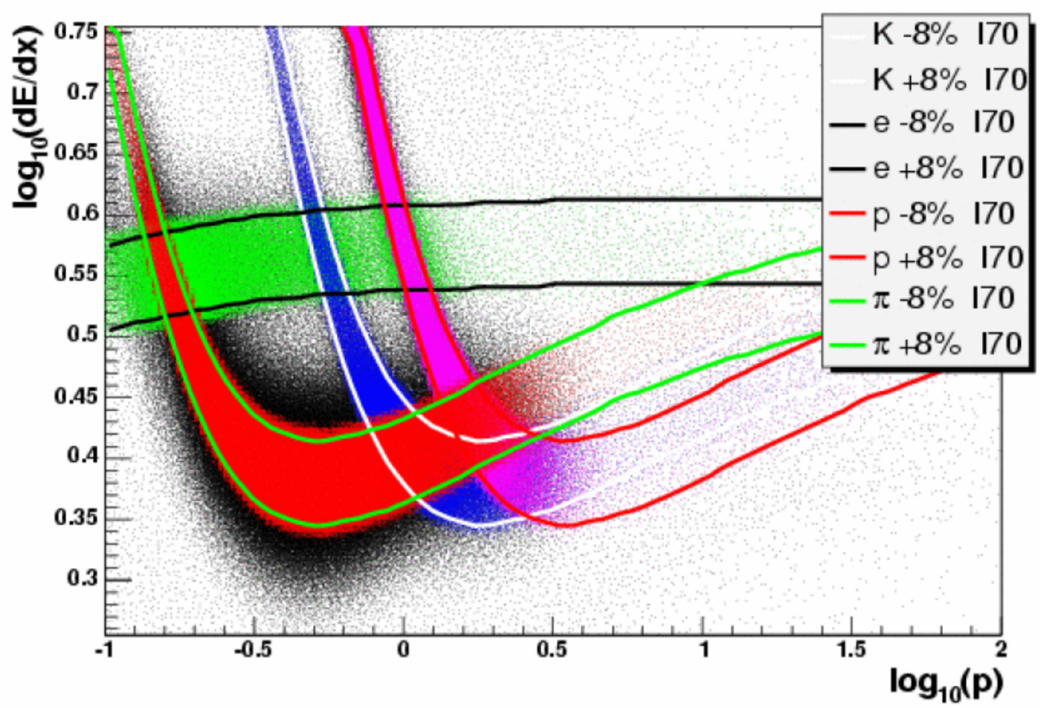

Fig. 2.7: The ionization energy loss (dE/dx) as a function of p_{T} for the charged particle at STAR.

2.3.3 Time Of Flight detector (TOF)

The TOF is designed to measure the time of flight for charged particles. It is another important device for particle identification, especially at low momentum [67, 68, 69]. The TOF covers 2π in azimuth direction and $|\eta| < 0.9$ in psedo-rapidity. The time of flight is the time interval from the start time of beam collisions to the stop time of particles reaching the TOF. The start time is measured by the Vertex Position Detector (VPD), while the stop time is measured by the TOF.

The VPD consists of two identical parts installed in the East and West of the STAR, located near the beam pipe. The distance of either slide of the VPD alone the Z direction respect to the center of STAR is 5.7 m, and the pseudo-rapidity acceptance is $4.24 \leq |\eta| \leq 5.1$. It not only can provide for the start time measurement, but also be used as a primary detector for minimum bias trigger, and vertex position measurement alone the Z direction, the vertex Z can be calculated as the following 2.2 [70]:

$$Z_{vtx} = c(T_{East} - T_{West})/2 \tag{2.2}$$

where T_{East} and T_{West} are the times measured by the VPD, c is the speed of light. The start time (the time when the collision happens) is given by:

$$T_{start} = (T_{East} + T_{West})/2 - L/c \tag{2.3}$$

where the L=5.7 m.

The TOF detector is based on the new technology of Multi-gap Resistive Plate Chamber (MRPC), which can provide excellent timing resolution, but with a relatively low cost. Fig. 2.8 shows the side view of an MRPC module for STAR. The MRPC is made of a stack of resistive plates (0.54-mm-thick float glass), with a series of uniform 220 μm gas gaps in between. A high voltage is applied on each gap. When a charged particle goes through the glass stack, some electrons and ions will be created by the ionization inside the gas gaps. The strong electric field will produce amplified avalanch signals.

The time of flight can be calculated by the time interval between TOF and VPD, the path length is measured by the TPC. Thus the velocity of the charge particle can be calculated based on the time of flight and path length.

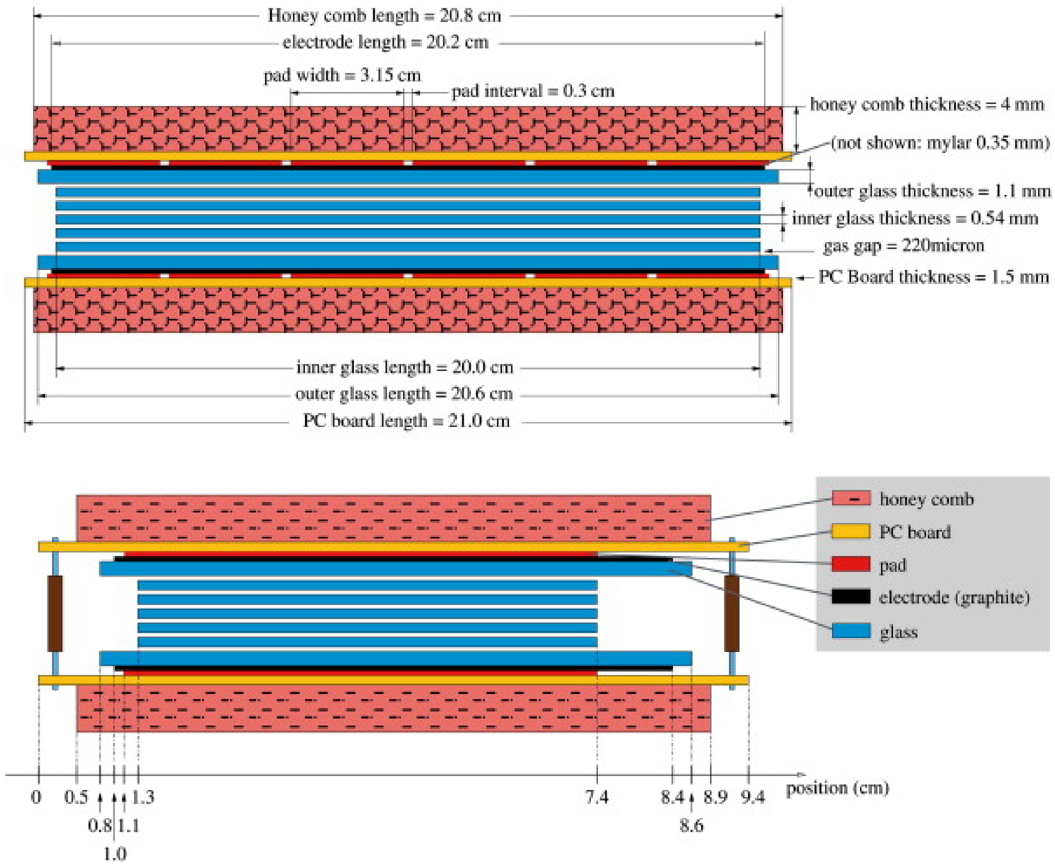

Fig. 2.8: The MRPC modules developed for Time OF Flight (TOF)

$$\frac{1}{\beta} = \frac{c\Delta t}{L} \tag{2.4}$$

Fig. 2.9 shows $1/\beta$ distribution as a function of transverse momentum p_{T} , where different color bands represent different particles.

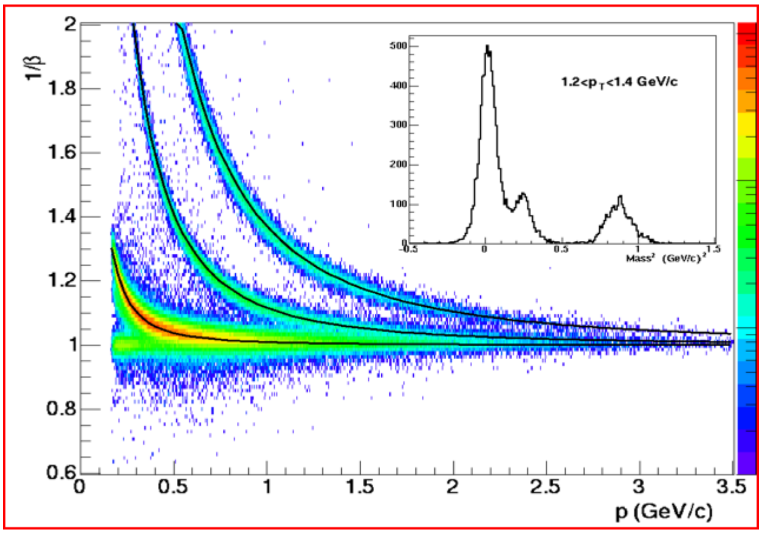

Fig. 2.9: $1/\beta$ distribution as a function of transverse momentum p_{T} .

2.3.4 Electro-Magnetic Calorimeter (BEMC)

The Barrel Electromagnetic Calorimeter (BEMC) is located outside of the TOF detector, covering $|\eta| < 1$ psendo-rapidty and 2π in azimuth. The inner radius is 220 cm, while the outer one is 250 cm [71]. The BEMC consists of 120 calorimeter modules, 60 modules for each side of the STAR, East and West side. Each modules is divided into 40 towers, 20 in η and 2 in ϕ. Every tower covers 0.05 for both $\Delta\eta$ and $\Delta\phi$. The STAR BEMC consists of 4800 towers in total. The side view of the BEMC is shown in Fig. 2.10. In each BEMC module, there are 21 active plastic layers, with 20 layers of lead in between, The total material budget for every module is about $20X_0$ radiation lengths at the mid-rapidity range.

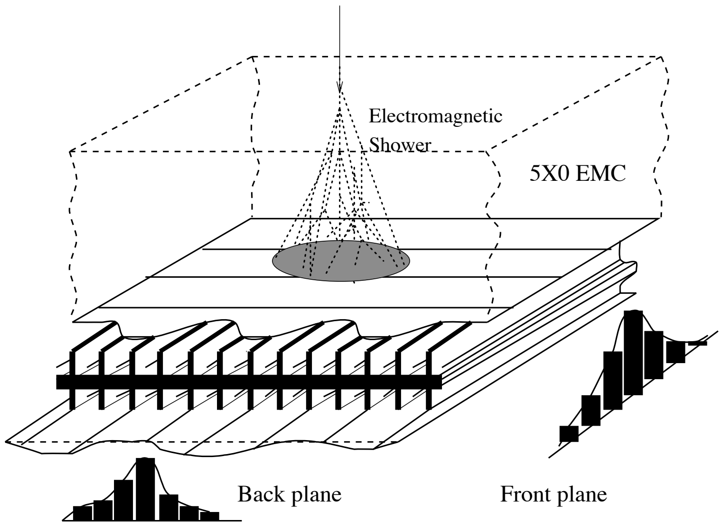

Fig. 2.10: Side view of a BEMC module developed for STAR.

There are two layers of Shower Maximum Detector (SMD), placed in the position of 5 radiation lengths from the beam line at mid-rapidty, the SMD have a very good spatial resolution both in the η and ϕ directions, which can be used to reconstruct shower position, and shape, The BSMD have two layers, with independent cathode planes with strips etched in the η and ϕ directions, respectively. allowing reconstruction of a two dimensional image of the shower as shown in Fig. 2.11. The strips resolution along η direction is 0.0064 and 0.1 in ϕ and 0.1 unity, respectively. The main purpose of this plane is to map out the shower profile both ϕ and η shape of shower. Basically, the BEMC provides the good energy measurements while the BSMD provides high spatial resolution for the electron identification.

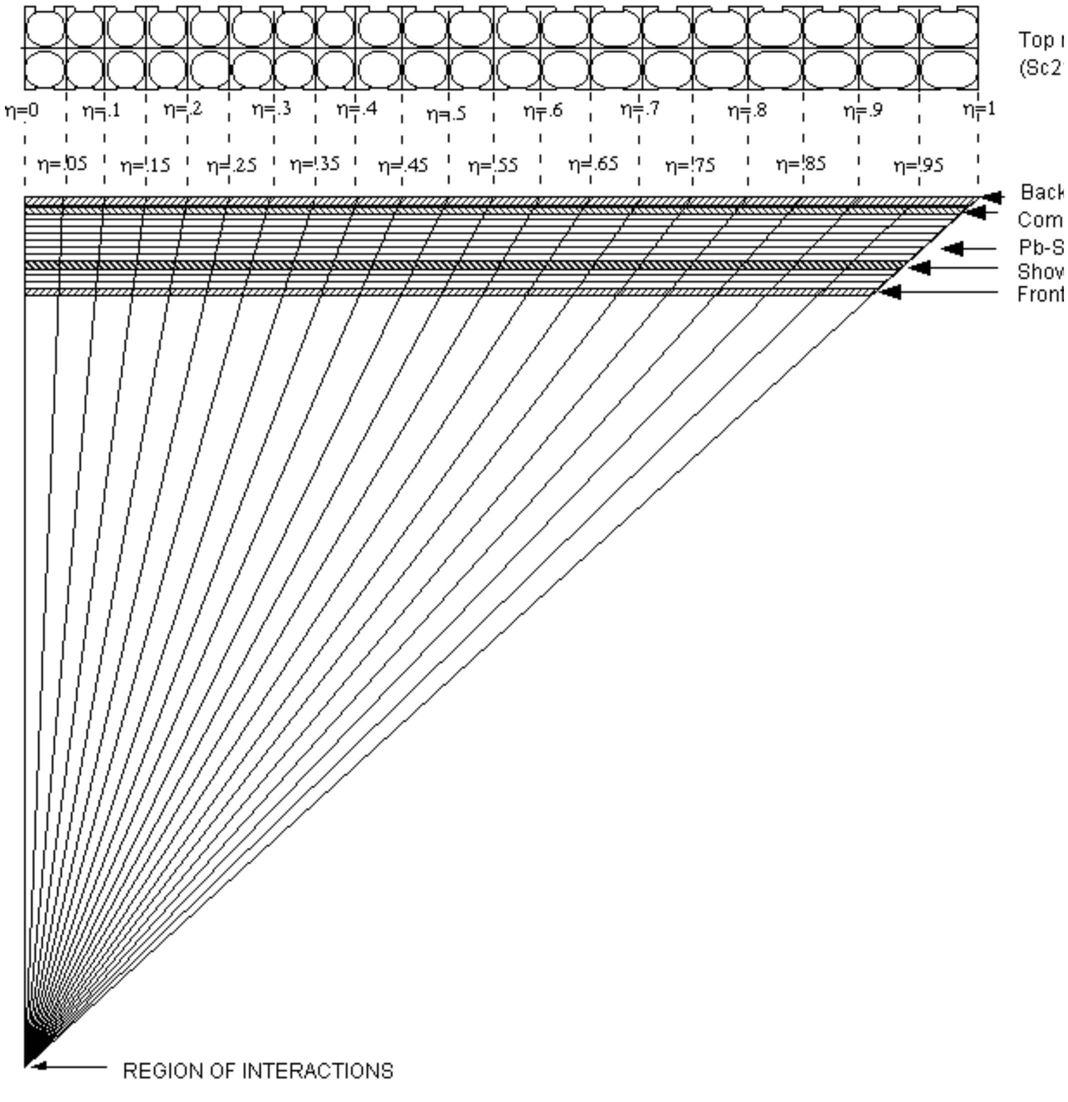

Fig. 2.11: Side and end views of the MRPC modules developed for STAR.

Electrons and photons deposit almost all of their energies in the BEMC. On the other hand, hadrons lose much less energy compared with electrons and photons. Therefore, electrons and photons can be identified by the energy deposit in the BEMC. The cluster consisted of four nearest towers, the electron deposit most of the energy in a single tower.

The total energy from these four towers record the energy for one track. The deposit energy on the cluster is almost equal to momentum for electrons, the ratio between momentum and energy or P/E in principle is close to 1 for electrons as shown in Fig. 2.12, while this ratio is much smaller than 1 for hadrons. The BSMD can identify the electrons based the shower shape, the electrons have a much larger shower shape compared with hadrons.

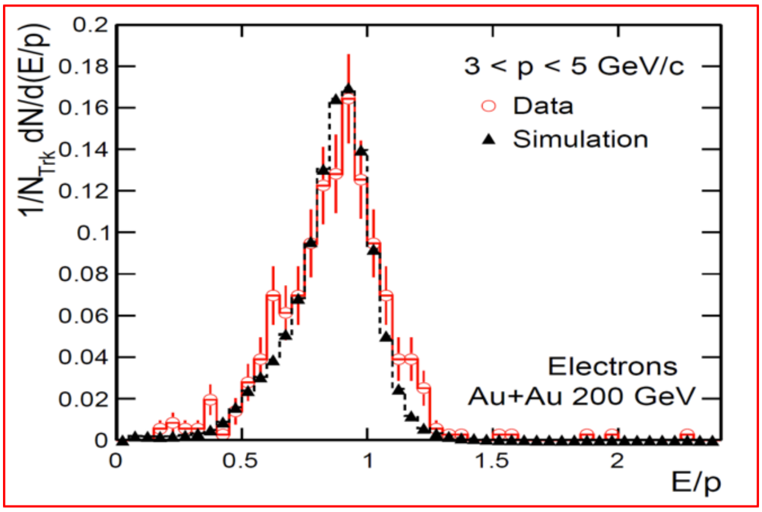

Fig. 2.12: The ratio between momentum and energy P/E distribution.

CHAPTER 3

Non-photonic electron production in p+p collisions at $\sqrt{s}$=200 GeV

3.1 The procedure for this analysis

In this analysis, the goal is to measure the non-photonic electrons (NPE) from open heavy flavor hadrons semi-leptonic decays (e.g. $D^0 \to K^- e^+ \nu_e$ and $B^0 \to D^- e^+ \nu_e$) in p+p collisions at $\sqrt{s}$=200 GeV.

The main sources of the non-photonic electrons (NPE):

- $D^0 \to e + X$ (B.R. 6.5%).
- $D^{\pm} \to e + X$ (B.R. 16%).
- $\Lambda_c \to e + X$ (B.R. 4.5%).
- $B \to e + X$ (B.R. 10%).

The essential steps for this analysis include the electron identification and background subtraction. The fist step is to apply all the track quality and electron identification cuts to select electron candidates which are referred to as inclusive electrons. The next step is to subtract the photonic electrons background from photo conversion and $pi^0 eta$ Dalitz decays, which can be reconstructed by the yield of unlike charge-sign pairs minus that of like charge-sign pairs with invariant mass $m_{ee} < 0.24$ GeV/c^2. Hadron background can be corrected using the inclusive electron purity. All the analysis details will be discussed in the following.

The main background electron sources are listed in below:

- The photonic electrons. The main photonic electron background are from gamma conversions which is from the detector materials, π^0 and η mesons Dalitz decays electrons, those electron background can be reconstructed by the unlike minus like sign method after applying a small invariant mass cuts, the details will be discussed in the latter sections 3.4.4.

- The mis-identified hadrons as electrons. Mis-identified hadron can be subtracted statistically by the inclusive electron purity, details will be discussed in the section 4.4.4.

- Drell-Yan and heavy quarkonia contributions ($J/\psi \to e^+e^-$). These contributions can be estimated by the simulation.

- Vector mesons (e.g. $\rho \to e^+e^-$,$\phi \to e^+e^-$.) dielectron decays electrons. These contributions can be estimated by the simulation.

- Single electrons from $Ke3$ decays, $Ke3$ ($K+ \to \pi^0 + e + \nu_e$), these contributions can be estimated by the simulation.

3.2 Dataset and event selection

The dataset for this analysis was recorded in p+p collisions at $\sqrt{s}$ =200 GeV record in the year of 2012 by STAR experiment. There are three different triggers used in this analysis, VPD Minimum-Bias (VPDMB) trigger for low transverse p_{T} , while the two BEMC triggers (HT0BBCMBTOF0, HT2BBCMB) for high transverse momentum p_{T} . The BEMC triggered or BEMC triggered events have a high p_{T} track with energy deposition in one single BEMC tower above a certain threshold, HT0 has the transverse energy threshold of E_T > 2.6 GeV and HT2 has the transverse energy threshold of E_T > 3.6 GeV. All of these datasets are produced under the STAR library SL12d.

The good events selection is based on TPC primary vertex Z (TpcVz), VPD vertex Z (vpdVz), both Vz defined as the distance between the measured vertex and the STAR center along the beam direction. The charged-particles multiplicity in p+p collisions is much lower than in Au+Au collisions, leading to worse p+p vertex quality is much worse than Au+Au, therefore, the vertex ranking cut was applied in the event selection.

The Minimum-bias and BEMC triggered HT0, HT2 good events selection cuts are listed in the table 4.4, Fig. 4.2 shows the primary vertex Z distribution from HT0 trigged events.

Table 3.1: Events selection for Run 2012 p+p 200 GeV collisions

Triggers	$\lvert TPC_{Vz}\rvert$ cm	Vertex Ranking	Good Events
VPDMB	< 35 $\lvert TPC_{Vz} - VPD_{Vz}\rvert$ <6	> 0	2.95e8
HT0BBCMBTOF0	< 35	> 0	1.67e7
HT2BBCMB	< 35	> 0	1.55e7

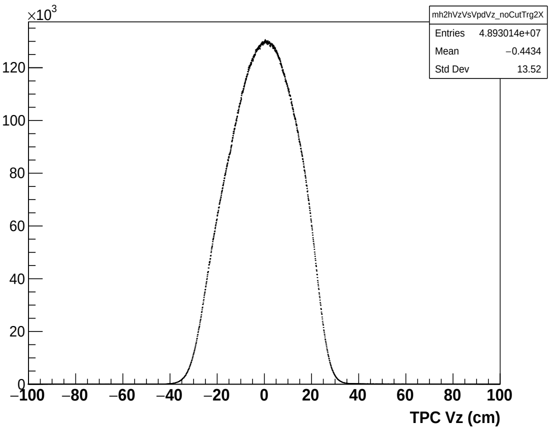

Fig. 3.1: TPC primary vertex Z distribution from MB trigged events.

3.3 Inclusive and photonic electrons selection from data

3.3.1 Track quality cuts

Tracks for charged particles were reconstructed from TPC hits. A minimum transverse momentum $p_{\mathrm{T}} > 0.2$ GeV cut was required to make sure all the tracks reach the TPC and avoid the ghost tracks. In order to improve the track reconstruction quality, some basic track quality cuts were applied, like the minimum number of the TPC hits (nHitsFit) to fit the track, the number of hits (nHitsDedx) for dE/dx calculation, and the distance of the closest approach between the track and the vertex (gDca). A cut on the position of the TPC point was applied to suppress photonic electron background from gamma conversion within the TPC. All the track quality requirements are listed in table 3.2. The track momentum was from the TPC hits only, without including the vertex position in the track reconstruction. The large distance between the production point and collision vertex for NPE electrons. Including the primary vertex in track reconstruction will lead to bias in momentum reconstruction.

Table 3.2: Track quality selection criteria for Run 2012 p+p 200 GeV data analysis.

	primary electron	partner electron
Transverse Momentum	$p_{\mathrm{T}} > 0.2$ GeV	$p_{\mathrm{T}} > 0.2$ GeV
Pseudo-rapidity	$\lvert\eta\rvert < 0.7$	
TPC Hits	nHitsFit $\geq$ 20	nHitsFit $\geq$ 15
$\frac{nHitsFit}{nHitsFitMax}$	≥ 0.52	
nHitsDedx	> 15	
gDcA	< 1.5 cm	
$R_{TPC^{1st}}$	<73 cm	

3.3.2 Electron identification cuts

- TPC ionization energy loss (dE/dx)

  The TPC not only provides the momentum measurement, but also particle identification via the ionization energy loss (dE/dx) in the TPC gas. In this analysis, the normalized dE/dx ($n\sigma_e$) was used for the electron identification:

$$n\sigma_e = \frac{\ln \frac{<dE/dx>^m}{<dE/dx>_e^{th}}}{R_{dE/dx}} \tag{3.1}$$

  where the $\langle dE/dx \rangle^m$ is the TPC measured energy loss (dE/dx), while the $\langle dE/dx \rangle^{th}$ is the theoretical values obtained from the Bichsel function [66], and $R_{dE/dx}$ is the experimental (dE/dx) resolution.

- Time of flight $1/\beta$

  The particle momentum and path length can be measured by the TPC, while the time of flight by the TOF. The mass can be calculated based on the momentum and velocity. However, as the momentum increases to higher $p_{\rm T}$, the mass effect is smaller and smaller, so the TOF detector particles identification capability working at low $p_{\rm T}$, up to 2GeV/c.

- The Barrel Electro-Magnetic Calorimeter (BEMC) and Shower Maximum Detector (BSMD)

  The electrons can be identified using the ratio between the energy deposit in the BEMC E/P. Electrons deposit most it's energies in the BEMC clusters, the E/P is near to 1 for electrons, while this ratio is much smaller for hadrons. As electrons deposit most of energies in a single tower, we take the highest tower energy E0 as the track energy deposition, the energy from this single highest tower marked as e^0.

The photonic electron pairs can be reconstructed by the e^+e^- mass and pair DCA method. In the photonic electrons pairs, the daughter that has tighter electron identification cuts was called the primary electron, while the other electron with looser cuts is referred to as partner electrons. The details for the photonic electron reconstruction cuts are listed in table 4.3

Table 3.3: Photonic electrons selection criteria for p+p run 2012 200 GeV collisions

	primary electron	partner electron
BEMC	$0.3 < p/e^0 < 1.5 (1GeV < p_T)$	
BSMD Match	$\lvert Dz\rvert < 3$ $\lvert D\phi\rvert < 0.015$ $(1GeV < p_T)$	
BSMD cuts	$1 <= N\eta$ $1 <= N\phi$ $(1GeV < p_T)$	
$n\sigma_e$	$-1 < n\sigma_e < 3$	
TOF β	$\lvert 1/\beta - 1\rvert < 0.3$	
TOF match	$Y_{local} < 1.8$	

The pure photonic electron pairs can be extracted by the unlike sign minus like sign method. The invariant mass ($m_{e^+e^-}$ < 0.24 GeV) and the measured distance-of-closest-approach between two daughters (Pair DCA e^+e^- < 1cm) cuts are applied enhance the photonic electron purity during the photonic electron reconstruction. The photonic electron invariant mass as a function of the primary electron p_{T} is shown in Fig. 3.2, where different panels are for different p_{T} bins, the black points stand for data, red curve is the STAR embedding simulation. As can be seen, embedding can describe the data quit well.

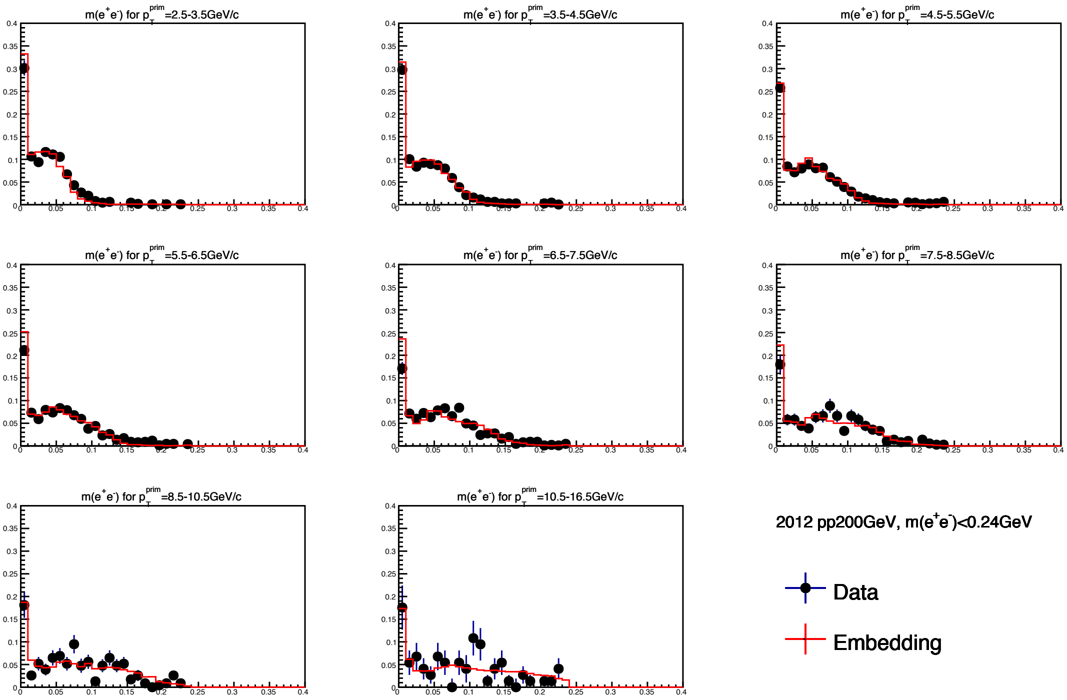

Fig. 3.2: Invariant mass distribution as a function of the primary electrons p_{T} from the photonic electron pairs.

3.4 Efficiency correction to the raw spectra

3.4.1 TPC Tracking efficiency

The TPC tracking efficiency and acceptance were obtained from the STAR embedding simulation. The basic idea is to reconstruct the embedded electrons in the simulation with data production chain and detector geometries structures. The detector responses can be extracted by comparing the MC and reconstructed tracks. In this way, the TPC acceptance and track reconstruction efficiency is obtained and shown on Fig 3.3. The left panel shows the tracking efficiency as a function of p_{T} from Minimum-Bias embedding sample and the right panel shows the efficiency as a function of p_{T} from BEMC-trigged embedding sample.

The systematic uncertainty for the TPC tracking efficiency was estimated by applying different track quality cuts, *i. e.* changing the "nhitfit" cuts from 20 to 25, and take the efficiency variation as the systematic uncertainty.

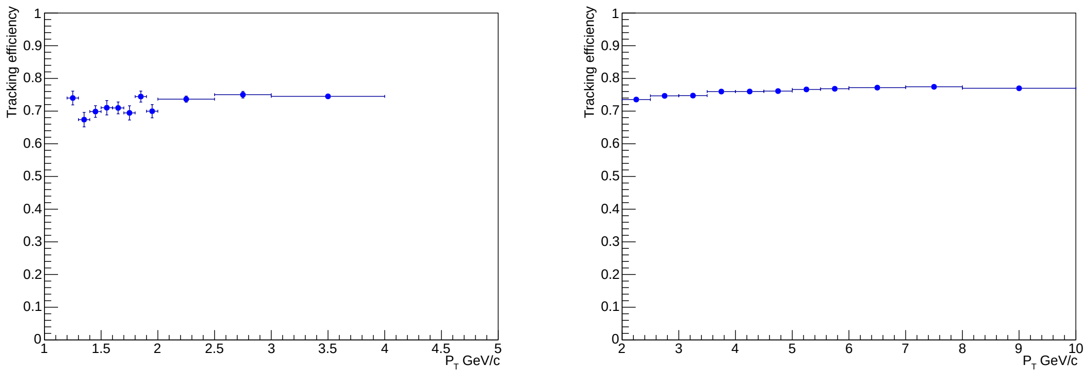

Fig. 3.3: TPC tracking efficiency and acceptance for as a function of p_{T} from the single electron and positron embedding. The left panel shows the efficiency from Minimum-Bias triggered events, the right panel shows the efficiency from BEMC triggered events.

3.4.2 Electron identification efficiency

- TOF cut $1/\beta$ efficiency

  The TOF $1/\beta$ ($|1/\beta - 1| < 0.03$) cut efficiency is calculated using the pure photonic electrons from data. The photonic electron reconstruction method is discussed in 3.3.2. We tighter the invariant mass cut from 0.24 GeV to 0.1 GeV in order to enhance the purity of the photonic electrons, and get rid of the hadron contaminations. Fig. 3.4 shows the $1/\beta$ 1 distribution from photonic electrons, different panels for different p_{T} bins.

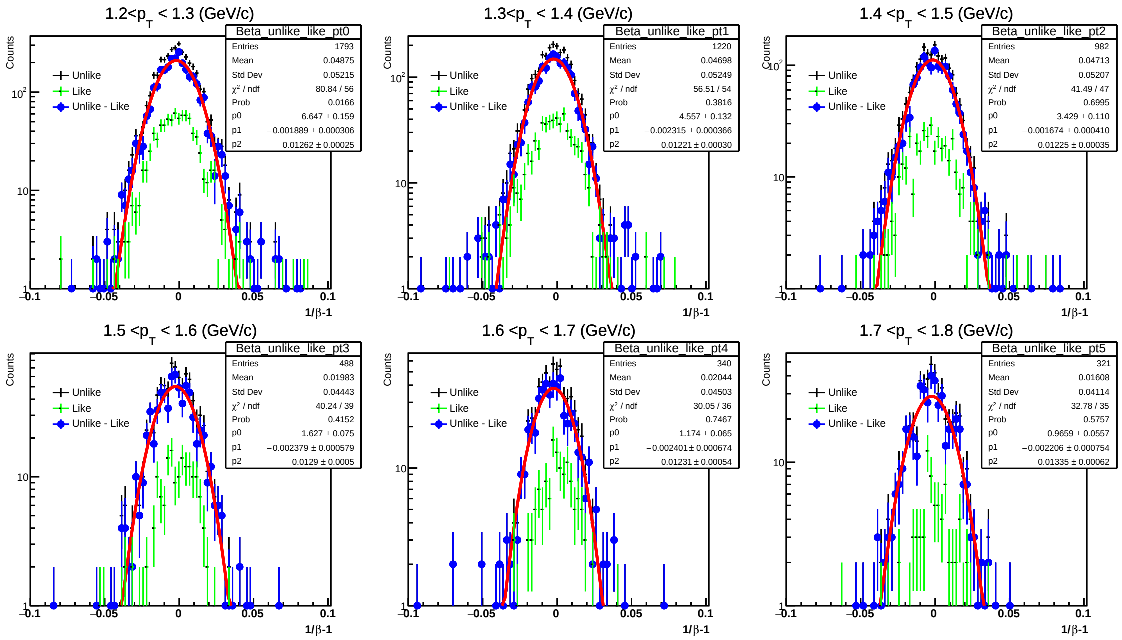

Fig. 3.4: $1/\beta$-1 distribution from the pure photonic electrons in different p_{T} bins.

The $1/\beta$-1 distribution was fitted by a single Gaussian function shown in Fig. 3.4. The $1/\beta$ cut efficiency was estimated by the Gaussian function parameter mean μ and the width σ value. The efficiency for every p_{T} bin is calculated by dividing an integral in (0.97, 1.03) range by an integral in (-5, 5) range in small momentum intervals:

$$\epsilon_{TOF(p_{\mathrm{T}})} = \frac{\int_{0.97}^{1.03} f(1/\beta, p_{\mathrm{T}})}{\int_{-5}^{5} f(1/\beta, p_{\mathrm{T}})} \tag{3.2}$$

The $1/\beta$ cut efficiency as a function of the p_{T} is shown in Fig. 3.5,

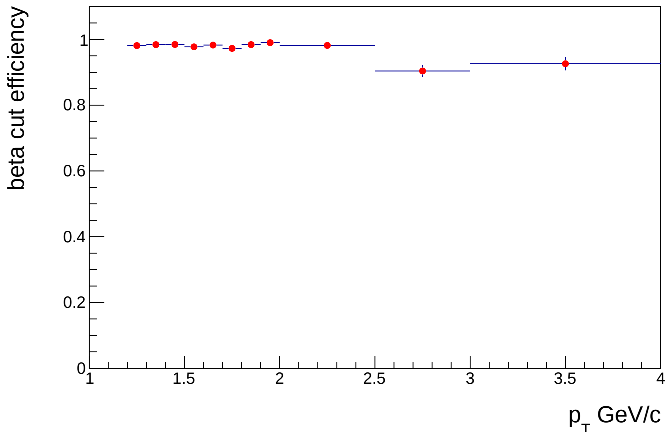

Fig. 3.5: The $1/\beta$ cut efficiency as a function of the p_{T} .

The systematic uncertainty for the $1/\beta$ cut efficiency is estimated fitted from the uncertainty of the Gaussian function mean μ and σ. Since the mean and sigma is correlated, we used the fitted mean and sigma to sample a two dimensional Gaussian distribution is shown in 3.6 right panel, and then calculated the $1/\beta$ cut efficiency from the two dimensional Gaussian, by repeating this procedure 5000 times, and get the efficiency distribution shown in Fig. 3.6 left panel. We used a Gaussian function to fit the efficiency distribution, and extract the sigma from the fit function as the $1/\beta$ systematic uncertainty.

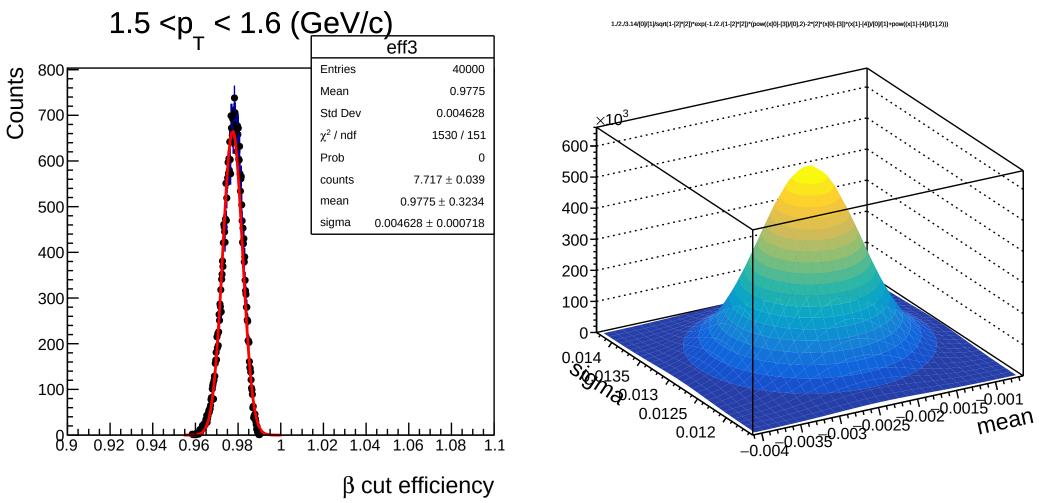

Fig. 3.6: Left panel shows the $1/\beta$ cut efficiency distribution. Right panel shows the $1/\beta$-1 distribution mean versus sigma.

- TOF match efficiency.

  Thanks for electrons need to match with a TOF hit and satisfy $|Y_{local}| < 1.8$ and $TOF_{match\ flag} > 0$. The TOF match efficiency is calculated based on the pure photonic electrons Eq. 3.3, the numerator is number of electrons passed the TOF match cuts, while the denominator is the number of electrons candidates regardless whether or not satisfy the TOF match cuts. Fig. 3.7 shows the TOF match efficiency as a function of p_{T} .

$$\epsilon_{TOF\,Match}(p_{\mathrm{T}}) = \frac{N^{e}_{Pass\,TOF\,Match}(p_{\mathrm{T}})}{(N^{e}_{TPC}(p_{\mathrm{T}})} \tag{3.3}$$

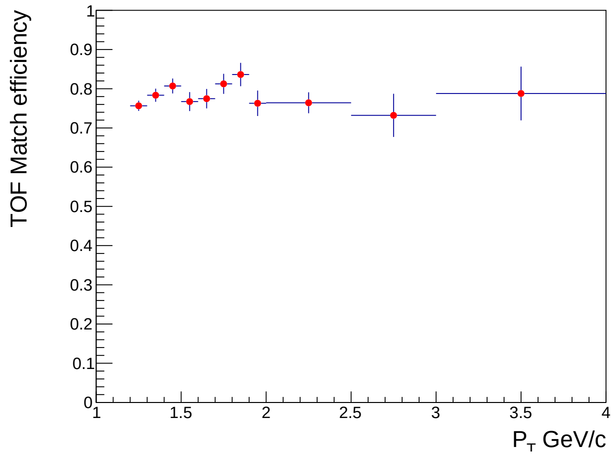

Fig. 3.7: TOF matching efficiency for electrons as a function of p_{T} .

- TPC electron identification efficiency.

  The TPC ionization energy loss dE/dx was used for electron identification in this analysis. We applied the normalized dE/dx (-1< $n\sigma_e$ <3) cut on the electrons. The cut efficiency are extracted from the photonic electrons sample from data. The efficiency is estimated based on photonic electrons $n\sigma_e$ distribution shown is Fig. 3.8. The electrons $n\sigma_e$ distribution has a Gaussian shape in a small momentum intervals. Therefore, we used a single Gaussian function to fit the $n\sigma_e$ distribution. The mean and sigma for electrons extracted from the Gaussian fit function parameters.

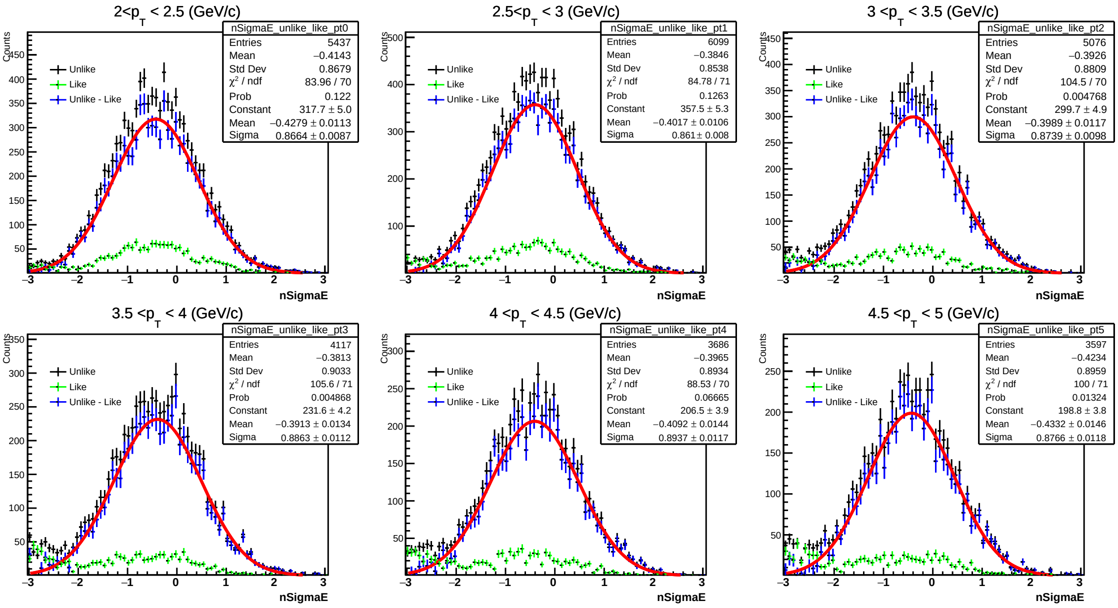

Fig. 3.8: Photonic electron nσ_e distribution in different p_{T} bins.

The TPC electron identification cut efficiency for the $n\sigma_e$ cut is calculated using the $n\sigma_e$ Gaussian fit function based on the Eq. 3.4,

$$\epsilon_{n\sigma_e} = \frac{\int_{-1}^{3} f(n\sigma_e, p_{\mathrm{T}})}{\int_{-5}^{5} f(n\sigma_e, p_{\mathrm{T}})} \tag{3.4}$$

The systematic uncertainty for the TPC $n\sigma_e$ cut efficiency was obtained from the same method with the TOF $1/\beta$ cut efficiency. Fig. 3.9 shows the TPC nσ_e cut efficiency as a function of the p_{T} . The left panel shows the efficiency for Minimum-Bias data sample, the right panel shows the efficiency for BEMC trigged sample.

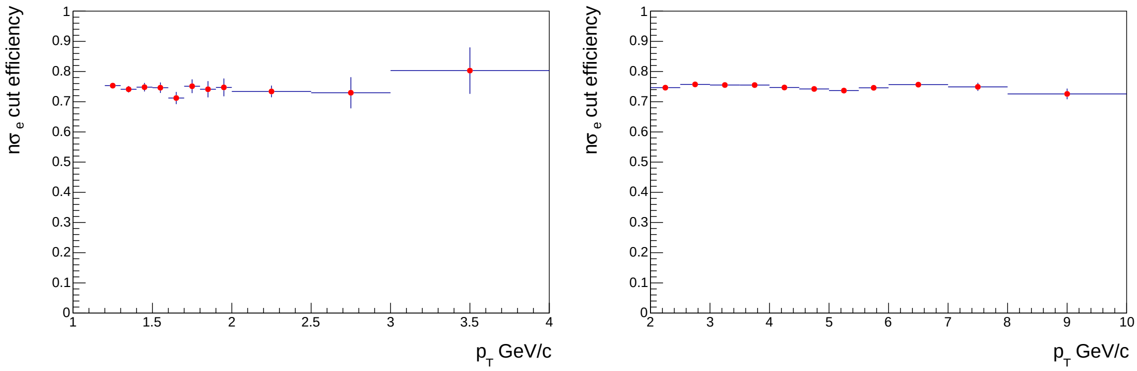

Fig. 3.9: TPC nσ_e cut efficiency for the single tracks, the efficiency was extracted from data, the left panel shows the efficiency from Minimum-Bias data sample, the right panel shows the efficiency from BEMC trigged sample.

- BEMC and BSMD cuts efficiency

  The BEMC and BSMD cut efficiency include the efficiency for BEMC match and cuts $0.3 < p/e^0 < 1.5$, while the BSMD cut is $1 < N\eta \&\& 1 < N\phi$ cut, and the BSMD match cuts $|Dz| < 3$,$|D\phi| < 0.015$ ($N\eta$ and $N\phi$ are the number of the SMD strip in the η and ϕ direction). Both the BEMC and BSMD efficiencies are extracted from data. In this analysis, the match and cut efficiency are calculated together, The efficiency calculation is based on Eq. 3.5. All the electron identification cuts are applied on the numerator, while the denominator does not have the BSMD and BEMC cuts.

$$\epsilon_{BEMC efficiency} = \frac{N^e_{Pass\,BEMC\,\&\,BSMD}(p_{\rm T})}{(N^e_{TPC}(p_{\rm T})} \tag{3.5}$$

  The systematic uncertainty is calculated based on the efficiency variation of different invariant mass cut, from 0.01 GeV to 0.05 and 0.15 GeV, respectively. The maximum deviation was taken as the systematic uncertainties. The BEMC and BSMD efficiency is shown in Fig. 3.10.

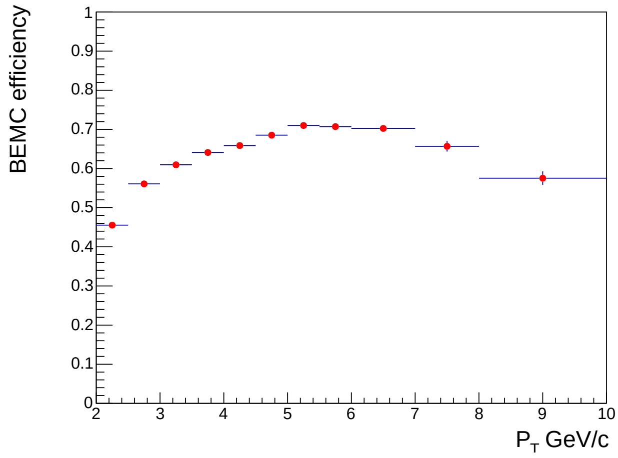

Fig. 3.10: The BEMC match and cut efficiency from the data.

3.4.3 BEMC trigger efficiency correction

In this analysis, a trigger simulator was used to simulate the BEMC response which mimic the real online configuration and figure out which electrons can fire the BEMC triggers. The offline adc0 was extracted from trigger simulator, which is the most energetic tower in a BTOW cluster and responsible for firing HT triggers. The online DsmAdc are linearly correlated with the offline adc0. The cut for HT0 ($11 < DsmAdc$) and HT2 ($18 < DsmAdc$), respectively. The trigger efficiency is estimated from the embedding simulation based on Eq. 3.6. The DsmAdc cut are applied on the numerator, while the denominator does not have the DsmAdc cut.

$$\epsilon_{Trigger} = \frac{N^{e}_{Threshold<DsmAdc}(p_{\mathrm{T}})}{(N^{e}_{No\,DsmAdc\,cuts}(p_{\mathrm{T}})} \tag{3.6}$$

The uncertainty for the trigger efficiency was calculated by the ROOT integrated function TGraphAsymmErrors, treating the efficiency as a parameter of a binomial distribution [72]. The trigger efficiency as a function of p_{T} is shown in Fig. 3.11, where the left panel is for the HT0 trigger efficiency while the right panel for the HT2.

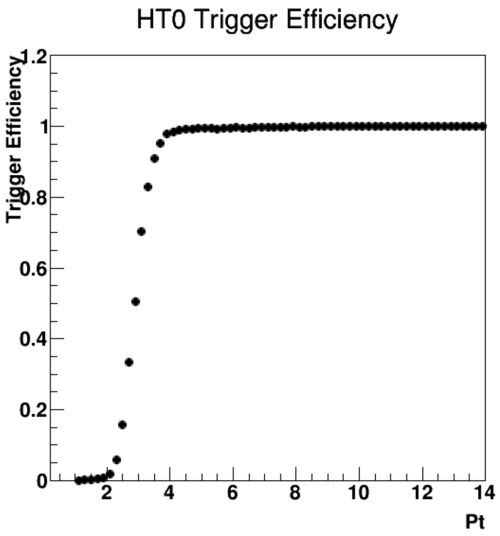

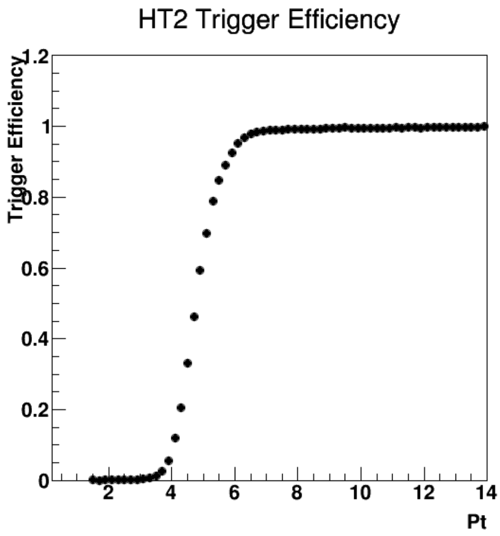

Fig. 3.11: BEMC trigger efficiency as a function of p_{T} , left panel for the HT0 trigger efficiency and right for the HT2 trigger efficiency, respectively.

3.4.4 Photonic electron reconstruction

One of the main background for this analysis is the photonic electrons which are from photo conversion in the detector material, π^0 and η mesons Dalitz decays. The photonic electrons reconstruction method has been discussed in section 3.3. The related cuts are listed in Table 4.3. Some of the photonic electrons can not be associated with a partner, due to the partner electrons were outside of the TPC acceptance or not reconstructed since the TPC efficiency is less than 100%. We need to correct the raw photonic electron background by the photonic electron reconstruction efficiency.

The photonic reconstruction efficiency is calculated using gamma, π^0 and η embedding, respectively. The efficiency is defined as the number of primary photonic electrons which are associated with a parter track in the same event with $m_{ee} < 0.24GeV$ and pair DCA < 1 cm, divided by the total number of photonic electrons in the embedding sample, the calculation equation:

$$\epsilon_{Phe} = \frac{N^{pairs}_{m_{e^+e^-}<0.24GeV\&pairDCA<1}(p_{\mathrm{T}})}{N^{e}_{single}(p_{\mathrm{T}})} \tag{3.7}$$

Since the gamma conversion, π^0 and η meson Dalitz decays reconstruction efficiency are not exact same, the total photonic electron reconstruction efficiency should be the combination of these three different photonic electron sources. The relative contribution to the total photonic electrons as a function of p_{T} is shown in Fig. 3.12, which is obtained from their parents invariant yield.

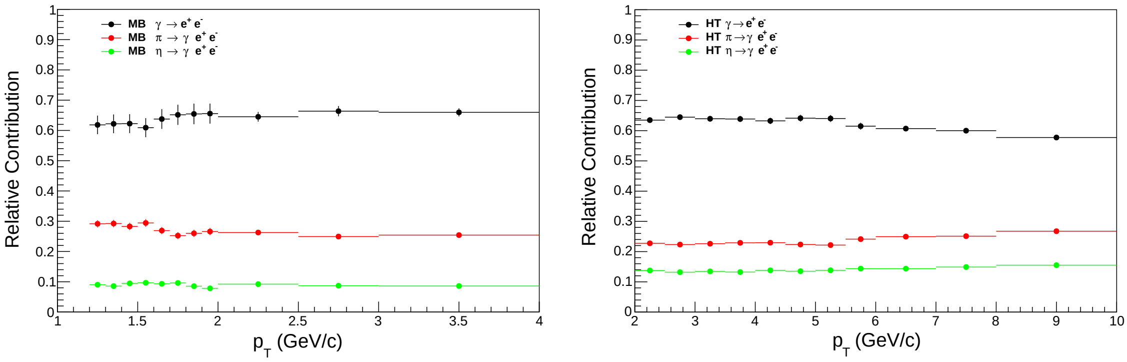

Fig. 3.12: Left panel shows the photonic electrons relative contribution to the total photonic electron as a function of p_{T} , right panel shows the same relative contribution but for BEMC triggered embedding sample.

The final photonic electrons reconstruction efficiency is the combination of the electrons from photo conversion and Dalitz decay, based on the Eq. 4.4:

$$
\begin{aligned}
PHE_{combined}(p_T) = & \frac{N_e^{\pi^0}(p_T)}{N_e^{\pi^0}(p_T) + N_e^{\eta}(p_T) + N_e^{\gamma}(p_T)}\epsilon_{Phe}(\pi^0) + \\
& \frac{N_e^{\eta}(p_T)}{N_e^{\pi^0}(p_T) + N_e^{\eta}(p_T) + N_e^{\gamma}(p_T)}\epsilon_{Phe}(\eta) + \\
& \frac{N_e^{\gamma}(p_T)}{N_e^{\pi^0}(p_T) + N_e^{\eta}(p_T) + N_e^{\gamma}(p_T)}\epsilon_{Phe}(\gamma)
\end{aligned} \tag{3.8}
$$

The uncertainty for the photonic electron reconstruction efficiency is estimated from two component. The statistical uncertainty regard as a parameter of a binomial distribution [72]. The systematic uncertainty is taken from the relative contribution from different photonic electron source. The final photonic electron reconstruction efficiency as a function of p_{T} is shown in Fig. 3.13, where the left panel is from the MB trigger and the right panel from the BEMC triggered events.

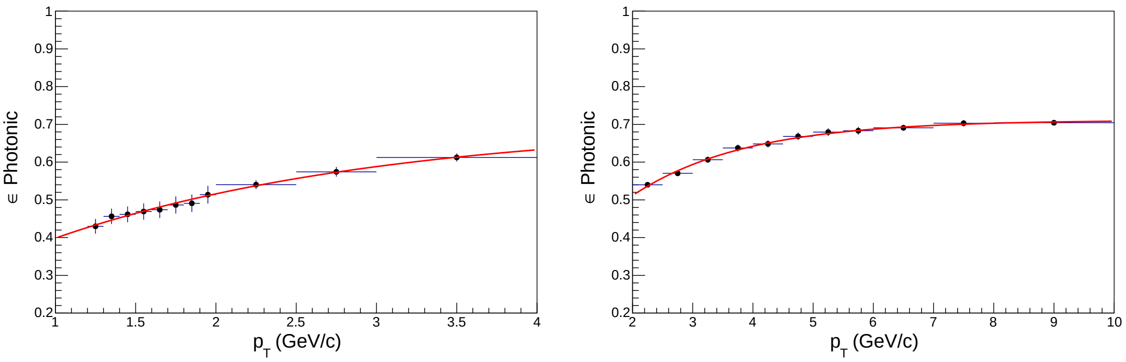

Fig. 3.13: photonic electron reconstruction efficiency as a function of p_{T} , left panel shows the efficiency from MB trigger and the right panel shows the high tower triggered sample.

3.4.5 hadron fraction estimation from electron purity fit

The other important background source is hadrons mis-identified as electrons, which can be corrected statistically by the inclusive electron purity, which is the hadron fraction in the inclusive electron candidates and was estimated from data by the Multi-Gaussian fits to the inclusive electrons nσ_e distribution.

In order to constrain the $n\sigma_e$ Multi-Gaussian fits, both the mean and width for electrons $n\sigma_e$ distribution can be obtained from the photonic electrons. Fig. 3.8 shows the nσ_e distribution fitted by a single Gaussian function. Fig. 3.14 shows the dependence of mean and sigma of $n\sigma_e$ as a function of p_{T} , a constant is used to fit the μ and σ. The uncertainty for the mean and sigma are from shifting the central value up and down as a certain value, the uncertainty can be covered by that value.

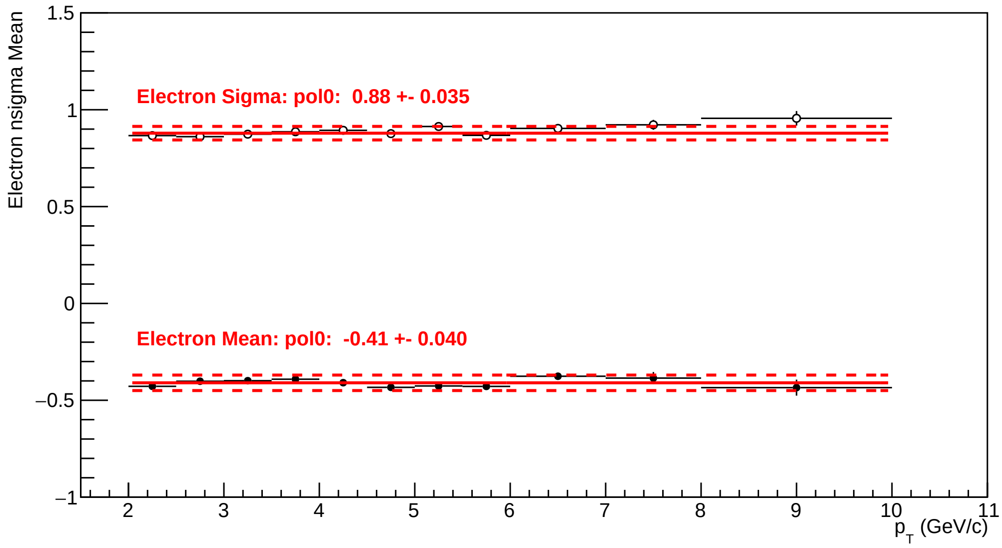

Fig. 3.14: Distributions of the mean and sigma from the Gaussian fit to nσ_e distributions as a function of p_{T} .

Purity of inclusive electron was estimated from constrained multi-Gaussian fit to the $n\sigma_e$ electron distributions. Every single Gaussian function in the fit represent a particle species and they are summed together to set the multi-Gaussian fit. We use a single Gaussians function describe the proton and kaon, since proton and kaon nσ_e mean are closer to each other. Figure. 3.15 shows the inclusive electron $n\sigma_e$ distribution fitted by a 3-Gaussian function. Here, all the cuts has been applied except the $n\sigma_e$. The electrons mean and width were constrained, the constrained limits estimated from the photonic electron $n\sigma_e$ shown in Fig. 3.14. There is no constrain on the hadron component. The purity of the inclusive electrons is calculated based on Eq. 3.9. It is a ratio of the integral of electron fit function (red curve) and the overall fit function (blue curve) in the range of (-1,3).

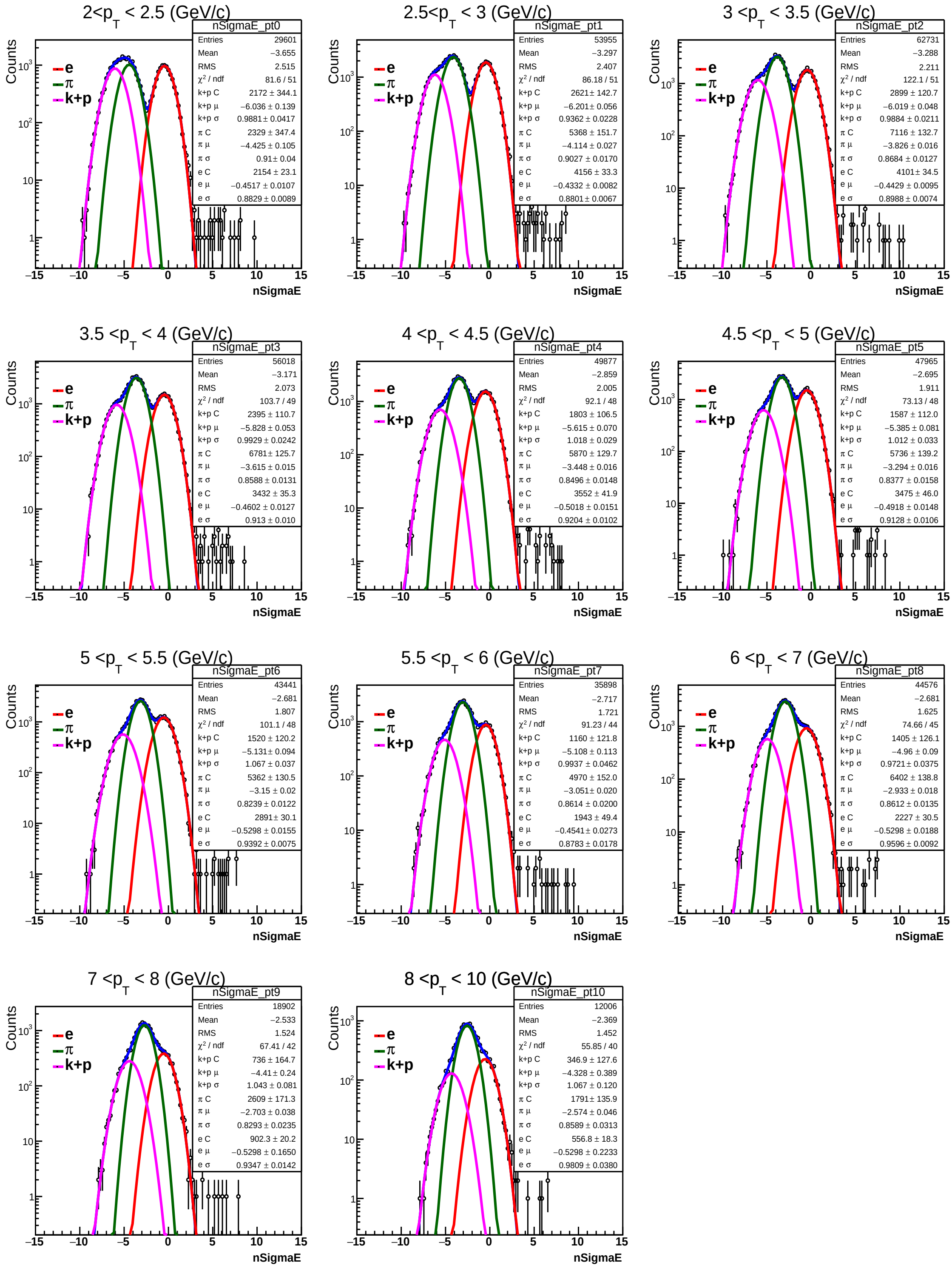

Fig. 3.15: The $n\sigma_e$ distribution for inclusive electrons (black points)and fitted by a multi-Gaussian function for different components, where different panels are for different p_{T} intervals.

$$purity = \frac{\int_{-1}^{3} f(electrons, p_{\mathrm{T}})}{\int_{-1}^{3} f(overall, p_{\mathrm{T}})} \tag{3.9}$$

The systematic uncertainty of the purity was estimated by varying the constraint on the multi-Gaussian fit, both the mean and width of the electron varied one, two and three standard deviations from their central values. The purity central value is the average of different constraint and the systematic uncertainty is maximum deviation from the mean in different constraints. Fig. 3.16 shows the inclusive electron purity as a function of p_{T} for different constraint.

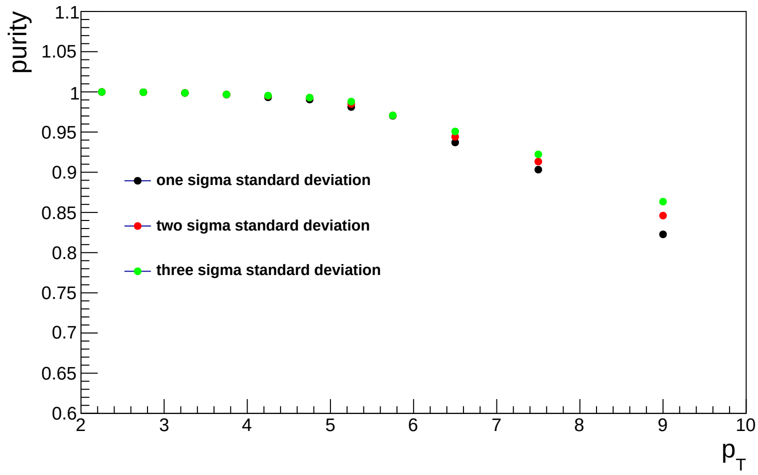

Fig. 3.16: The inclusive electrons purity as a function of p_{T} , different color represent different constrains.

The purity statistical uncertainty is estimated by a numberical method, which is to shift the inclusive $n\sigma_e$ up and down randomly according to a Gaussian distribution bin-by-bin, fit the distribution and estimate the purity. This procedure was repeated 1000 times for every p_{T} . The purity distribution from one of the p_{T} bin is shown in figure. 3.17. The sigma parameter from the Gaussian fit was taken as the statistical uncertainty.

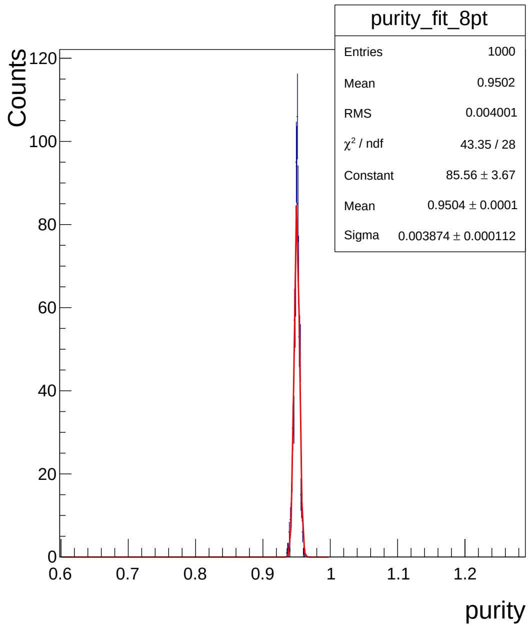

Fig. 3.17: The purity distribution from shifting the inclusive $n\sigma_e$ distribution up and down randomly 1000 times according to a Gaussian distribution.

The total uncertainties for the purity is the combination of the statistical and systematic uncertainties. Fig. 3.18 shows the purity as a function of p_{T} from MB (left) and BEMC triggered data (right).

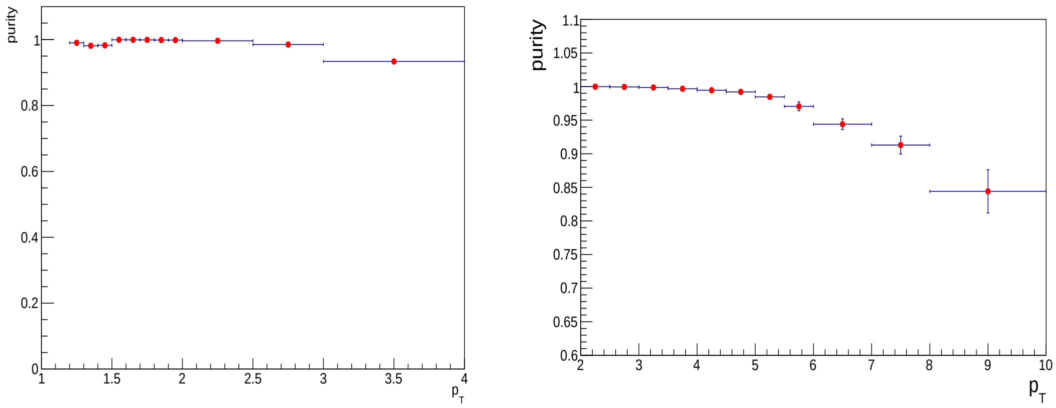

Fig. 3.18: Left panel shows the purity of inclusive electrons as a function of p_{T} from MB trigged data, right panel shows the purity from BEMC triggered data.

3.5 Result and discussion

After applying all the electron identification cuts, the raw p_{T} spectra for the inclusive and photonic electrons shows in the Fig. 3.19. The left panel shows the raw spectra of inclusive and photonic electrons as a function of p_{T} from MB triggered events while the right panel shows the raw spectra but for BEMC triggered events. These raw spectra have been corrected by the prescale factors, but no any efficiency correction.

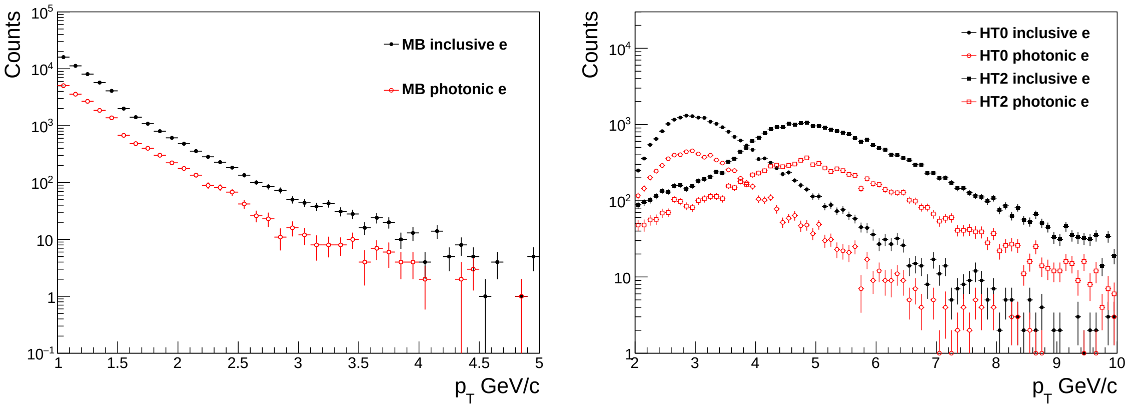

Fig. 3.19: Left panel shows the raw spectra of the inclusive and photonic electrons as a function of p_{T} from MB trigged data. Right panel shows the same spectra but for BEMC triggered data.

3.5.1 Non-photonic electron cross section in p+p collisions at $\sqrt{s}$=200 GeV.

In this section, we present the results of NPE cross section in p+p collisions at $\sqrt{s} =$ 200 GeV.

The raw yield of NPE is corrected by the hadron and photonic electron background contributions.

$$N_{NPE} = N_{inclusive} * purity - \frac{N_{PHE}}{\epsilon_{PHE}} \tag{3.10}$$

where the purity is estimated from data and us used for the hadron subtraction, and ϵ_{PHE} is obtained from embedding for those photonic electrons missing its partner during the photonic electron pair reconstruction. The NPE raw yield is corrected by the ePID efficiency, trigger efficiency, tracking efficiency and acceptance, the calculation based on the Eq. 3.11.

$$E\frac{d^3\sigma}{dp^3} = \frac{N_{NPE}\sigma_{NSD}}{2\pi p_T \Delta p_T N_{MB} \Delta\eta \epsilon_{trg}(p_T)\epsilon_{trk}(p_T)\epsilon_{ePID}(p_T)} \tag{3.11}$$

where $\epsilon_{trg}(p_T)$ is the BEMC trigger efficiency estimated from embedding and used for BEMC-triggered data. $\epsilon_{trk}(p_{\mathrm{T}})$ is track reconstruction efficiency and geometric acceptance estimated from embedding. σ_{NSD} is the total non-single diffractive (NSD) cross section, which is measured by STAR to be 30.0 ± 2.4 mb[34], N_{MB} is the total number of minimum-bias events used for the analysis. N_{NPE} is the raw NPE yield in every p_{T} bin within a rapidity window Δy.

Besides the background contribution from photonic electrons, and mis-identified hadrons, there are still a small fraction of Drell-Yan and electrons from J/ψ,Υ and light vector mesons (ρ, ω and ϕ) decays. The J/ψ production cross section in p+p collisions at middle rapidity has been measured by both STAR and PHENIX experiments [73, 74, 75] as shown in Fig. 3.20 left panel. The contribution from J/ψ decay electrons was subtracted from NPE cross section. Fig. 3.20 right panel shows the simulation study for Υ, Drell-Yan, light vector mesons (ρ, ω and ϕ) decay electrons [40], their contribution is smaller than the uncertainty of J/ψ decay electrons the vector mesons are subtracted from this analysis by simulation.

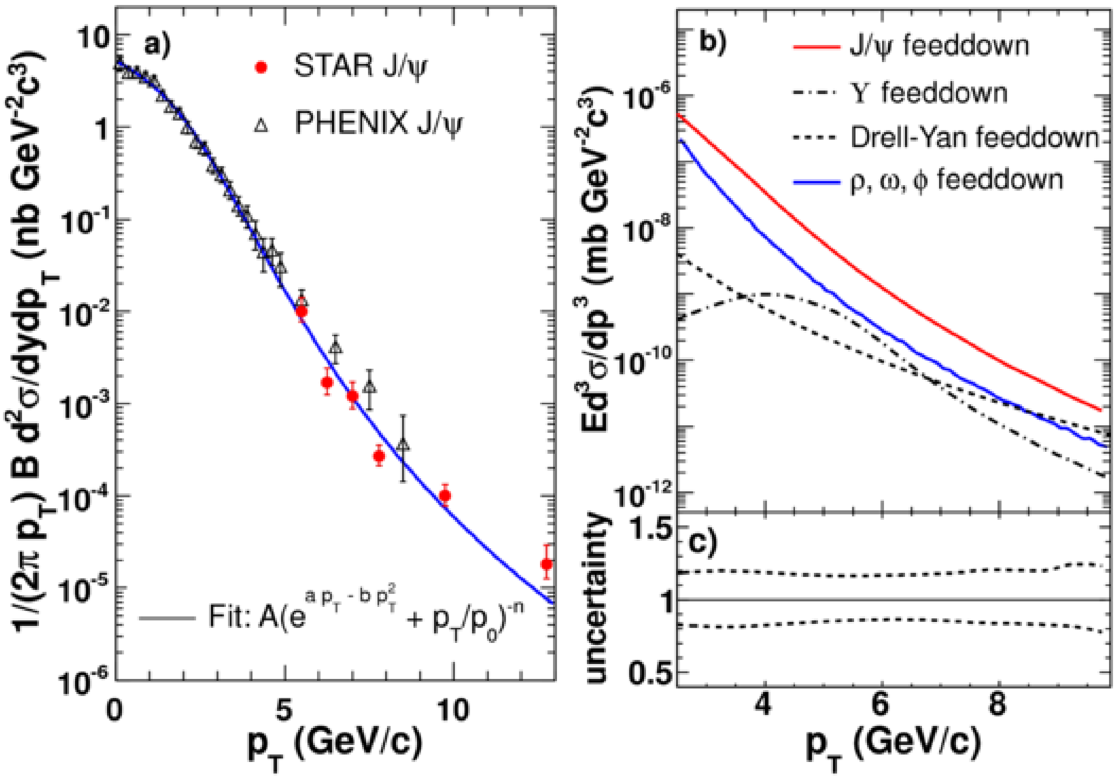

Fig. 3.20: The Left panel shows the J/ψ invariant yield measurement from STAR (closed circles) and PHENIX (open triangles), right panel shows the cross section of the electron from decays of J/ψ, Υ, Drell-Yan and light vector mesons feeddown to electrons and compare with the J/ψ decay electrons.

The measured NPE cross section in p+p collisions at $\sqrt{s}$=200 GeV using data from 2012 is shown in Fig. 3.21. The upper panel of Fig. 3.21 is a comparison of this analysis, the STAR's previous measurement using data from 2005 and 2008 (black points) [40] and the perturbative Quantum Chromo-Dynamics (pQCD) Fixed-Order Next-to-Leading Logarithm (FONLL) calculation (blue curves) [76]. The lower panel shows a ratio of data to FONLL calculation. This new measurement extends the p_{T} coverage to both lower and higher values than the previous STAR measurement with significantly better precision. The new result confirms the FONLL prediction and can also provide further constraints on such model calculations [77].

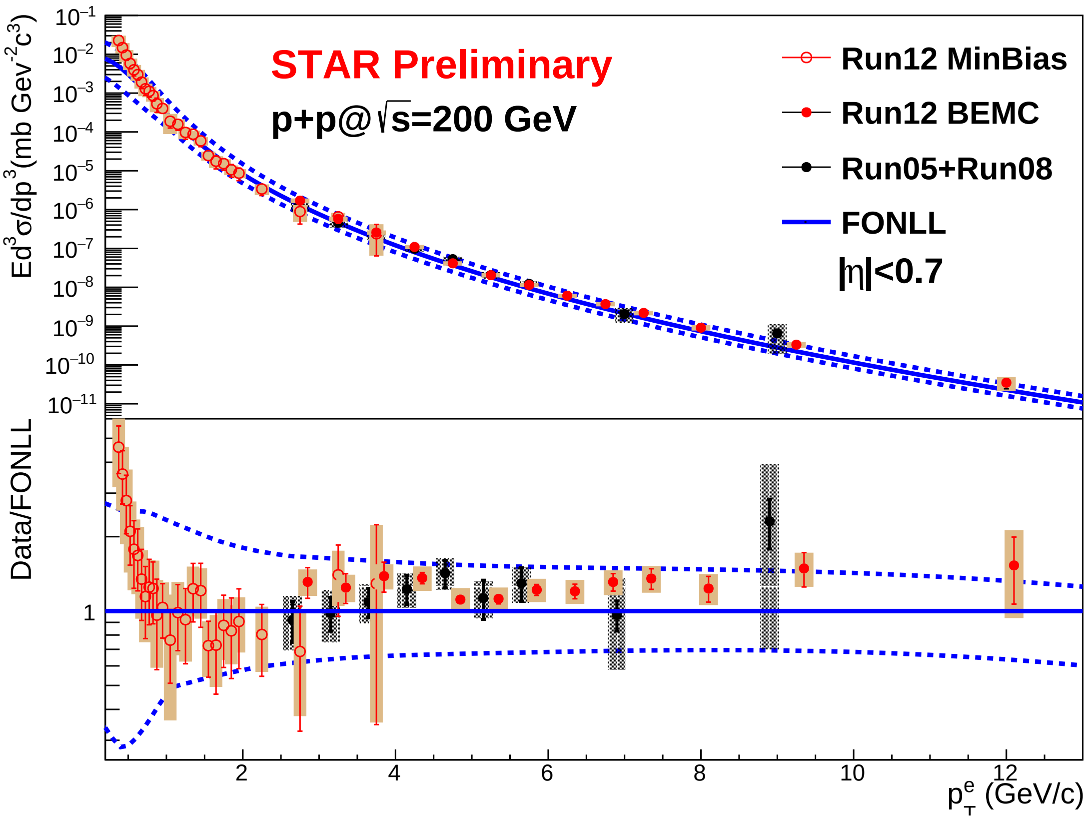

Fig. 3.21: Top panel: Non-photonic electron cross section in p+p collision at $\sqrt{s_{NN}}$=200 GeV from RHIC run 2012. The red points are this analysis, black points are STAR's previous measurement in RHIC run 2005+2008, and the blue curve is pQCD FONLL calculation. Bottom panel: The ratio of the data and pQCD calculation. The vertical lines are statistical uncertainties and shaded boxes are systematic uncertainties from the measurements.

3.5.2 Non-photonic electron nuclear modification factor

The nuclear modification factor (R_{AA}) was obtained in Au+Au collisions at $\sqrt{s_{NN}}$=200 GeV using the new, improved p+p reference as shown in Fig. 3.22. The data show significant suppression at high p_T in the most central Au+Au collisions, and the suppression reduces gradually towards more peripheral collisions. The results also show an enhancement at low p_T across all collision centrality intervals, but with large systematic uncertainties. The measured R_{AA} in the 0-10% centrality interval is compared with different model calculations. The gluon radiation scenario (DGLV) model [78] can not describe the large suppresion of NPE R_{AA} at high p$_T$. After adding the collisional energy loss, the model calculation is consistent with the data for p_T > 2.5 GeV/c. The collisional dissociation model [79], He et al. [80, 81], and the Gossiaux et al. models [82, 83, 84] have some challenge to describe the data [77].

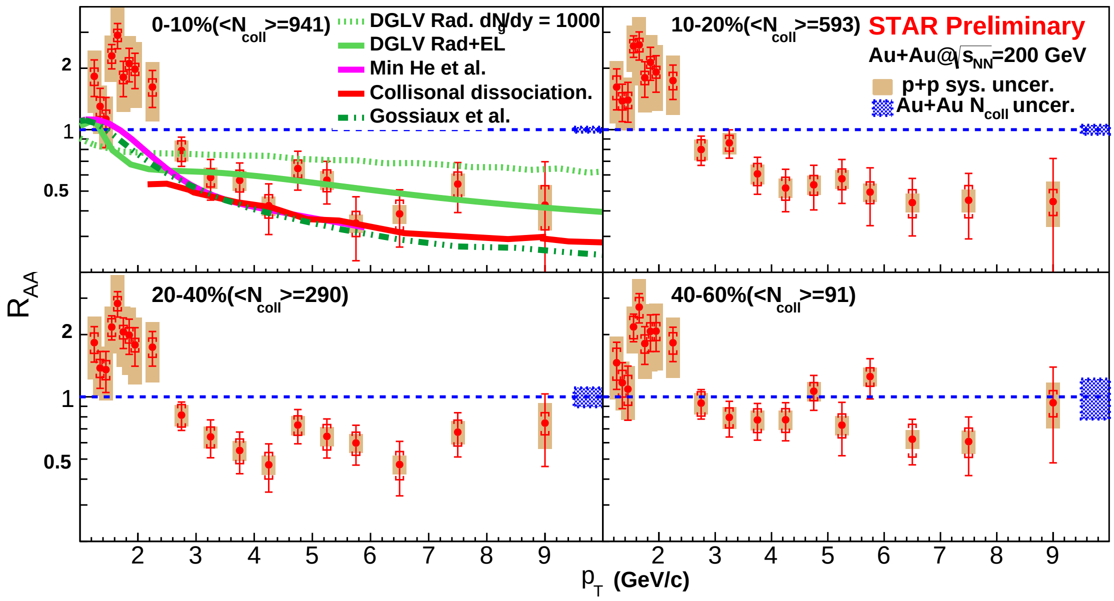

Fig. 3.22: Nuclear modification factor R_{AA} in Au+Au collisions at $\sqrt{s_{NN}}$=200 GeV for different collision centralities and compared with model calculations for 0-10% most central collisions, the vertical lines show the combined statistical uncertainties in p+p and Au+Au collisons, while the shaded boxes and square brackets indicate the systematic uncertainties in p+p and Au+Au collisions, respectively.

CHAPTER 4

Measurements of open bottom and charm hadron production in Au+Au collisions at $\sqrt{s_{NN}}$ = 200 GeV

4.1 The motivation and procedures for this analysis

In this analysis, the primary goal is to measure the open bottom and charm production in in Au+Au collisions at $\sqrt{s_{NN}}$ = 200 GeV, which is studied by the measurement the electrons from the open heavy flavor hadrons via semi-leptonic decays. This is the fist time at STAR measured the charm and bottom quark production separately in heavy-ion collisions by the track impact parameter method. Fig. 4.1 shows the flavor dependent parton medium interactions, nuclear modification factors R_{AA} as a function of p_{T} from model calculation [85]. Therefore, this measurement is crucial to investigate the flavor dependent parton energy loss mechanism, and advances our understanding of the properties of the QGP.

The Heavy Flavor Tracker (HFT), fully installed at the STAR experiment since 2014, provides excellent resolution to measure the Distance of Closest Approach (DCA) between reconstructed primary vertices and tracks. The HFT details have been discussed in chapter 2 section 2.3.1. The HFT can provides the DCA resolution up to 30 μm for momentum p = 1.5 GeV/c, which enables the separation of non-photonic electron (NPE) produced from D- and B-meson decays.

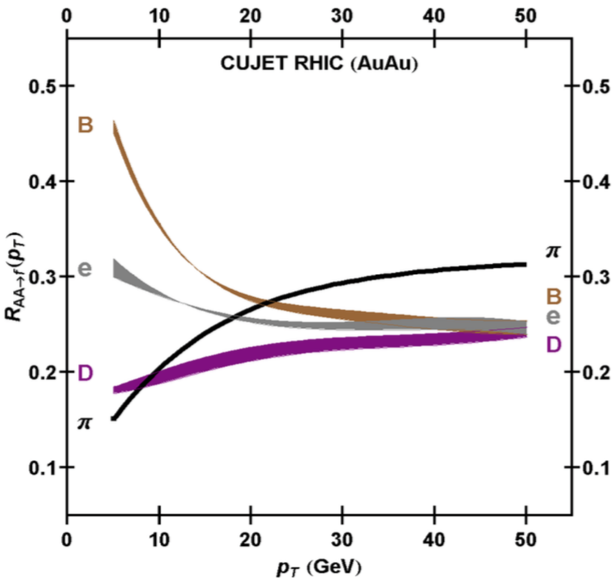

Fig. 4.1: Flavor dependent nuclear modification factors as a function of transverse momentum p_{T} at mid-rapidity for π, D, B and e in Au+Au 0-5% centrality interval.

The main procedures for this analysis are listde as flowing:

- Inclusive and photonic electrons selection from data. Applying all the track quality and electron identification cut criteria to select the electrons candidates as inclusive electrons, while the photonic electrons are reconstructed by the invariant mass and unlike minus like sign method, more details are discussed in section 4.2.

- The DCA template extraction for both measured signal and background. The DCA template for open heavy flavor hadrons decayed electrons DCA is obtained from HFT+EvtGen data driven simulation. The photonic electron background template are generated from Hijing simulation, and hadron background template are obtained from data, more detais are in section 4.3, section 4.4.1 and 4.4.4, respectively.

- The fraction of B hadron decayed electron contributed to the inclusive NPE ($\frac{N_{eB}}{(N_{eD}+N_{eB})}$) is extracted from template fit, more discussion are indruduced in section 4.5.

4.1.1 Dataset and event selection

The datasets for this analysis were taken in the year of 2014 in Au+Au collisions at $\sqrt{s_{NN}}$ = 200. It is the first year of physics running with the new STAR heavy flavor tracker detector. Both Minimum-Bias and BEMC triggered events are selected for this analysis, and the data was produced under the STAR library SL16d . The event selection based on the TPC primary vertex Z (TpcVz), and the difference between TpcVz and vertex position detector vertex Z (vpdVz). Since the VPD is a fast detector can be used for the pileup events rejection. The event selection cuts criteria are listed in the table 4.1. The TPC Vz versus VPD Vz is shown in Fig. 4.2 left panel and TPC Vz distribution rignt panel for high tower trigger 2 (HT2), the difinition of the different trigger have been discussed in the section 3.2. The multiplicities in Au+Au collisions is much higher than p+p collisions, leading to better vertex quality in Au+Au collisions. In this analysis, the MB triggered and BEMC triggered events are combined to increase the statistics.

Table 4.1: Events selection cuts for Run 2014 Au+Au 200 GeV collisions

Triggers	$\lvert TPC_{Vz}\rvert$ cm	$\lvert VPD_{V_z} - TPC_{Vz}\rvert$ cm	accept # Events
MB	< 6	< 3	853M
HT1	< 6	< 3	39.5M
HT2	< 6	< 3	48.9M
HT3	< 6	no cuts	14.7M

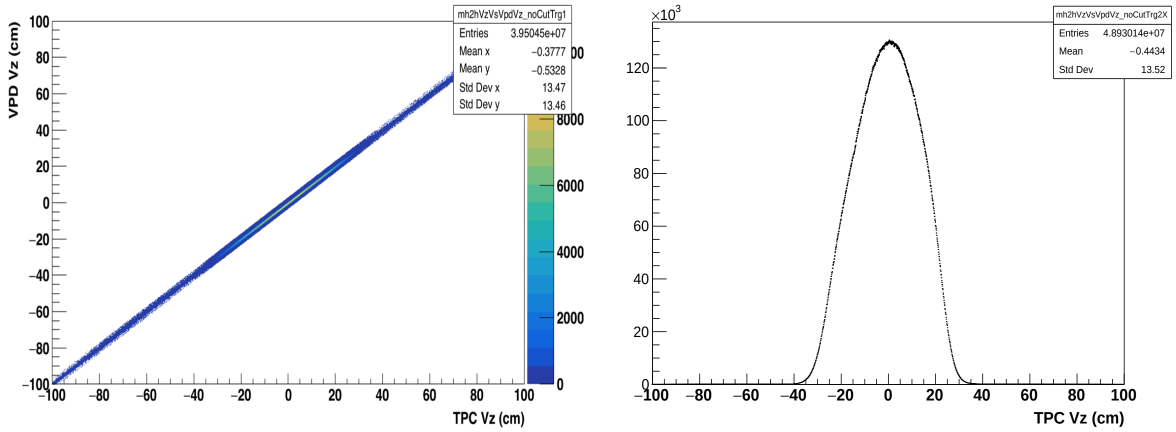

Fig. 4.2: Left: VPD Vz versus TPC Vz before vertex cuts from MB triggered vents. Right: TPC Vz before vertex cuts from MB trigged events.

4.2 Inclusive electrons selection from data

4.2.1 Track quality cuts

The tracks for this analysis are reconstructed based on the TPC hits from charged particles. Since the finite TPC acceptance, which is discussed in the previous chapter 2.3.2, a maximum pseudo-rapidity and minimum transverse momentum cut are required, the pseudo-rapidity coverage is $-1 < \eta < 1$ and transverse momentum p_{T} greater than 0.2 GeV/c, minimum p_{T} cut to make sure all the tracks avoid the ghost tracks. In order to improve the track reconstruction quality, the main track quality cuts is minimum number of the reconstructed hits (nHitsFit) to fit the track, and the number of hits (nHitsDedx) for dE/dx calculations, since we used the TPC energy loose dE/dx for the electron identification. The distance of closest approach between the track and the vertex (gDca). We did't apply the first TPC point cut in this analysis, due to we have a new detector HFT, which is more efficient to suppress the photonic electron background from gamma conversion with a larger radius compared to the first TPC point radius, the basic track quality cuts are similar to the previous p+p analysis, but still has more special requirements as listed in the table 4.2. The tracking parameters including the momentum are from the global tracks, since the large distance between the production points and collision vertex for the gamma conversion electrons, this will leading to the momentum distorted for the primary momentums.

The Fig. 4.3 shows the distributions of the reconstructed photonic electron conversion radius with and without HFT matching requirements. Since the HFT is very closer to the beam pipe (radius of its first inner layer is 2.9 cm), the HFT match can reject those electrons that are from gamma with a larger conversion radius, the photonic electron is the main background in this analysis. Fig. 4.3 shows the reconstructed conversion radius distributions of photonic electron candidates from 2014 MB data in Au+Au collisions at $\sqrt{s_{NN}}$=200 GeV. As we can see, the HFT match requirements can significantly suppress photonic electron background, which is the other benefit from HFT detector except the excellent DCA resolution.

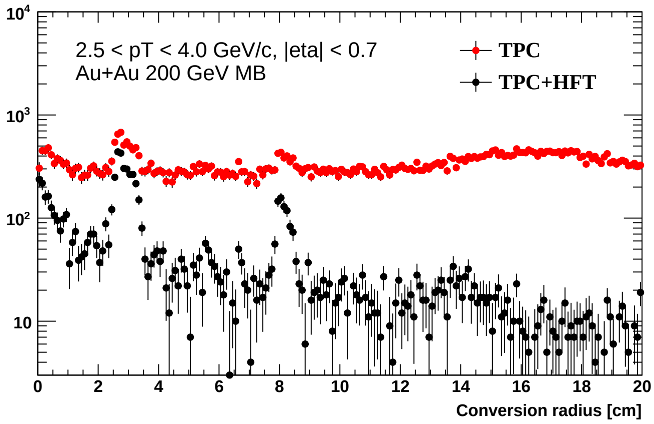

Fig. 4.3: Reconstructed conversion radius distributions of photonic electron candidates from 2014 MB data in Au+Au collisions at $\sqrt{s_{NN}}$=200 GeV. The red (black) points are before (after) requiring that tracks have hits from at least three HFT layers.

Table 4.2: Track quality selection criteria for Au+Au collisions at 200 GeV

	primary electron	partner electron
Transverse Momentum	0.2 GeV p_{T}	0.2 GeV p_{T}
Pseudorapidity	$\lvert\eta\rvert$ < 0.7	$\lvert\eta\rvert$ < 1
Spatial Hits	20 <= nHitsFit	15 <= nHitsFit
dE/dx Hits	15<=nHitsDedx	
Dca	dca < 1.5cm	dca < 3cm
HFT	At least three HFT hits	

4.2.2 Electron identification cuts

The electron selection method is very similar to the previous p+p analysis, but there are some minor differences mentioned in below items:

- TPC ionization energy loss (dE/dx)

The TPC used for the momentum measurements and particles identification for charged particles via the ionization energy loss (dE/dx). The normalized dE/dx ($n\sigma_e$) is used for the electrons identification [86], which is defined in Eq. 3.1, and Fig. 4.4 shows the normalized dE/dx ($n\sigma_e$) as a function of momentum.

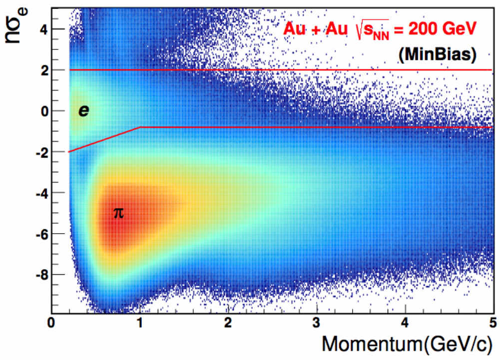

Fig. 4.4: Normalized dE/dx ($n\sigma_e$) versus momentum (p) distributions for all charged particles.

- Time of Flight (β)

  The time of flight is measured by the TOF. The masses for the different particles are calculated based on the momentum and velocity, the velocity is related to the time of flight. Therefore, the particle identification depends on the masses difference, the details are discussed in previous 2.3.3. Here we tight the $|1/\beta - 1| < 0.025$ instead of $|1/\beta - 1| < 0.03$ used in previous p+p analysis. Fig. 4.5 shows the $1/\beta$ distribution as a function of momentum for in Au+Au collisions at $\sqrt{s_{NN}}$ = 200 GeV.

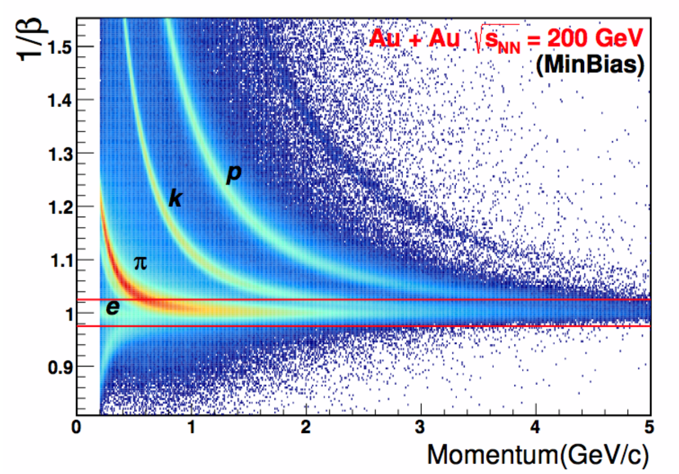

Fig. 4.5: $1/\beta$ as a function of momentum (p) distributions for all charged particles.

- The Barrel Electro-Magnetic Calorimeter (BEMC).

  The electrons are identified by the energy deposit from BEMC and momentum ratio. We applied ratio cut of menmentum over energy cut as 0.3 <p/e<1.5, and this is same with the previous as used in p+p analysis. However, we removed the shower maximum detector (BSMD) cut in this analysis, since the BSMD cut has no significant improvement for the electron purity but lost almost 50% statistics.

Table 4.3: Photonic electrons selection criteria for Au+Au run 2014 200 GeV collisions

	primary electron	partner electron
Transverse Momentum	0.2 GeV p_{T}	0.2 GeV p_{T}
Pseudo-rapidity	$\lvert\eta\rvert < 0.7$	$\lvert\eta\rvert < 1$
Spatial Hits	20 <= nHitsFit	15 <= nHitsFit
dE/dx Hits	15<=nHitsDedx	
Dca	dca < 1.5cm	dca < 3cm
BEMC	$0.3 < p/e0 < 1.5(1GeV < p_T)$	
BEMC Match	$\lvert Dz\rvert < 3$ $\lvert D\phi\rvert < 0.015$ $(1GeV < p_T)$	
$n\sigma_e$	$-1 < n\sigma_e < 3$	$-3.5 < n\sigma_e < 3.5$
TOFβ	$\lvert 1/\beta - 1\rvert < 0.25$ $(p_T < 4GeV)$	

After applying all the track quality cuts and electron identification cuts, the raw DCA$_{XY}$ distribution for the inclusive electron candidates from data in Au+Au collisions at $\sqrt{s_{NN}}$=200 GeV is shown in Fig. 4.6, different panel represent different p_{T} intervals. Currently, this analysis focused on the higher p_{T} , since we don't have a good control on the low p_{T} (p_{T} <2 GeV/c) HFT mis-match effect.

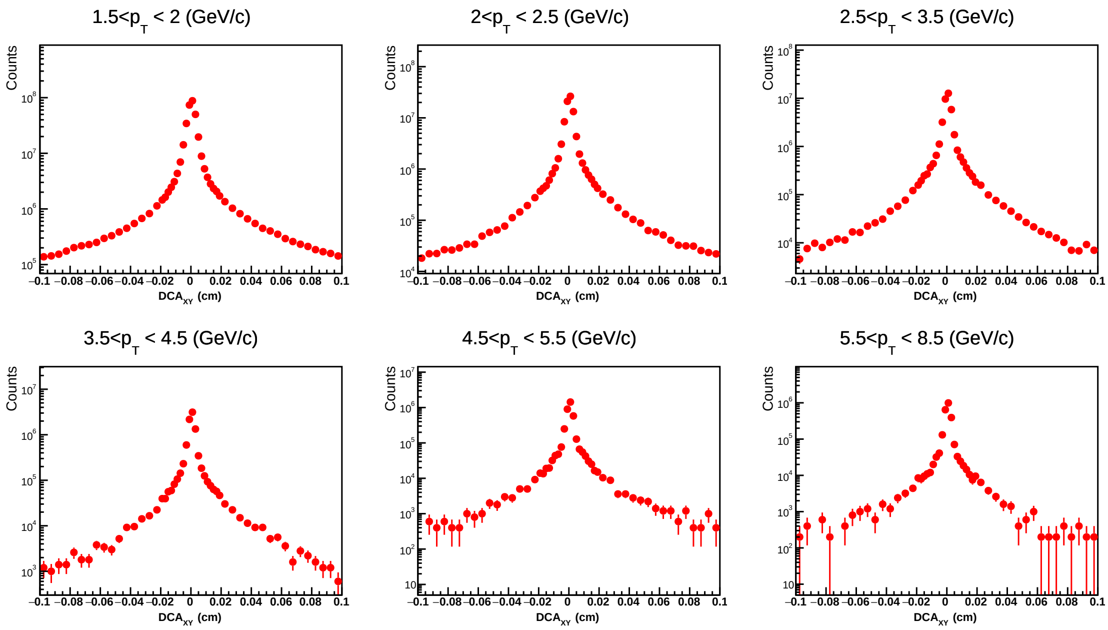

Fig. 4.6: Inclusive electrons candidates DCA_{XY} distribution from data in different p_{T} bins.

4.3 The charm and bottom hadron decayed electrons template from data driven simulation

The non-photonic electron (NPE) are produced by the open heavy flavor hadrons via simi-leptonic decays, which is our signal for the measurement, (e.g. $D \to K e \nu_e$, $B \to D e \nu_e$ and $B \to D e \nu_e \to K e \nu_e$). The DCA_{XY} template for charm and bottom hadron decayed electrons generated by HFT+EvtGen data driven simulation, the details are shown in the following three sections.

4.3.1 EvtGen simulation

The EvtGen has been developed by Barbar experiment and used for over a decades of years with the growing popularity, especially for the B physics. It is a high quality Monte Carlo data generator and heavy flavor decay package which provides a versatile B decay, currently this package has been developed as a stable release that are available to all the particle physics experiments. It is used to simulate the underlying physics processes and as a framework for the implementation of physics processes relevant to decays of B mesons and other resonances. Models of time dependent CP asymmetries in neutral B meson decays, semi-leptonic form factor models. [87]. There are several event generators and decayer available for the simulation of particle decays in high energy physics experiment, why the EvtGen was selected as a simulation package for our NPE analysis, there are a few benefits which are listed in the below items.

- Implementation of spinor algebra to account for spin and to allow the accurate simulation of angular distributions.
- User input mechanism allows the use of complex amplitudes to encapsulate the decay physics.
- Each node of the decay chain is treated independently to allow efficient and fast Monte Carlo generation.
- Code is organized into a modular architecture, with different processes models encoded in separate classes.
- The user may provide his own decay table to over ride the default, decay table informs the code which amplitude should be used to decay a given particle, and gives the branching ratio for each process.
- Quantum interference (mixing,CP violation, resonant, non-resonant final states) which have an important impact on the phenomenology of the decay. This led to the creation of dedicated B-decay packages, the most successful being EvtGen. Neutral B meson oscillations is one of the manifestations of the neutral particle [88], a fundamental prediction of the Standard Model of particle physics. It is the phenomenon of B mesons changing (or oscillating) between their matter and antimatter forms before their decay. The daughter electrons $c\tau$ distribution from B^0 and $\bar{B}^0$ shows on Fig. 4.7, the positron from direct $B^0 \rightarrow D^{\star -} + e^+ + \nu_e$ simi-leptonic decay, electrons from $B^0 \rightarrow \bar{B}^0 \rightarrow D^{\star +} + e^- + \nu_e$, back curve is sum of the B^0 and oscillated $\bar{B}^0$ decay together, which can be described by exponential fit [89].

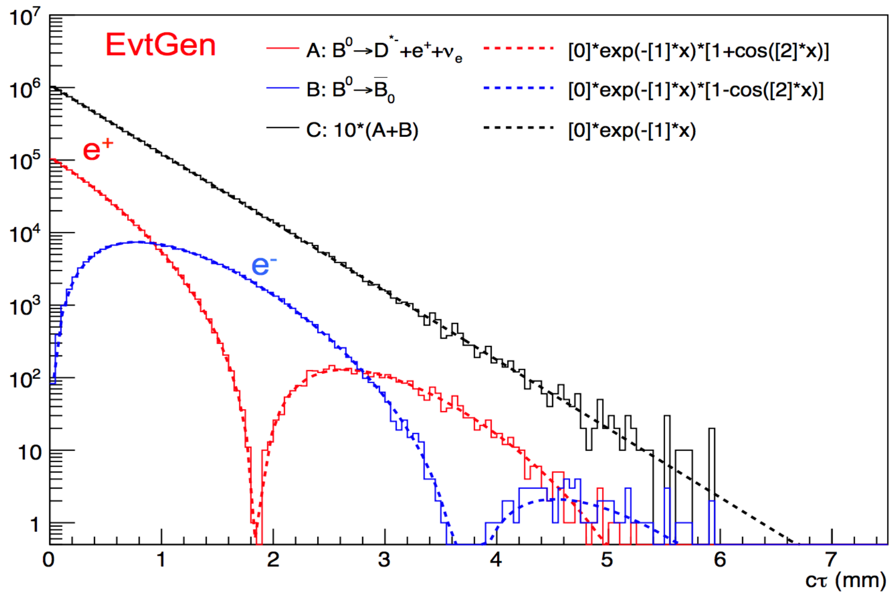

Fig. 4.7: The B^0 and oscillated $\bar{B}^0$ simi-leptonic decayed electrons $c\tau$ distribution, the positron from $B^0 \to D^{\star-} + e^+ + \nu_e$ decay in red curve and electrons from $B^0 \to \bar{B}^0 \to D^{\star+} + e^- + \nu_e$ decay in blue curve, black curve is combined the B^0 and oscillated $\bar{B}^0$ decayed electrons together, the total distribution fitted by an exponential distribution.

4.3.2 Electrons and hadrons DCA$_{XY}$ comparison from full detector Geant simulation

The separation of charm and bottom production analysis based on the STAR Heavy Flavor Tracker Detector (HFT) data sample, this is the first year of physics running with the new detector. However, the STAR official simulation framework embedding with HFT was not available yet. One of the option is the data driven simulation. As we all know, the π are dominant produced during the primary vertex by the strong interactions, the basic idea is that we can apply the tight π identification cut to select a pure π sample, and extracted the DCA$_{XY}$ distribution and HFT ratio from data, and then use the π to smear the electron's true DCA$_{XY}$ which was from simulation. There is a assumption that the π and electron have same HFT resolution, so we have to make the full detector simulation with HFT and justify such a assumption.

Geant is a software toolkit package for the passage of particles through matter simulation. It has been been used by a lot of experiments in a variety of application domains, including high energy physics, astrophysics and space science, medical physics and radiation protection. The Geant4 [90, 91, 92] has been implemented into STAR simulation environment for many years and called "starsim", it has been demonstrated a very accurate knowledge of STAR material budget in STAR GEANT simulations framework. User can define the geometry for different sub-detector, the material budget, since the sub-detector geometry is different in different runs [93]. There are 5 charged π and 5 electrons are injected into "starsim", and in the injected Mc particles are reconstructed with the same chain and detector geometry with data, same track quality cut are applied on simulation with data. The DCA_{XY} comparison between electron and charged π from simulation shows on Fig. 4.8, red and black curve represent the single π and electrons, respectively, while the green and blue curve are from the single Gauss function fit the electrons and charged π DCA_{XY}. The comparison plots shows the electron and π have almost same HFT DCA_{XY} hits resolution in higher p_{T} ($p_{\mathrm{T}} > 1$ GeV/c).

4.3.3 Data driven fast simulation

It has been justified that the electrons and π have almost same DCA_{XY} resolution as shown on Fig. 4.3.2. The LBNL group developed a data driven fast simulation package, and it is used for all the HFT related analysis. This simulation package can do HFT DCA smearing using the charged π and Kaon distributions extracted from data, including the HFT matched efficiency calculated by the number of HFT matched tracks and TPC tracks ratio, spatial resolution: DCA distributions of HFT matched tracks (XY-Z dependence). Luminosity, centrality, azimuth and pseudo-rapidity dependence have been considered. DCA resolution histograms are divided into 5 η, 4 Vz, 9 $centralities$, 2 $particles(K/\pi)$, 21 p_T, and 140 DCA_{XY} x 140 DCA_Z bins 2-D histograms. We input the DCA at 0 to the smear package by detector resolution effect which was obtained from data driven simulation, by comparing the smear results and data again for the validation check, such a comparison was shows on Fig. 4.9, red is from data driven simulation, black is from data in the data driven simulation package. As we can see, the

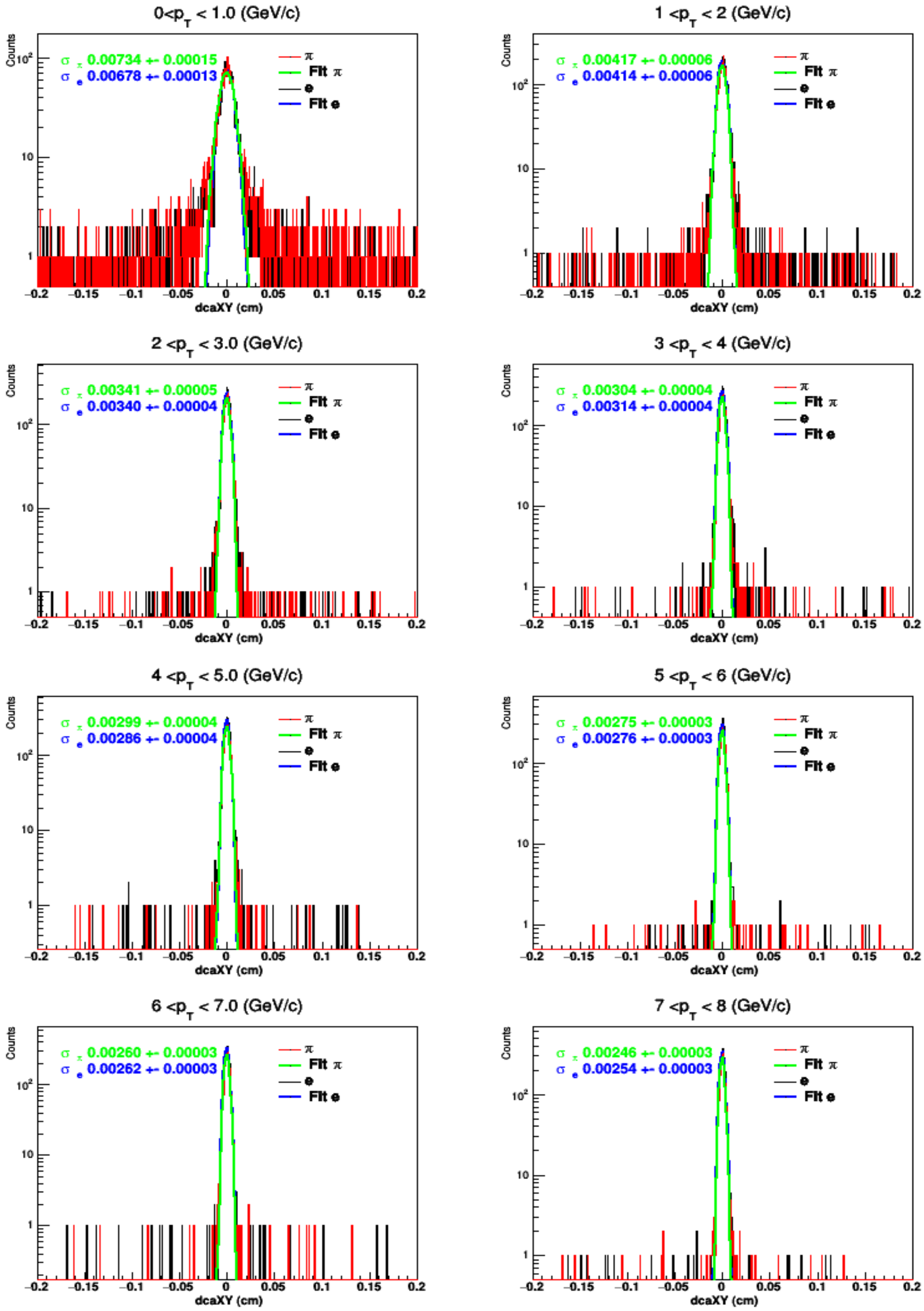

Fig. 4.8: HFT DCA_{XY} hits resolution for electrons and charged π from STAR full detector simulation, red and black curve represent the DCA_{XY} of single charged π and electrons, respectively, the green and blue curve from the single Gauss fit the charged π and electron DCA_{XY}.

data driven simulation are works quit good.

There are a few effects are considered in this data driven simulation.

- Spatial resolution of HFT is encoded in two variables: DCA_{XY} and DCA_Z.
- Vertex resolution, which is possibly folded in the DCA resolution of single tracks and correlated for Kaon and Pions, is a negligible, at least for semi-central to central events.
- The contribution of feed-down particles from secondary decays to DCA distributions is negligible.

The measued NPE are those electrons that dominated by the semi-leptonic decays of open heavy flavor D- and B-mesons. Both charm and bottom hadrons have substantial branching ratios around 10% to single electrons or single muons. The EvtGen has been selected as a heavy flavor decayer to decay the heavy flavor hadrons, since the EvtGen has many benefits to make the heavy flavor study, particular for B physics, the details has been discussed in previous 4.3.1. In this simulation, the D- and B-meson (D^0 , D^+, B^0 and B^+) are inclueded. The input heavy flavor hadron p_{T} spectrum are from the FONLL calculations, and the rapidty distribution from Pythia. The default decay table was used in the simulation, which means all the decay channel (both simi-leptonic and hadronic) are switched on, and the decay branch ratio is kept as default, so only fragmentation-fraction should be take into account during the total charm and and bottom decay electrons normalization and combination. The fragmentation fraction for different charm mesons are from the measurements [94]. The average of charm decayed electron is combined from the electrons from D^0 , D^+ based on its fragmentation fraction which is shown in Fig. 4.10. Both the individual bottom meson and the average are shown in Fig. 4.11, different panel represents different p_{T} bin.

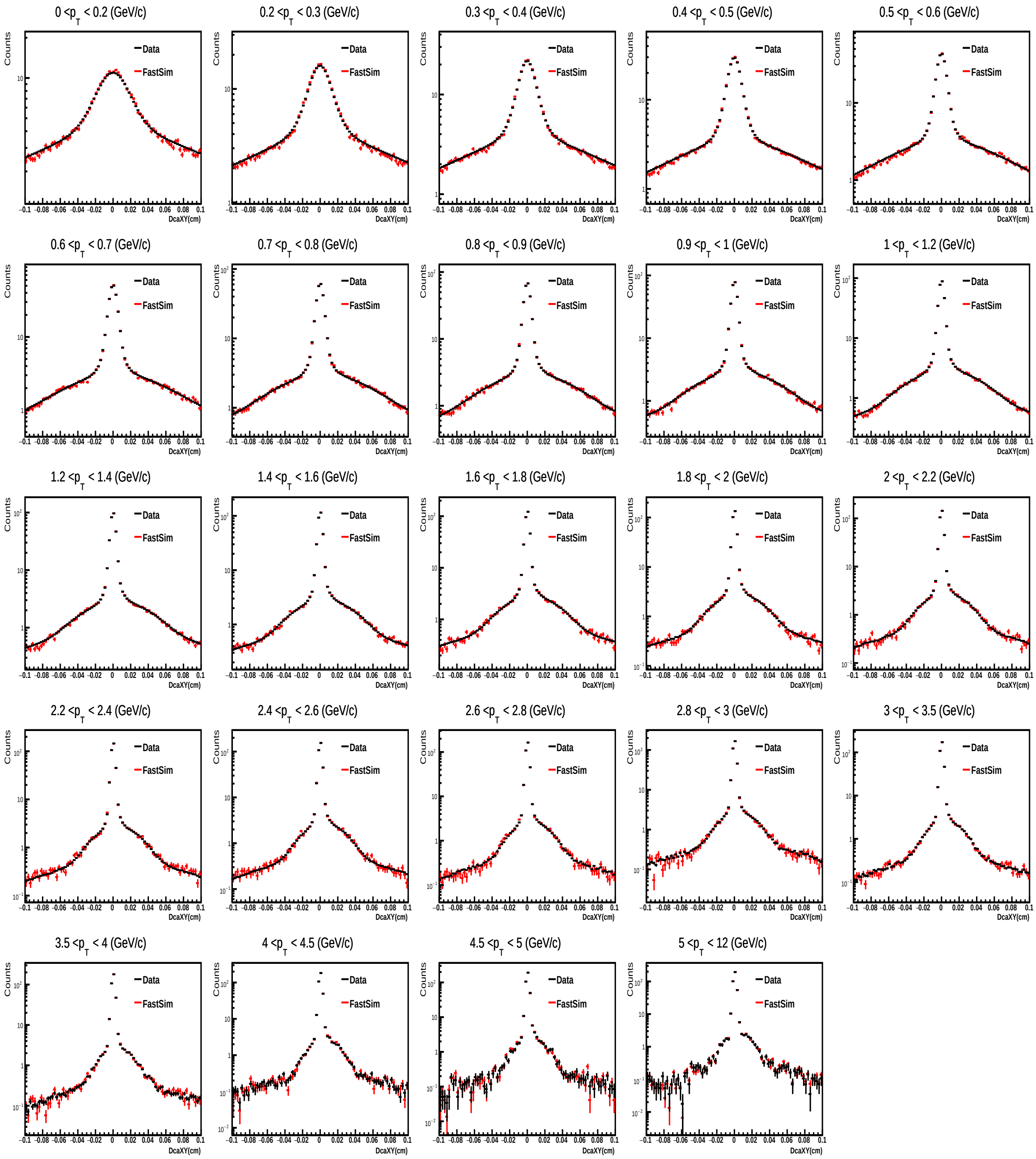

Fig. 4.9: Data driven simulation validation check, red is from data driven simulation, black is from data in the data driven simulation package, different panels shows different p_{T} bins.

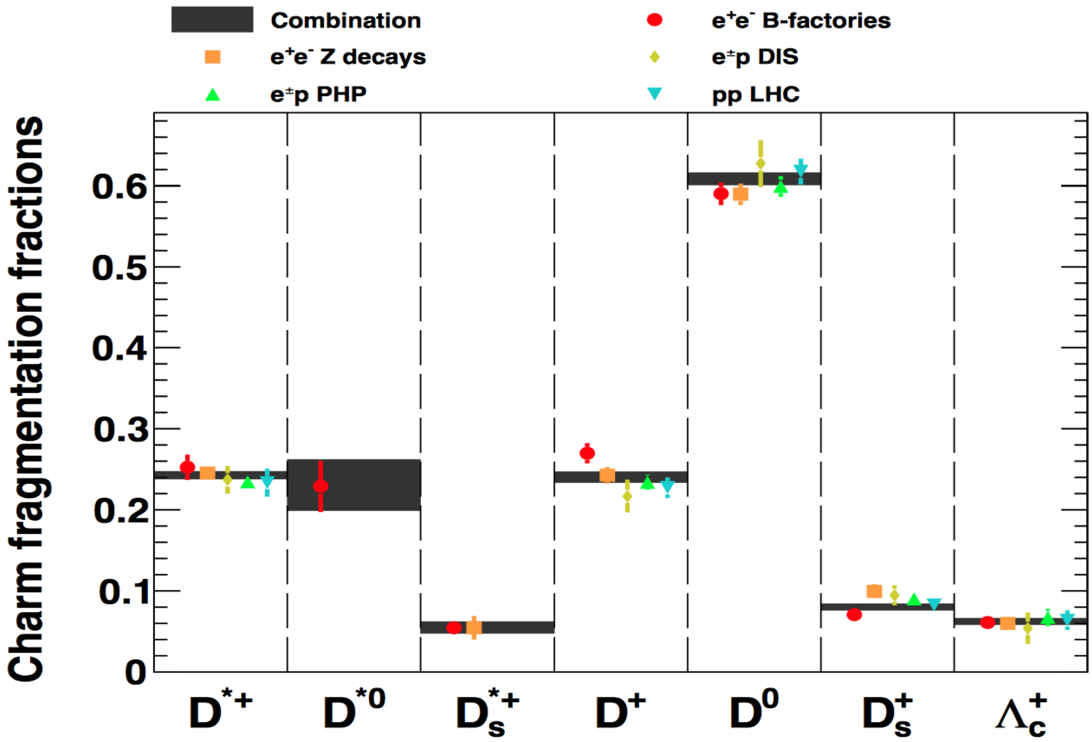

Fig. 4.10: The values of charm-quark fragmentation fractions from the measurement. Averages of included data in different production regimes are shown with various full symbols.

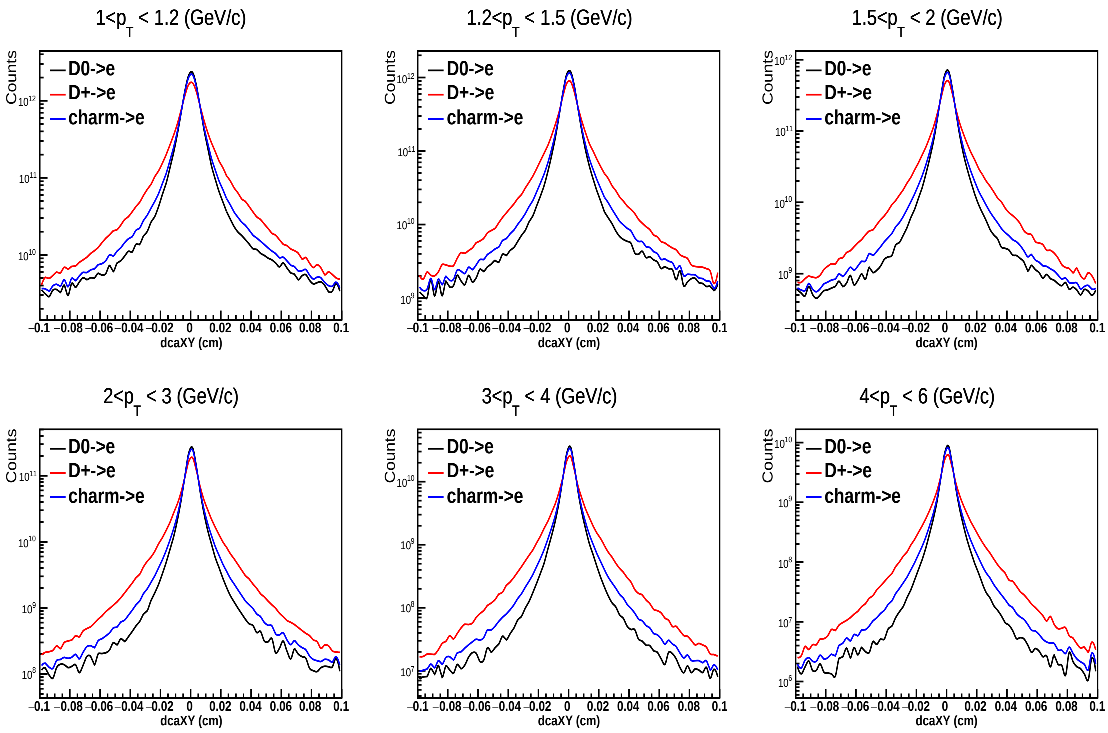

Fig. 4.11: Charm meson simi-leptonic decayed electrons DCA$_{XY}$ from data driven fast simulation, the D^0 ($\bar{D}^0$) and $D^{\pm}$ decayed electrons DCA$_{XY}$ are indicated by black and blue curve, respectively, blue curve represent the combination of D^0 ($\bar{D}^0$) and $D^{\pm}$ and decayed electrons.

The produced b or *barb* quarks can hadronized with different probabilities into the full spectrum of b-hadrons, either in their ground or excited states, The sum of the b fragmentation fraction were obtained from a fit where the sum of the fractions were constrained to equal 1.0, neglecting production of Bc mesons. The observed yields of Bc mesons at the Tevatron [95] yields fc = 0.2%, in agreement with expectations [96], and well below the current experimental uncertainties in the other fractions [97]. The fragmentation fraction for bottom meson are obtained from PDG ??, The average of bottom decayed electron is combined the electrons from B^0 , B^+, Both the individual bottom meson and the average are shown on Fig. 4.12, different panel represents different p_{T} bin.

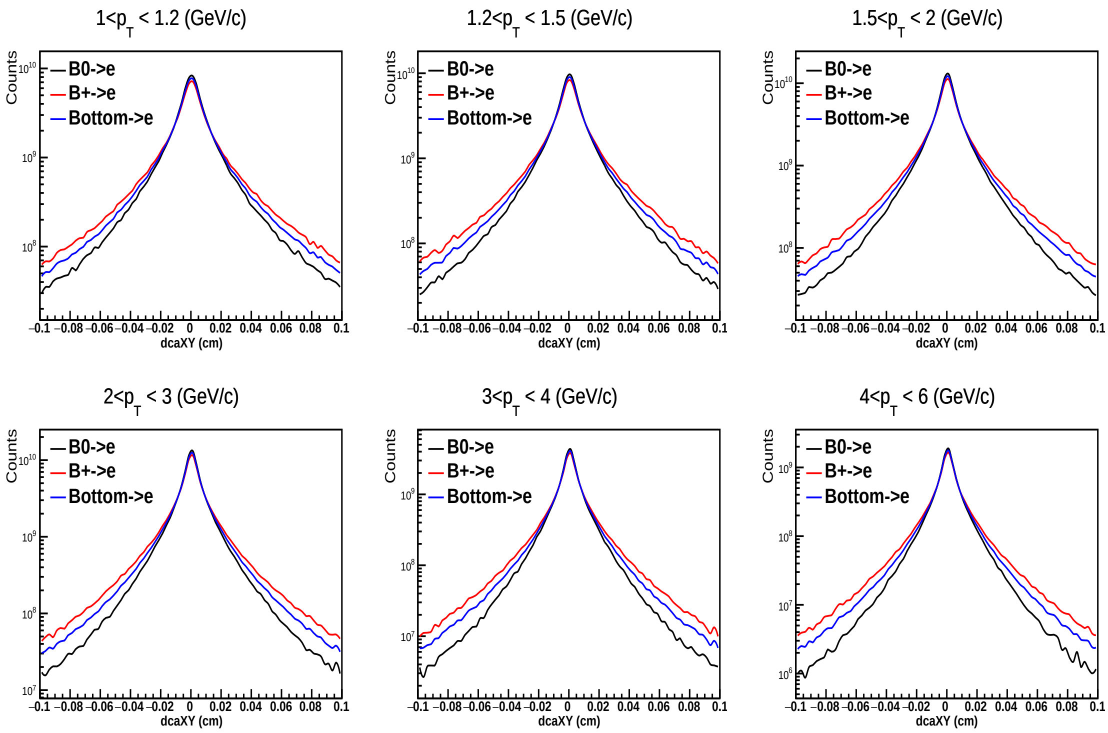

Fig. 4.12: Bottom meson simi-leptonic decayed electrons DCA$_{XY}$ from data driven fast simulation, the B^0 $\bar{B}^0$ and $B^{\pm}$ decayed electrons DCA$_{XY}$ are indicated by black and blue curve, respectively, blue curve represent the combination of B^0 $\bar{B}^0$ and $B^{\pm}$ and decayed electrons.

The current total fragmentation fraction for both charm and bottom mesons are greater than 80%, but still some other remain D- and B-meson D_s and B_s etc. contributions are not excluded in the simulation so for. Since it can be covered by the systematic uncertainty.

4.4 Background DCA template

The main background is photonic electrons from gamma conversions , π^0, η mesons Dalitz decays electrons and the mis-identified hadrons for this measurement. Additional electron sources, such as heavy quarkonia decays ($J/\Psi \to e^- + e^+, \Upsilon \to e^- + e^+$), Drell-Yan processes ($q + \bar{q} \to e^- + e^+$), K_{e3} decays ($K \to \pi e \nu_e$), and light meson decays, also contribute to the inclusive electron sample, but the dominate background are still the photonic electrons including gamma conversions in the detector materials and π^0 and η mesons Dalitz decays electrons and the mis-identified hadrons.

4.4.1 Photonic electrons background

The photonic electrons from gamma conversions Eq. 4.1 in the detector materials and $\pi 0$ and η mesons Dalitz decays Eq. 4.2 and Eq.4.3. The photonic electron was reconstructed by the photonic pairs via e^+e^- invariant mass and pair DCA method. The tighter electron identification cut applied on one of the electron and called primary electrons, then randomly pairing up electrons with the same charge (marked as like-sign) and opposite charge (marked as unlike sign), the uncorrelated combination background subtracted by unlike sign minus like sign method. We applied the mass $m_{e^+e^-} < 0.06$ GeV) and the measured distance-of-closest-approach between two daughters (Pair DCA $e^+e^- < 0.6$ cm) for the pair cut. For the associated partner electrons, the looser electron identification cuts are applied, like TPC energy lose dE/dx $-3.5 < n\sigma_e < 3.5$ cut and the track quality cuts which are discussed in the previous table 4.2.1, the looser cuts expect a higher photonic electron reconstruction efficiency. The details for the photonic electron reconstruction cut are listed in table 4.2.

Fig. 4.14 shows the photonic electron parents source (Gamma,π^0 and η) yield density as a of function p_{T} from simulation, the π^0 , η and direct photos from the PHENIX measurements used a function fit to extend to higher p_{T} [48, 98], Gamma from $\pi^0 \to 2\gamma$, $\eta \to 2\gamma$ and direct photos contribution.

$$\gamma = e^+ + e^- \tag{4.1}$$

$$\pi^0 = e^+ + e^- + \gamma \qquad (1.174 \pm 0.035)\% \tag{4.2}$$

$$\eta = e^+ + e^- + \gamma \qquad (0.69 \pm 0.04)\% \tag{4.3}$$

After applying all the track quality cuts and electron identification cuts, the raw DCA_{XY} distribution for the photonic electrons from data are shown on Fig. 4.13, different panels represent for different p_{T} bins. As you can see, the statistics is really very poor in high

p_T ($p_T > 4.5$ GeV). Therefore, the Hijing simulation was used to extend the p_T to higher range, the details about the Hijing simulation discussed on 4.4.2.

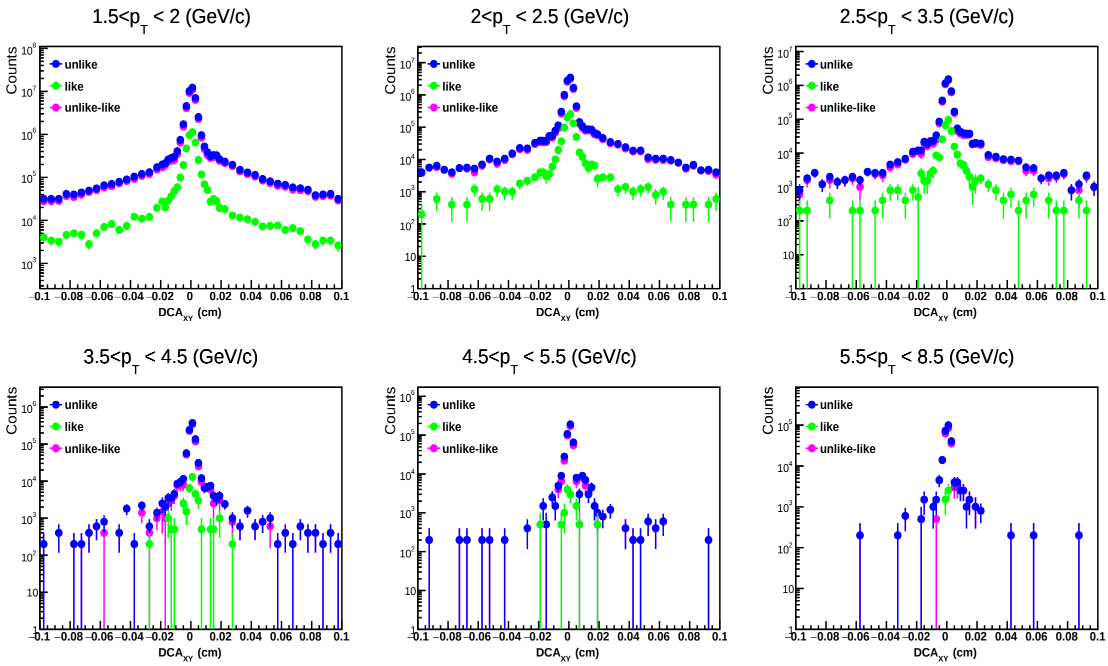

Fig. 4.13: Photonic electrons unlike-sign (blue points),like-sign (green points), unlike-like-sign (magenta) from data in different p_T bins.

It has been mentioned that the photonic electrons was dominated by three different electron source. The gamma conversion and Dalitz decay electron DCA_{XY} shape are different, since the Dalitz decay with a very short life time ($c\tau = 200\nu m$), which is happened almost at primary vertex, while the gamma conversion are taken place in the detector materials with a large conversion radius. Unfortunately, different photonic electron source can not be divided by the detectors in data, however the individual DCA_{XY} shape can be carried out by simulation, and then combined the individual photonic electron source based on it's relative contribution, which was extracted by its parent production invariant yield shown on Fig. 4.14, the figure shows the photonic electron parents Gamma, π^0 and η p_T spectrum as a function of p_T , the π^0 , η and direct photos are from the PHENIX measurements in the low p_T and using a function fit the low p_T data point to extend to higher p_T [48, 98], Gamma from $\pi^0 \to 2\gamma$, $\eta \to 2\gamma$ and direct photos contribution are from simulation.

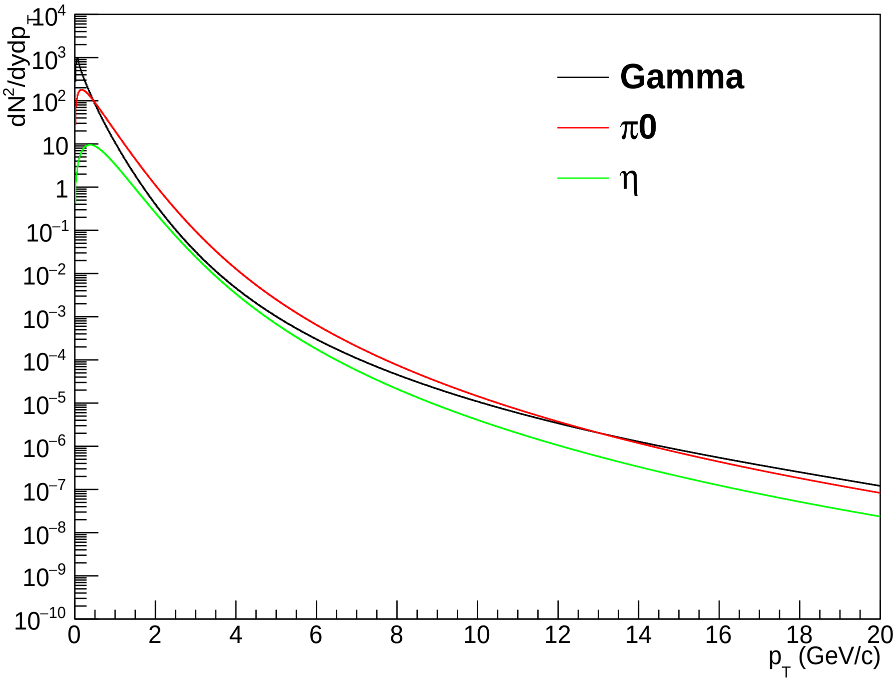

Fig. 4.14: The gamma,π^0 and η yield desity as a function p_{T} from simulation, the π^0 , η and direct photos from the PHENIX measurements used a function fit to extend to higher p_{T} .

4.4.2 Hijing simulation

Hijing is a Monte Carlo event generator for parton and particle production in high energy hadronic and nuclear collisions. Based on QCD-inspired models for multiple jet production, it is designed in particular to study jet and mini-jet production and associated particle production in high energy p+p, p+A and A+A collisions. This model incorporates mechanisms such as multiple mini jet production, soft excitation, nuclear shadowing of parton distribution functions and jet interactions in dense hadronic matter. It has been compared extensively to p+p data at collider energy, and with existing heavy ion data at SPS energies [99, 100, 101].

We input additional 500 photons,100 neutral pions and 100 eta mesons injected per Hijing event with flat p_{T} , the Hijing event was reconstructed by the Geant with STAR full detector geometry, the reconstruction chain are same with data production, and same STAR software library SL16d. in order to reproduce the data, there are a few more effect effect was take into account in the Hijing simulation setup which is listed in the below lines. most of the this effects are extracted from data.

- Day depentent pileup effect from data.
- Tuned the PXL DCA resolution based on the pure π sample which was extracted from data.
- Realistic masking table from data.
- Pixelization effect.

The photonic electrons from Hijing simulation was combined from gamma conversion and Dalitz decay electrons. The combination weight factor for different electron source based on the its relative contribution to the total photonic electrons, the different electron source plotted as a function of p_{T} shows on Fig. 4.15.

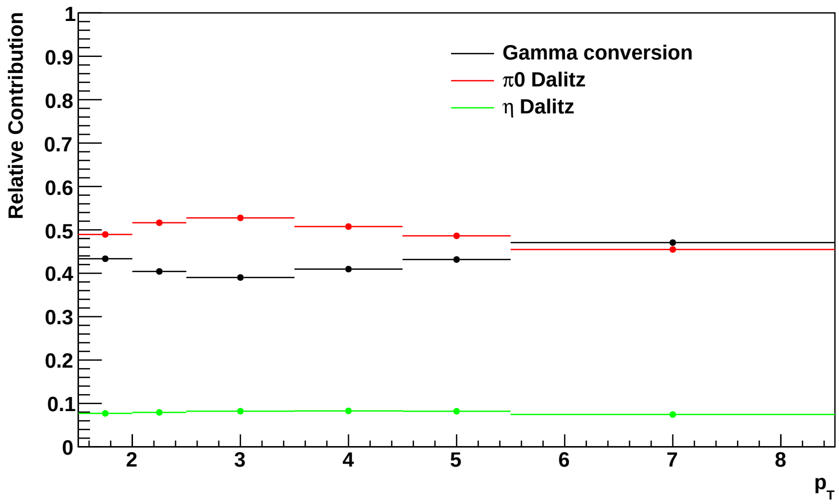

Fig. 4.15: Different photonic electron relative contribution as a function of p_{T} .

After taken into the relative contribution to the total photonic electrons, three individual photonic elctron are combined based on the Eq. 4.4. The average total photonic electrons from Hijing simulation shows on Fig. 4.16, different panel shows the photonic electron DCA$_{XY}$ distribution for different p_{T} intervals. The Hijing simulation improved the statistics significantly at higher p_{T} . The DCA$_{XY}$ flipped Hijing simulation can describe the data better than without the flip, hence, the fliped Hijing DCA$_{XY}$ was used as the photonic electron template.

$$
\begin{aligned}
Phe_{Total}(DCA_{XY}) = & \frac{N_e^{\pi^0}(DCA_{XY})}{N_e^{\pi^0}(DCA_{XY}) + N_e^{\eta}(DCA_{XY}) + N_e^{\gamma}(DCA_{XY})} Phe_{\pi^0}(DCA_{XY}) + \\
& \frac{N_e^{\eta}(DCA_{XY})}{N_e^{\pi^0}(DCA_{XY}) + N_e^{\eta}(DCA_{XY}) + N_e^{\gamma}(DCA_{XY})} Phe_{\eta}(DCA_{XY}) + \\
& \frac{N_e^{\gamma}(DCA_{XY})}{N_e^{\pi^0}(DCA_{XY}) + N_e^{\eta}(DCA_{XY}) + N_e^{\gamma}(DCA_{XY})} Phe_{\gamma}(DCA_{XY})
\end{aligned}
\tag{4.4}
$$

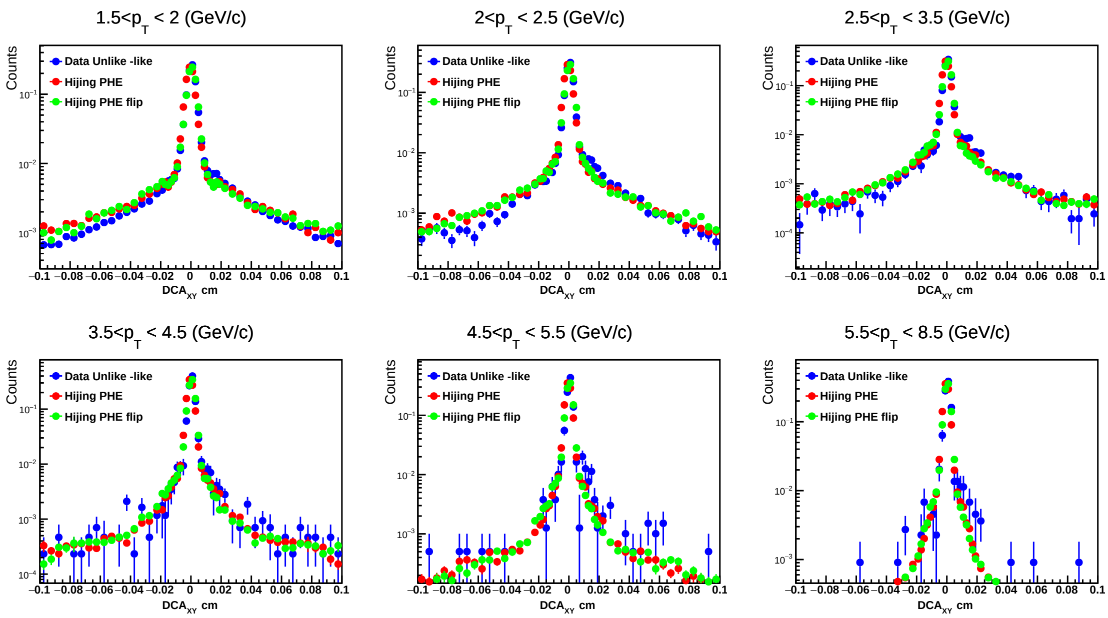

Fig. 4.16: Comparison DCA$_{XY}$ between data (unlike-like sign in blue points) and Hijing (combined gamma conversion and Dalitz decay electron in red point) simbulation,fliped DCA$_{XY}$ between negative side and positive slide in Hijing (combined gamma conversion and Dalitz decay green points)

This analysis focused on the B hadron decayed electron fraction to inclusive heavy flavor decay electron, instead of the absolute yield production. Therefore the DCA dependent efficiency should be take into account, only for the DCA shape correction. Fig. 4.17 shows the ratio of the inclusive photonic electron and inclusive photonic electron that associate with a partner, it is clearly that this ratio is DCA dependent, thus a DCA bin by bin correction was take applied to the final photonic electron template.

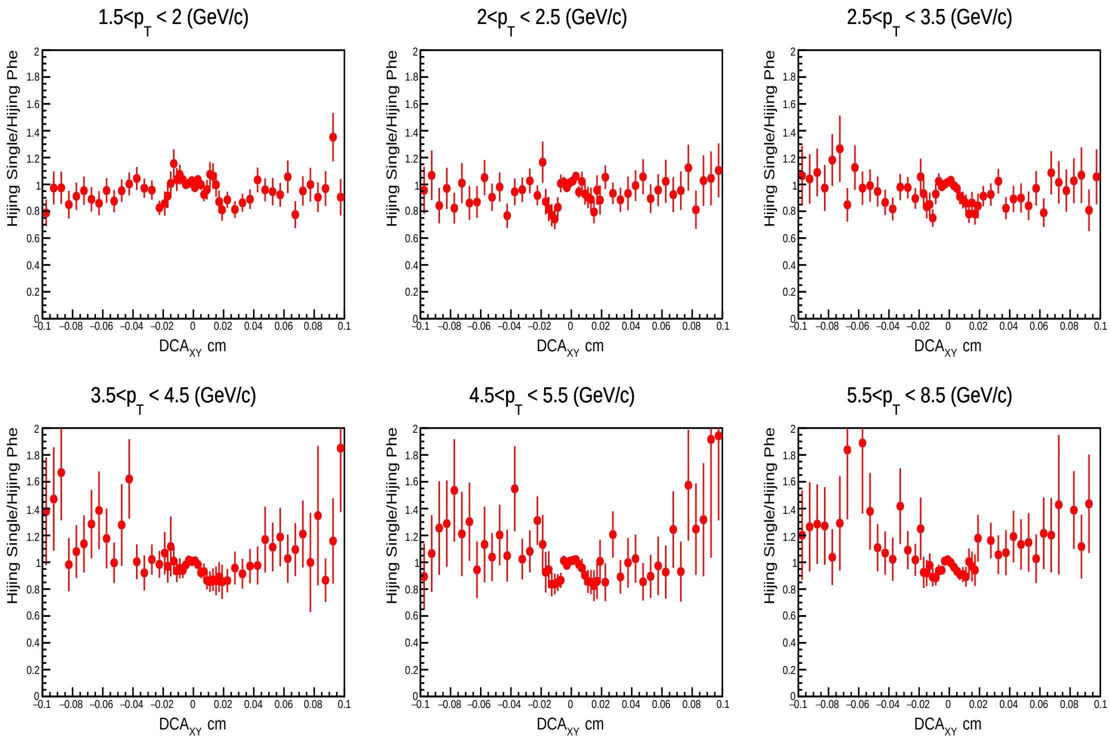

Fig. 4.17: The ratio of the single photonic electron and single photonic electron that associate with a partner, different panel shows different $p_{\rm T}$.

In this analysis, the low $p_{\rm T}$ statistics is sufficient, so the photonic electron template from data, but higher $p_{\rm T}$, the photonic electron template from data Hijing simulation. Both the low $p_{\rm T}$ and high $p_{\rm T}$ are corrected by the DCA dependent photonic electron reconstruction efficiency which are from the Eq. 4.5 and 4.6 ,respectively.

$$Phe_{DCA_{XY}}(4.5GeV <= p_{\rm T}) = \frac{Phe^{Data}_{DCA_{XY}}}{Phe^{Hijing}_{DCA_{XY}}} Single^{Hijing}_{DCA_{XY}} \tag{4.5}$$

$$Phe_{DCA_{XY}}(p_{\rm T} < 4.5GeV) = \frac{Single^{Hijng}_{DCA_{XY}}}{Phe^{Hijing}_{DCA_{XY}}} Phe^{Data}_{DCA_{XY}} \tag{4.6}$$

4.4.3 Hadron background DCA$_{XY}$ from data

The mis-identified hadrons DCA$_{XY}$ template extracted from data, we applied the track quality cuts but without any particles identification cuts, so the inclusive hadron sample includes the π, kaon and proton. The DCA$_{XY}$ distribution from the inclusive hadron in different p_{T} bins are shown in Fig. 4.18. different panel represent different p_{T} bins. The mis-identified hadrons background are taken into account as an independent component in the final B fraction fit.

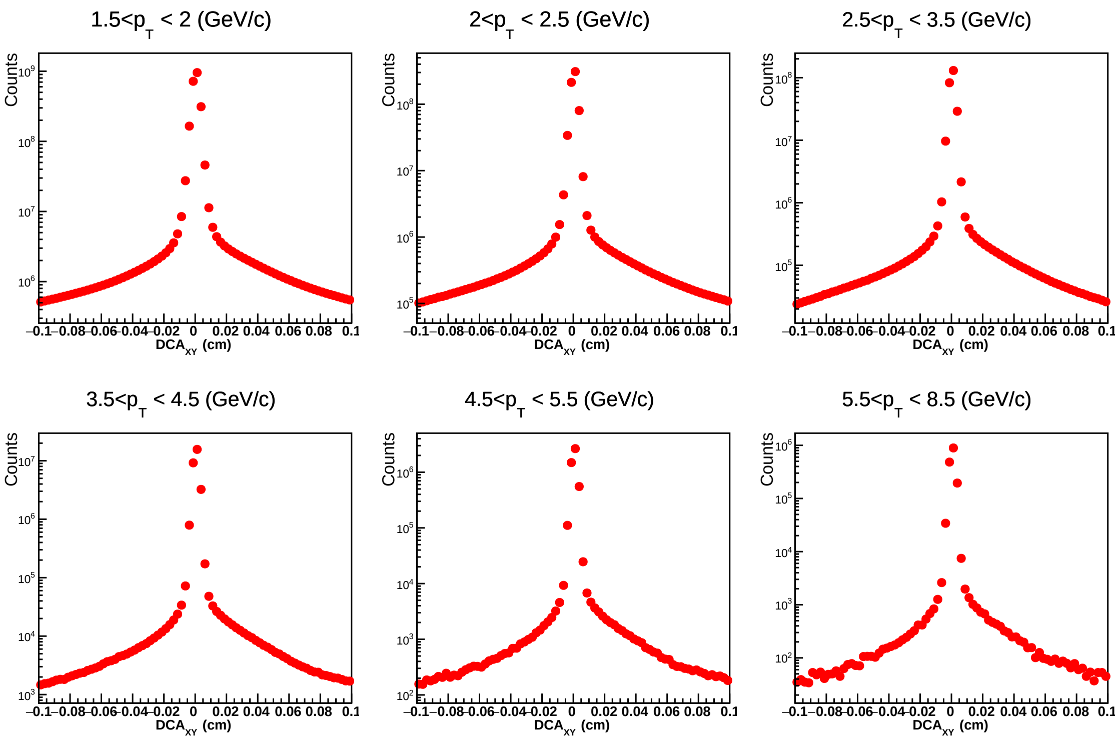

Fig. 4.18: The inclusive hadrons DCA$_{XY}$ distribution from data, different panel are for different p_{T} bins.

4.4.4 hadron fraction estimation from electron purity fit

The mis-identified hadron as electrons background, its fraction can be calculated based on the inclusive electron purity. The purity is the hadrons fraction in the inclusive electron candidates, the inclusive electron purity was estimated from data by the Multi-Gaussian fits to the inclusive electrons nσ_e distributions.

In order to constrain the $n\sigma_e$ Multi-Gaussian fits, the position and width for electrons are calibrated by the $n\sigma_e$ from the photonic electrons. Fig. 4.19 shows the nσ_e distribution, which is fitted by a single Gaussian function without any constrain.

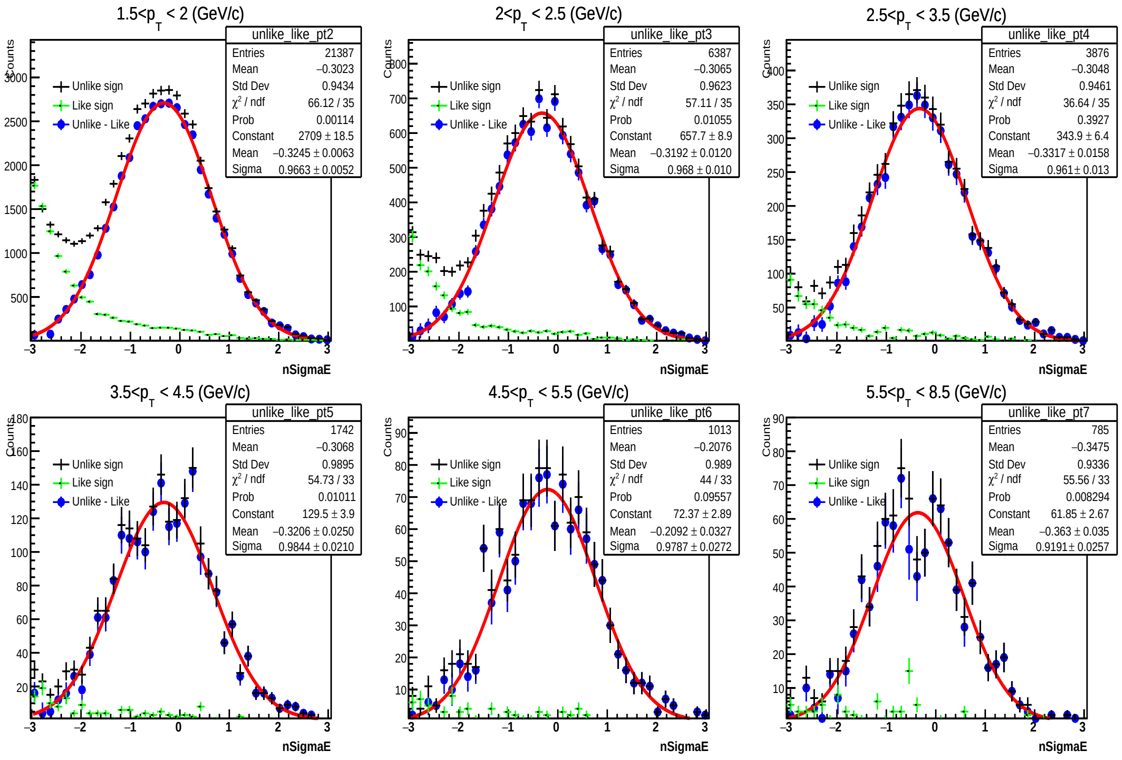

Fig. 4.19: Photonic electron nσ_e distribution in different p_{T} bins.

The electron and sigma obtained from the fitted function. Fig. 4.20 shows the distributions of mean and sigma of the Gaussian function as a function of p_{T} , a constant used to fitted the μ and σ. The uncertainty for the mean covered by shifting the mean constant up and down by 0.04, the uncertainty of the sigma covered by shifting the fitted function up and down 0.02.

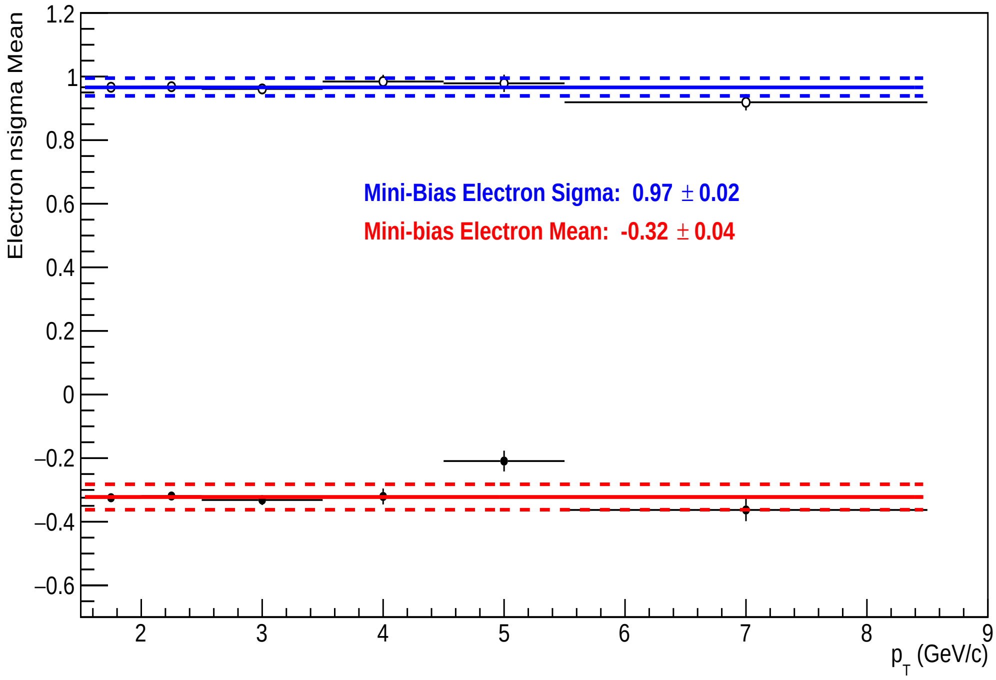

Fig. 4.20: Distributions of the mean and sigma from the Gaussian fit to nσ_e distributions as a function of p_{T} .

Purity of inclusive electron was estimated from constrained multi-Gaussian fit to the $n\sigma_e$ electron distributions. Every single Gaussians function in the fit represent different particle species and they are summed together to the final multi-Gaussian fit. we use a single Gaussians to describe the proton and kaon, since proton and kaon nσ_e mean and sigma are closer to each other. Figure. 4.21 shows the inclusive electron candidates $n\sigma_e$ fitted by a 4-Gaussian function. Here, all the cuts has been applied except the $n\sigma_e$, there is no constrain on the hadron component, but the electrons mean and width were constrained, the constrained limits estimated from the photonic electron $n\sigma_e$ calibration. One sigma deviation was constrained for both the mean and sigma. The purity of the inclusive electrons is calculated based on the Eq. 4.7. it is the ratio of the integral of the electron fit function (red curve) to that of the overall fit function (blue curve) between the range of (-1,3).

$$purity = \frac{\int_{-1}^{3} f(electrons, p_{\mathrm{T}})}{\int_{-1}^{3} f(overall, p_{\mathrm{T}})} \tag{4.7}$$

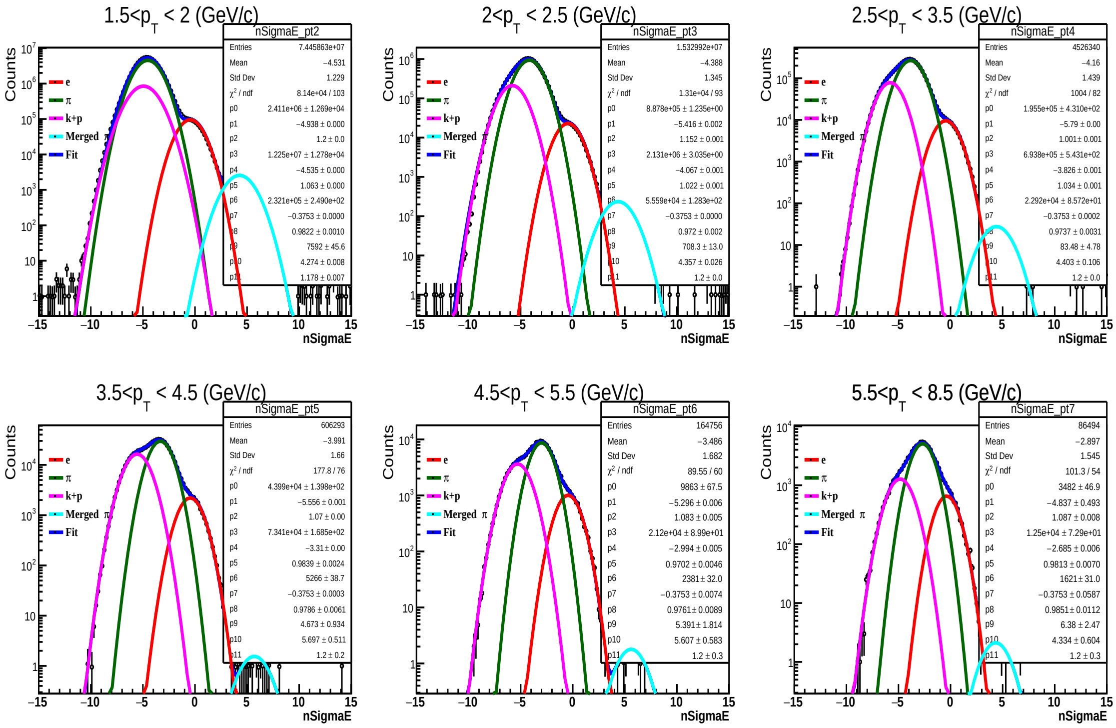

Fig. 4.21: The $n\sigma_e$ distribution for inclusive electrons (black points)and fits from different components by a multi-Gaussian function for different p_{T} . Every single Gaussian function in the fit represent different particle species and they are summed together to the final multi-Gaussian fit.

The systematic uncertainty of the purity estimated by the different constrain on the multi-Gaussian fit, both the mean and width of the electron varied from one, two and three standard deviations from their central values. The final purity is from the average of different constrain and the systematic uncertainty is taken from the maximum deviation from the mean of the three sets of constraints, Fig. 4.22 left panel shows the inclusive electron purity as a function of p_{T} from different constrain. right panel show the final inclusive electron purity as a fucntion of p_{T} , the uncertainty was from left panel maximum deviation.

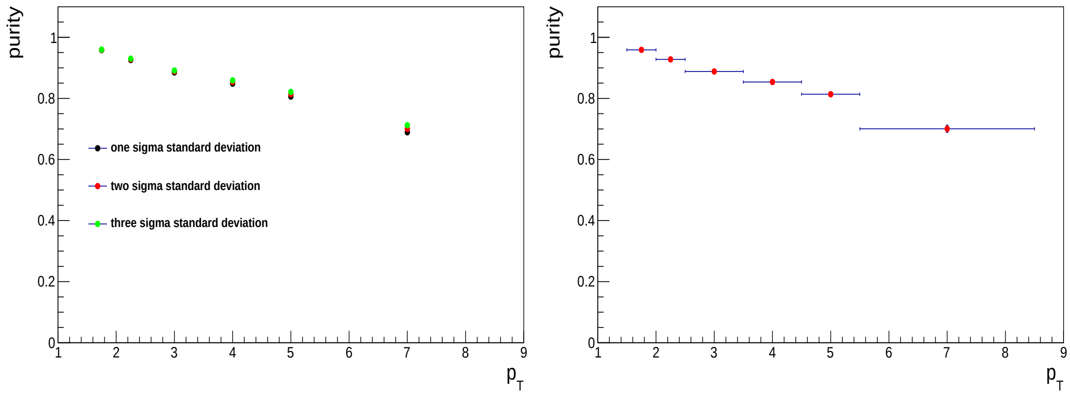

Fig. 4.22: The left panel shows the the inclusive electron purity as a function of p_{T} for different constrain, right panel shows the the final purity with the systematic uncertainty.

4.5 Fraction fit to the data inclusive electrons based on the template

4.5.1 Basic concepts of Minut

The Minut is one of important package which acts on a multi-parameter which was developed by Fortran. however, it has been implemented into the ROOT with a C++ interface, User can define the chi-square function FCN is defined via the MINUIT SetFCN member function. It is the task of MINUIT to find those values of the parameters which give the lowest value of chis-quare. The statistical interpretation about how the MINUIT determining the statistical significance and error propagation.[102]

The basic idea of the template fraction fit is to sum all the template components together as a single components, every individual component with a coefficient as the weight factors Eq. 4.8, in this equation, there are four components, then try to fit the single components to the inclusive electrons. The sum of fraction parameter should be equal to 1, and every individual component fraction between 0 and 1. In the fit equation 4.8, there are four components, but only three of them are as free fractions, For the charm and bottom decay electrons component fraction, the constrain to the fraction parameter is between 0 and 1, The constrain for the hadron background template based on the inclusive electron purity which was extract from data, so the photonic electron fraction was decided by the other three (1-$f_B - f_D - f_{PHE} - f_{Hadron}$). The global constant for the normalization of the yield, since we normonized each template to 1 before the template fit. Fig. 4.23 shows the template fit to the inclusive data which is from data, in the top panel, the black points is DCA$_{XY}$ distribution for inclusive electrons from data, red curve is fraction fit to the data inclusive electrons based on the template in different p_{T} bins, blue dash curve is the electrons from charm decays, margeta dash curve is electrons from bottom decays. light blue is the sum of gamma conversion and Dalitz decay electron background, green curve is the mis-identified hadron as electrons background, lower panel shows the ratio between fit function and data.

$$\begin{aligned} Inclusesive \quad electron = Norm(&f_B e^B + f_D e^D + f_{Hadron} e^{Hadron} \\ &+(1 - f_B - f_D - f_{PHE} - f_{Hadron}) e^{PHE}) \end{aligned} \tag{4.8}$$

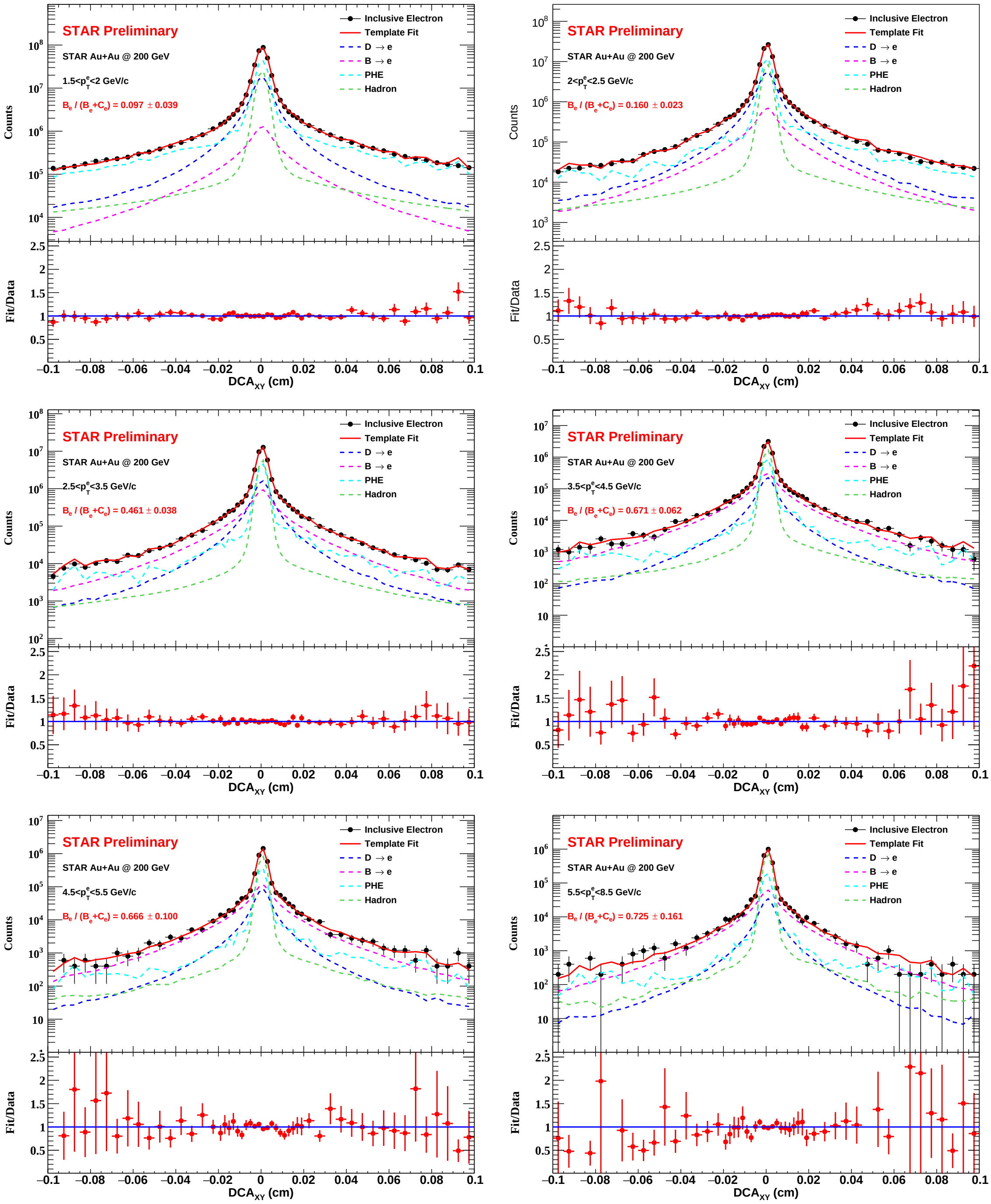

Fig. 4.23: Top panel:The black points is DCA$_{XY}$ distribution for inclusive electrons from data, red curve is fraction fit to the data inclusive electrons based on the template in different $p_{\rm T}$ bins, blue dash curve is the electrons from charm decays, margeta dash curve is electrons from bottom decays. light blue is the sum of gamma conversion and Dalitz decay electron background, green curve is the mis-identified hadron as electrons background. Lower panel: The ratio between Fit function and data.

The B hadron decay electron to inclusive heavy flavor decay electron fraction can be calculated based on the formulation $\frac{N_{eB}}{(N_{eD}+N_{eB})}$, the N_{eB} and N_{eD} extract from the Eq. 4.9 and 4.10, respectively.

$$N_{eB} = Norm * f_B \tag{4.9}$$

$$N_{eD} = Norm * f_D \tag{4.10}$$

where the $Norm$, f_D and f_D are obtained from the template fit.

4.5.2 Systematic uncertainty

The systematic uncertainty calculated for each p_{T} bin in this analysis. The main systematic uncertainty source are discussed in the below lines.

- A: The systematic uncertainty from the fit range, since the difference between charm and bottom decay electrons are different in different DCA$_{XY}$ range, so the fit range will effect the final result B-fraction. (change the fit range from 0.1 cm to 0.06 cm).
- B: The systematic uncertainty from different hadron source (change the hadron template from π candidates to inclusive hadron, take the difference as the systematic of hadron template)
- C: The systematic uncertainty from charm hadron decay electron DCA$_{XY}$ template shape (change the charm quark fragmentation ratio to D^0 and D^+ based on it's uncertainty from measurements, since we combined D^0 and D^+ decayed electron as a single component in the final template fit from data driven fast simulation, the detail have been discussed in the previous).
- D: The systematic uncertainty from decayed charm re-weight spectra in the data

driven fast simulation, the default is FONLL calculation, the charm hadron p_{T} spectrum changed from FONLL to measurements.

- E: The systematic uncertainty from with and without hadron fraction fit, the fraction of mis-identified as electrons fraction can be estimated based on the nσ_e distribution from data. take the difference between with and without hadron constrain as the hadron fraction constrain uncertaity. the average of with and without hadron constrain as the final default value.

- F: The systematic uncertainty from Hijing simulation, since the photonic electron statistics from data is too hungry in the higher p_{T} ($3.5GeV/c < p_T$), so the Hijing+Geant simulation taken as a approach to extrapolate the DCA$_{XY}$ to from low p_{T} to higher p_P ($< 3.5GeV p_T$), the lower p_{T} ($< 3.5GeV p_T$) photonic electron template is from data since we have sufficient statistics from data, so we take the Hijing+Geant simulation corrected by data, taken the difference between $2 < p_T < 2.5GeV$ and $2.5 < p_T < 3.5GeV$ Fig. 4.16 as the p_{T} extrapolation systematic uncertainties.

Table 4.4: The summary of the main p_{T} bin-by-bin systematic errors

p_{T} (GeV/c)	Fit range	Hadron template	Charm template	Charm spectrum	Hadron fraction	Hijing phe.	All sys
$1.5 < p_T < 2$	0.0622	-0.0200	0.0585	0.5678	-0.0007	0.0000	0.5779
$2 < p_T < 2.5$	-0.0212	-0.0685	0.0245	0.2286	-0.0001	0.0000	0.2782
$2.5 < p_T < 3.5$	0.0012	-0.0675	0.0067	0.0492	-0.0000	0.0000	0.1113
$3.5 < p_T < 4.5$	0.0527	-0.0338	0.0028	0.0070	0.0703	-0.0147	0.1009
$4.5 < p_T < 5.5$	0.0357	-0.0135	0.0031	0.0086	0.0769	-0.0406	0.0994
$5.5 < p_T < 8.5$	0.0403	0.0050	0.0031	0.0048	0.1327	-0.0486	0.1462

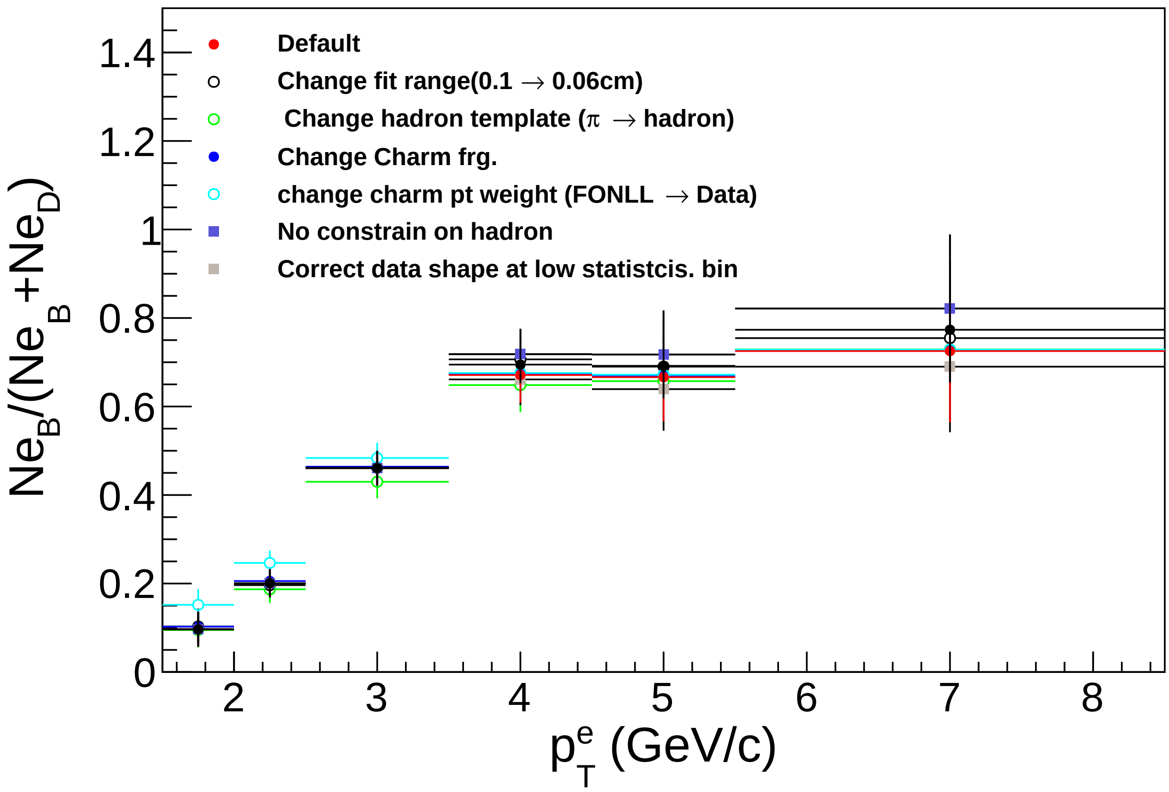

Fig. 4.24: The main systematic uncertainties in the fraction of B-decayed electrons is extracted from DCA$_{XY}$ distribution in data to templates.

4.5.3 The fraction of B-decayed electrons.

The fraction of B-decayed electrons ($\frac{B\to e}{D\to e+B\to e}$) is extracted via fitting track impact parameter DCA$_{XY}$ distribution method at in Au+Au collisions $\sqrt{s_{NN}}$ = 200 GeV. The fit result of the open heavy flavor decay electrons from bottom hadrons fraction is obtained via the fraction fit which is shown in Fig. 4.23, This measurement was carried out at mid-rapidity ($|y|$ <0.7), the B-decayed electrons fraction $r_B = \frac{N_{eB}}{(N_{eB}+B_{eD})}$ is shown as a function of p_{T} in Fig. 4.25, the red points represent the B-decayed electrons fraction central value, and the vertical lines represent the statistics error which was extracted from Tminut fit package, the vertical error band indicate the statistics uncertainty. The grey band was from PHNEIX measurements [103]. As we can see from the figure, the fraction of B-decayed electrons increased at lower p_{T} region ($p_T < 4GeV$), it is flat at higher p_T . This analysis is consistent within uncertainty with PHNEIX VTX result. The fraction of B-decayed electrons $r_B = \frac{N_{eB}}{(N_{eB}+B_{eD})}$ is measured in p+p collisions at $\sqrt{s}$ = 200 GeV by STAR [45], This measurements are obtained through electron-hadron azimuthal correlations. The vertical line represent for the statistics, while the vertical band represent the systematic uncertainty. r_B increases with electron p_T . The FONLL pQCD calculation including theoretical uncertainties in black dash lines. The fraction of B-decayed electrons in p+p are consistent with FONLL calculations [33].

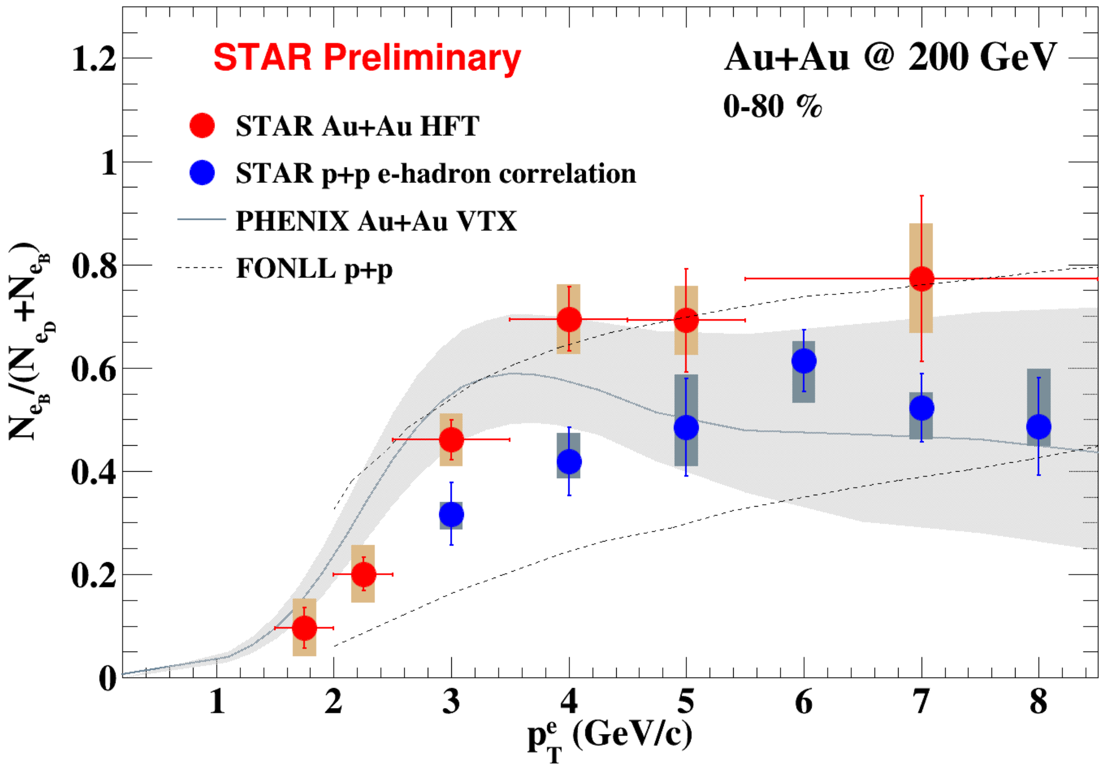

Fig. 4.25: The fraction of B-decayed electrons is extracted from fitting track impact parameter distribution in data to templates Au+Au at $\sqrt{s_{NN}}$ = 200 GeV collisions, the fraction of B-decayed electrons in p+p collisions at $\sqrt{(s = 200GeV)}$ was carried out by electron-hadron correlations at STAR, the vertical error bar and error band are represent the statistics and systematic uncertainty, respectively The Au+Au results are consistent with the PHENIX (grey band) measurements. and the p+p result are consistent with FONLL calculations.

4.5.4 Nuclear modification factors R_{AA} for D- and B-decayed electrons

The inclusive open heavy flavor decay electron (D- and B- mesons) nuclear modification factor (R_{AA}) was extracted in Au+Au collisions at $\sqrt{s_{NN}}$=200 GeV. The p+p reference from the previous analysis using data from Run 2012 as shown in Fig. 3.21, The Au+Au data is from STAR Run 2014, but without HFT. The inclusive non-photonic eletrons nuclear modification R_{AA}^{HF} shows on Fig. 4.26 [104], Both the Run 2014 and Run 2010 measurements are used the same Run 2012 p+p reference, two results are consistent with.

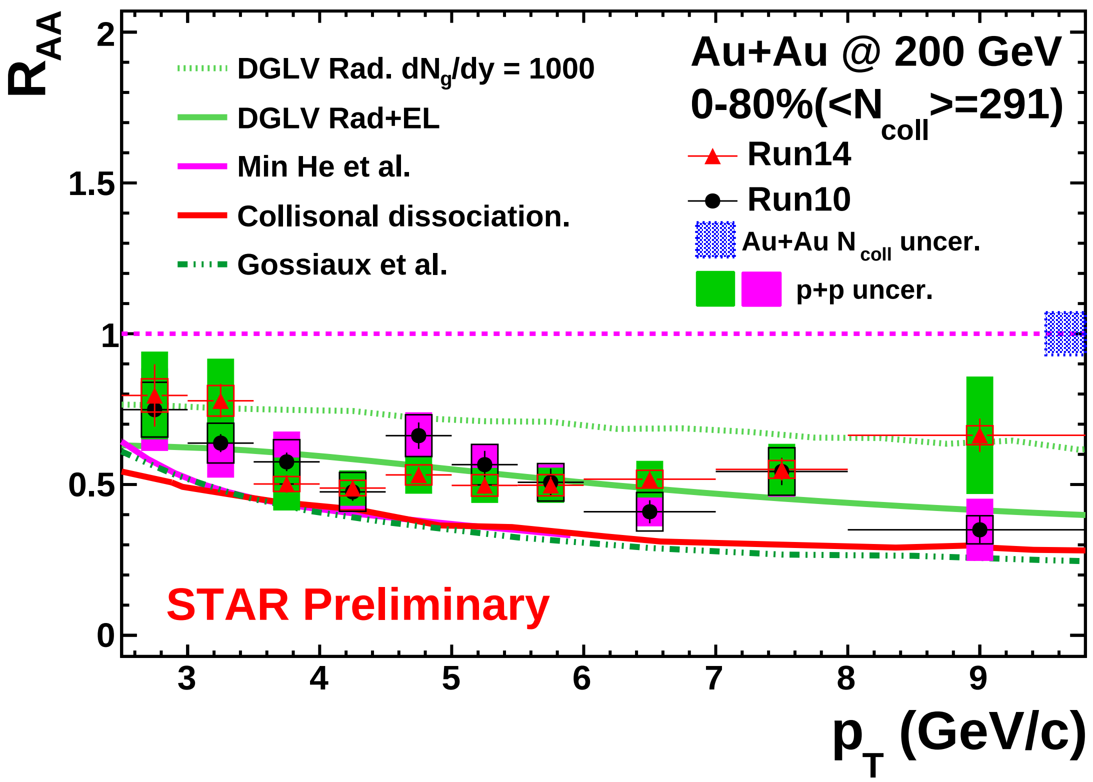

Fig. 4.26: Nuclear modification factor R_{AA} in Au+Au collisions at $\sqrt{s_{NN}}$=200 GeV for centrality 0-80% bin, the red triangle stand for the Run 2014 data, while the black point for the Run 2010 data. The measurements are compared with different model calculations.

The fraction of B-decayed electrons ($\frac{B\to e}{D\to e+B\to e}$) are obtained from the template fit.

Therefore, the nuclear modification factor $R_{AA}^{D\to e}$ and $R_{AA}^{B\to e}$ can be extracted using the Eq. 4.11 and 4.12, where F_{AuAu} and F_{pp} are the fractions of heavy flavor electrons from bottom hadron decays in Au+Au and p+p respectively and R_{AA}^{HF} are the inclusive open heavy flavor decay electron (D- and B- mesons) nuclear modification factor (R_{AA}). The result shows in Fig. 4.27.

$$R_{AA}^{D\to e} = \frac{(1 - F_{AuAu})}{(1 - F_{pp})} R_{AA}^{HF} \tag{4.11}$$

$$R_{AA}^{B\to e} = \frac{F_{AuAu}}{F_{pp}} R_{AA}^{HF} \tag{4.12}$$

This measurements suggest that less suppression for B-decayed electrons than D-decayed electrons, The $R_{AA}^{D\to e}$ suppression level is around 2 times of sigma lower than the $R_{AA}^{B\to e}$ and this measurements are compared with the DUKE model calculations, The measurements are consistent with Duke Model production [105], both measurements and model calculation are suggested the mass hirechy of parton energy loss $\Delta E_b < \Delta E_c$. In the model calculations, the in-medium energy loss of heavy quarks is described by the modified Langevin equation [81, 105]. During the heavy quarks propagate through a thermalized QCD mediums, they lose energy via both quasielastic scatterings with light patrons in the medium and gluon radiation induced by multiple scatterings. The expanding of the QGP medium is simulated by a (2+1)-dimensional viscous hydrodynamic model [?].

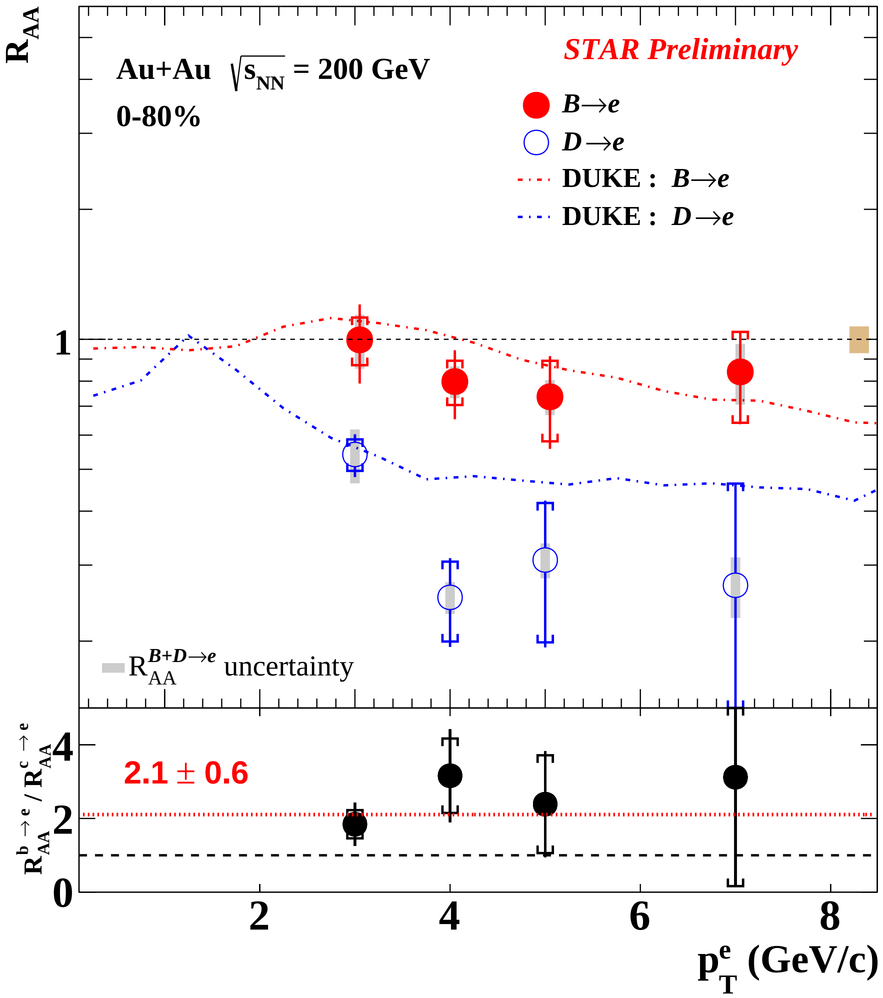

Fig. 4.27: Nuclear modification factors R_{AA} for D- and B-decayed electrons are obtained, suggesting less suppression for B-decayed electrons than D-decayed electrons and consistent with model calculations and mass hirechy of parton energy loss $\Delta E_b < \Delta E_c$.

CHAPTER 5

Summary and Outlook

5.1 Summary

In this thesis we present the measured NPE cross section in p+p collisions at $\sqrt{s}$=200 GeV using data from 2012, the results are compared to both the STAR's previous measurement using data from 2005 and 2008 and the perturbative Quantum Chromo-Dynamics (pQCD) Fixed-Order Next-to-Leading Logarithm (FONLL) calculation. This new measurement extends the p_{T} coverage to both lower and higher values than the previous STAR measurement, with significantly better precision. The new results confirmed the FONLL prediction and can also provide further constraints on such model calculations.

The nuclear modification factor R_{AA} was obtained in Au+Au collisions at $\sqrt{s_{NN}}$=200 GeV using the new, improved p+p reference. The R_{AA} was shown in different collision centrality intervals. The results show significant suppression at high p_{T} in the most central Au+Au collisions, and the suppression reduces gradually towards more peripheral collisions. The results also show an enhancement at low p_{T} across all collision centrality intervals, but with large systematic uncertainties. The measured R_{AA} in the 0-10% centrality interval is compared with different model calculations. The gluon radiation scenario (DGLV) model cannot describe the large suppression of NPE R_{AA} at high p_{T} . After adding the collisional energy loss, the model calculation is consistent with the data for p_T > 2.5 GeV/c. The collisional dissociation model, He et al., and the Gossiaux et al. models have some challenge to describe the data.

The Heavy Flavor Tracker (HFT) detector has been installed into STAR and taken data since 2014. The HFT provides excellent track impact parameter resolution, enabling separation of NPE from D and B mesons simi-leptonic decay. The fraction of B-decayed electrons ($\frac{B\to e}{D\to e+B\to e}$) was extracted from fitting track impact parameter DCA$_{XY}$ method. The B-decayed electrons fraction as a function of p_{T} has been shown at $\sqrt{s_{NN}}$=200 GeV in Au+Au collisions. The measurements are done at mid-rapidity ($|y|$ <0.7). The B-decayed electrons fraction result from this measurement have the similar trend with PHENIX result. The central value is higher than PHENIX results at higher p_{T} , but still consistent with PHENIX within uncertainty.

The inclusive NPE nuclear modification factor R_{AA} in Au+Au collisions at $\sqrt{s_{NN}}$=200 GeV is obtained. The fraction of B-decayed electrons in p+p collisions at $\sqrt{s}$=200 GeV was carried out by electron-hadron correlations at STAR, while the B decayed electrons in Au+Au collisions at $\sqrt{s_{NN}}$=200 GeV measured from this analysis. Therefore, The D- and B- mesons simi-leptonic decay $R_{AA}^{D\to e}$ and $R_{AA}^{B\to e}$ in Au+Au collisions at $\sqrt{s_{NN}}$ = 200 GeV can be calculated, respectively. The new measurement suggest that less suppression for B-decayed electrons than D-decayed electrons, it is consistent with the model calculations of mass hierarchy of parton energy loss $\Delta E_b < \Delta E_c$.

Currently, the measurements of NPE from D- and B- mesons simi-leptonic decay uncertainties is not good, particular at high p_{T} , but we have 5 more high-p_{T} electron triggered data were taken by the STAR experiment in Run 2016, which will significantly enhance the precision of the measurements on both bottom and charm productions.

5.2 Outlook

5.2.1 Detector upgrade proposals

The STAR will upgrade the HFT detector for preciser heavy flavor measurements. The projects proposed as HFT+, and the time scale will be in 2020+. The main upgrade for hardware is replaced the HFT sub-detector inner layer by the state-of-art MAPS pixels, which will allow the HFT to take the data with high luminosity. The new chips are being developed by both CERN and IPHC, and one of the designs will be used for

ALICE ITS upgrade which is planned for installation by the end of 2019. Most of the HFT existing infrastructure, including the carbon fiber structure, the air-cooling and the IST outer layer detectors will be reused. The new MAPS sensors have a much better radiation tolerance, which will allow for improving operation in the high 2020+ RHIC luminosities. Fig. 5.1 shows single pion track efficiency for HFT systems with different PXL integration times at a ZDC coincidence rate of 100k Hz. The upgrade HFT+ system with an integration time better than 40 μs will have a significant increase in tracking efficiency, for example 50% (18%) increase for 0.5 (2) GeV/c pions. [106].

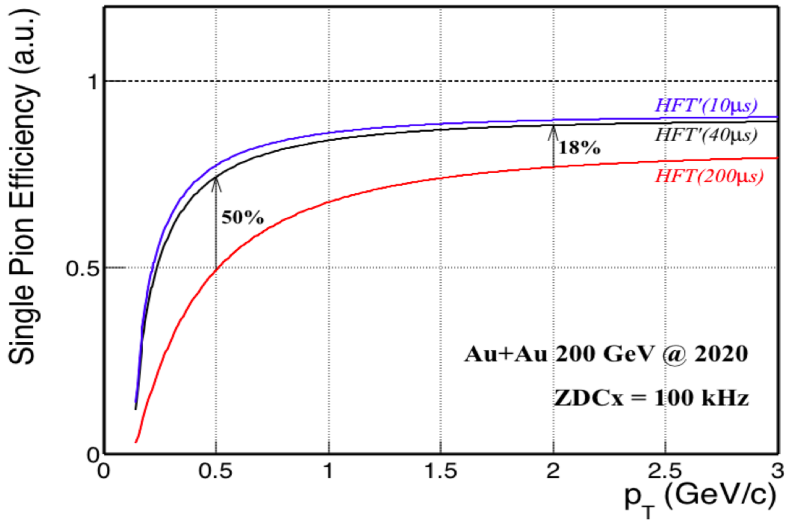

Fig. 5.1: The single π efficiency for HFT systems with different PXL integration times of 200(red), 40(black), 10(blue) μs, respectively at a ZDC coincidence rate of 100k Hz.

5.2.2 Future measurements

Both recent model calculation and experiments results are suggested that the strong interactions between heavy quarks the medium are different with light quarks, since different mass. In this thesis, the measurement of the D- and B- mesons simi-leptonic decay $R_{AA}^{D\to e}$ and $R_{AA}^{B\to e}$ in Au+Au collisions at $\sqrt{s_{NN}}$ = 200 GeV, indicated that the B-decayed electrons $R_{AA}^{B\to e}$ is higher than the D-decayed electrons. This result is consistent with model calculations and mass hirechy of parton energy loss $\Delta E_b < \Delta E_c$. Therefor, precise measurements of charm and bottom quark production separately in heavy-ions collisions is crucial for understanding the flavor dependent parton energy loss mechanism, and improve our understanding of the properties of the QGP.

The HFT detector has been installed into STAR and taken data since 2014, there are a lot of exciting results have been carried out by HFT. It is the first time topological reconstructed the D^0, and measured its azimuthal anisotropy at RHIC, a measurement that will help constrain the QGP transport coefficients. It is the first time reconstructed the Λ_c in the heavy-ions collision. Particularly, the HFT fist time enabling the measurement of the non-prompt D^0 and non-prompt $J\psi$, which if are from the B hadron decay. Fig. 5.2 shows the productions of bottom quarks by the J/ψ, D^0 and electron decay channels (this analysis) in Au+Au collisions at $\sqrt{s_{NN}}$ = 200 GeV with STAR. The strong suppression for $J\psi$, D^0 are from B hadron decays. However, Both two measurements are with large uncertainties, therefore, more statistics is expected for the precise measurements.

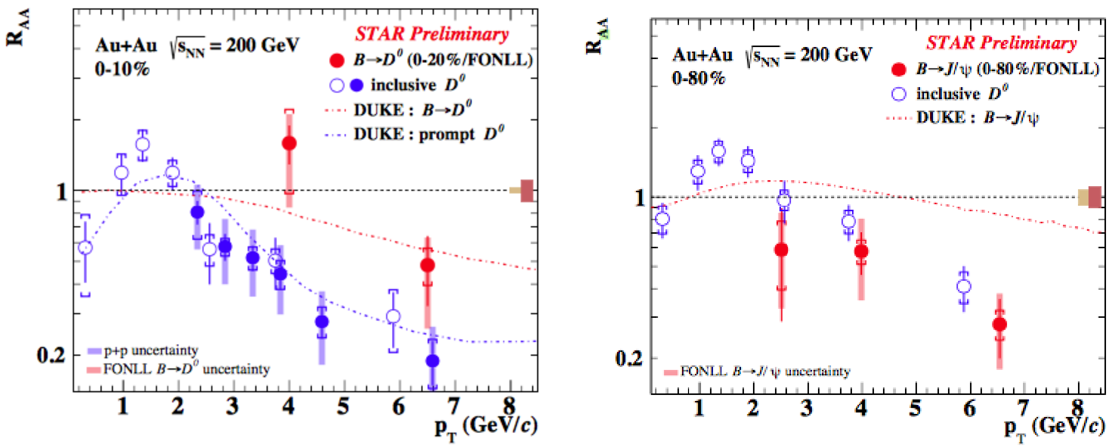

Fig. 5.2: Left panel shows the nuclear modification factor R_{AA} of non-prompt D^0 and inclusive D^0 as a function of p_{T} in Au+Au collisions at $\sqrt{s_{NN}}$ = 200 GeV. Right panel shows the nuclear modification factor R_{AA} of non-prompt J/ψ and inclusive D^0 as a function of p_{T} in 0-80% Au+Au collisions at $\sqrt{s_{NN}}$ = 200 GeV.

It has been discussed that STAR proposed to upgrade the current HFT detector to HFT+ 5.2.1, HFT+ will significant increase in tracking efficiency. Fig. 5.3 shows the simulation of the expected statistical error on the nuclear modification factor R_{AA} for non-prompt J/ψ (top left) and D^0 (bottom left) from the bottom hadron decays. By comparing the HFT measurement and HFT+ simulation. The HFT+ measurements are more preciser than the currently HFT results, and the p_{T} range is much higher than HFT, the HFT+ can measure the bottom quark tagged jets, and the expected p_{T} up to 40 GeV/c, all the simulation compared with model calculations from theory model calculations from TAMU, Duke, and CUJET3.0 [80, 105, 107], therefore, the HFT+ can make a big difference in the B measurement, and the precise measurements from HFT+ can be expected.

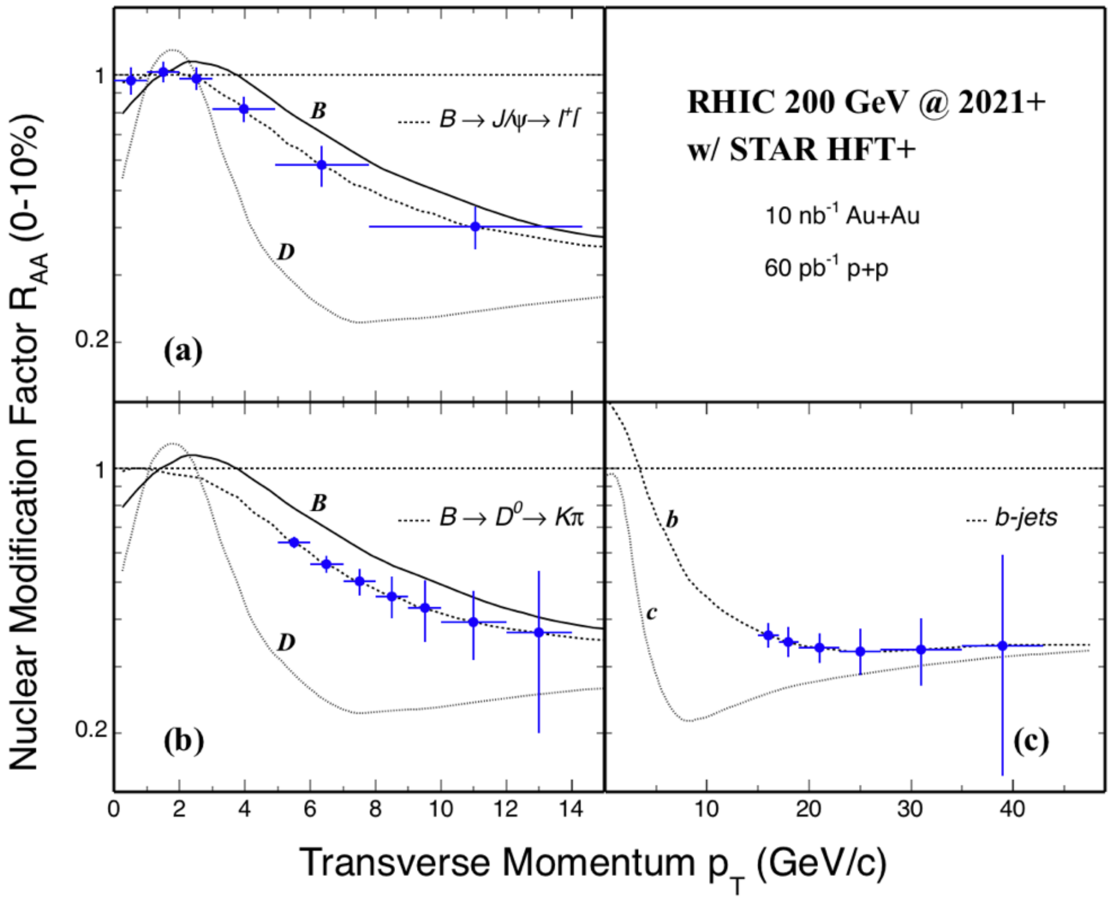

Fig. 5.3: Statistical error projection for R_{AA} in 0-10% Au+Au 200 GeV collisions for (a) J/Ψ , (b) D^0 from beauty decays and (c) b-tagged jets with data collected by the HFT+.

References

[1] M. Gell-mann. A schematic model of baryons and mesons. *Phys. Lett.*, 8:214–215, 1964.

[2] G Zweig. An SU_3 model for strong interaction symmetry and its breaking; Version 1. Technical Report CERN-TH-401, CERN, Geneva, 1964.

[3] H. David Politzer. Asymptotic Freedom: An Approach to Strong Interactions. *Phys.Rept.*, 14:129–180, 1974.

[4] Reinhard Stock. The QCD Phase Diagram: Expectations and Challenges. *PoS*, CPOD2009:001, 2009.

[5] S. Bethke. Experimental tests of asymptotic freedom. *Progress in Particle and Nuclear Physics*, 58(2):351 – 386, 2007.

[6] L.N. Lipatov. The parton model and perturbation theory. *Sov.J.Nucl.Phys.*, 20:94–102, 1975.

[7] George Sterman, John Smith, John C. Collins, James Whitmore, Raymond Brock, Joey Huston, Jon Pumplin, Wu-Ki Tung, Hendrik Weerts, Chien-Peng Yuan, Stephen Kuhlmann, Sanjib Mishra, Jorge G. Morfín, Fredrick Olness, Joseph Owens, Jianwei Qiu, and Davison E. Soper. Handbook of perturbative qcd. *Rev. Mod. Phys.*, 67:157–248, 1995.

[8] Abulencia. and others (CDF Collaboration). Measurement of the inclusive jet cross section in $p\overline{p}$ interactions at $\sqrt{s} = 1.96$ TeV using a cone-based jet algorithm. *Phys. Rev. D*, 74:071103, 2006.

[9] T. Aaltonen et al. Measurement of the Inclusive Jet Cross Section at the Fermilab Tevatron p anti-p Collider Using a Cone-Based Jet Algorithm. *Phys. Rev.*, D78:052006, 2008. [Erratum: Phys. Rev.D79,119902(2009)].

[10] J. C. Collins and M. J. Perry. Superdense matter: Neutrons or asymptotically free quarks? *Phys. Rev. Lett.*, 34:1353–1356, 1975.

[11] John Adams et al. Experimental and theoretical challenges in the search for the quark gluon plasma: The STAR Collaboration's critical assessment of the evidence from RHIC collisions. *Nucl. Phys.*, A757:102–183, 2005.

[12] G. F. Burgio, M. Baldo, P. K. Sahu, and H.-J. Schulze. Hadron-quark phase transition in dense matter and neutron stars. *Phys. Rev. C*, 66:025802, 2002.

[13] M. A. Stephanov. QCD phase diagram: An Overview. *PoS*, LAT2006:024, 2006.

[14] Carleton E DeTar and John F Donoghue. Bag models of hadrons. *Annual Review of Nuclear and Particle Science*, 33(1):235–264, 1983.

[15] M J Tannenbaum. Recent results in relativistic heavy ion collisions: from 'a new state of matter' to 'the perfect fluid'. *Reports on Progress in Physics*, 69(7):2005, 2006.

[16] T D Lee and G C Wick. Vacuum stability and vacuum excitation in a spin-0 field theory. *Physical Review D*, 9(8):2291, 1974.

[17] H H Gutbrod, A M Poskanzer, and H G Ritter. Plastic ball experiments. *Reports on Progress in Physics*, 52(10):1267, 1989.

[18] Hans H Gutbrod, Arthur M Poskanzer, and Hans Georg Ritter. Plastic ball experiments. *Reports on Progress in Physics*, 52(10):1267, 1989.

[19] J. Adams et al. Experimental and theoretical challenges in the search for the quarkgluon plasma: The STAR collaboration's critical assessment of the evidence from rhic collisions. *Nuclear Physics A*, 757(1):102 – 183, 2005.

[20] K. Adcox et al. Formation of dense partonic matter in relativistic nucleusnucleus collisions at rhic: Experimental evaluation by the phenix collaboration. *Nuclear Physics A*, 757(1):184 – 283, 2005.

[21] Frithjof Karsch. Lattice results on QCD thermodynamics. *Nucl. Phys.*, A698:199–208, 2002.

[22] F. Karsch. Lattice QCD at high temperature and density. *Lect. Notes Phys.*, 583:209–249, 2002.

[23] Adams. et al. Evidence from $d+\mathrm{Au}$ measurements for final-state suppression of high-p_T hadrons in $\mathrm{Au}+\mathrm{Au}$ collisions at rhic. *Phys. Rev. Lett.*, 91:072304, 2003.

[24] Adler et al. Disappearance of back-to-back high-p_T hadron correlations in central $\mathrm{Au}+\mathrm{Au}$ collisions at $\sqrt{s_{NN}} = 200$ GeV. *Phys. Rev. Lett.*, 90:082302, 2003.

[25] Michael L Miller, Klaus Reygers, Stephen J Sanders, and Peter Steinberg. Glauber modeling in high-energy nuclear collisions. *Annu. Rev. Nucl. Part. Sci.*, 57:205–243, 2007.

[26] B Alver and G Roland. Collision-geometry fluctuations and triangular flow in heavy-ion collisions. *Physical Review C*, 81(5):054905, 2010.

[27] BI Abelev, MM Aggarwal, Z Ahammed, BD Anderson, D Arkhipkin, GS Averichev, Y Bai, J Balewski, O Barannikova, LS Barnby, et al. Systematic measurements of identified particle spectra in pp, d+ au, and au+ au collisions at the STAR detector. *Physical Review C*, 79(3):034909, 2009.

[28] A. M. Poskanzer and S. A. Voloshin. Methods for analyzing anisotropic flow in relativistic nuclear collisions. *Phys. Rev. C*, 58:1671–1678, 1998.

[29] Adler. et al. Elliptic flow of identified hadrons in $\mathrm{Au}+\mathrm{Au}$ collisions at $\sqrt{s_{NN}} = 200$ GeV. *Phys. Rev. Lett.*, 91:182301, 2003.

[30] Pasi Huovinen, Peter F Kolb, Ulrich Heinz, PV Ruuskanen, and Sergei A Voloshin. Radial and elliptic flow at rhic: further predictions. *Physics Letters B*, 503(1):58–64, 2001.

[31] Denes Molnar and Sergei A Voloshin. Elliptic flow at large transverse momenta from quark coalescence. *Physical review letters*, 91(9):092301, 2003.

[32] Stephen Scott Adler, S Afanasiev, C Aidala, NN Ajitanand, Y Akiba, J Alexander, R Amirikas, L Aphecetche, SH Aronson, R Averbeck, et al. Single electrons from heavy-flavor decays in $p+p$ collisions at $\sqrt{s} = 200$ GeV. *Physical review letters*, 96(3):032001, 2006.

[33] Matteo Cacciari, Paolo Nason, and Ramona Vogt. Qcd predictions for charm and bottom quark production at rhic. *Phys. Rev. Lett.*, 95:122001, 2005.

[34] Adamczyk et al. Measurements of D^0 and D^* production in p+p collisions at $\sqrt{s}$=200 GeV. *Phys. Rev. D*, 86:072013, 2012.

[35] C. Amsler, M. Doser, et al. Review of particle physics. *Physics Letters B*, 667(15):1 – 6, 2008. Review of Particle Physics.

[36] John Adams, MM Aggarwal, Z Ahammed, J Amonett, BD Anderson, D Arkhipkin, GS Averichev, SK Badyal, Y Bai, J Balewski, et al. Open charm yields in $d + au$ collisions at $\sqrt{s} = 200$ GeV. *Physical review letters*, 94(6):062301, 2005.

[37] Adamczyk L. and et al. Observation of D^0 meson nuclear modifications in Au+Au collisions at $\sqrt{s_{\rm NN}} = 200$ GeV. *Phys. Rev. Lett.*, 113:142301, 2014.

[38] Abelev et al. Identified baryon and meson distributions at large transverse momenta from Au + Au collisions at $\sqrt{s_{NN}} = 200$ GeV. *Phys. Rev. Lett.*, 97:152301, 2006.

[39] Abelev. et al. Transverse momentum and centrality dependence of high-p_T nonphotonic electron suppression in Au + Au collisions at $\sqrt{s_{\rm NN}} = 200$ GeV. *Phys. Rev. Lett.*, 98:192301, 2007.

[40] Agakishiev. and others (STAR Collaboration). High p_T nonphotonic electron production in $p+p$ collisions at $\sqrt{s} = 200$ GeV. *Phys. Rev. D*, 83:052006, 2011.

[41] Adare. et al. Measurement of high-p_T single electrons from heavy-flavor decays in $p+p$ collisions at $\sqrt{s} = 200$ GeV. *Phys. Rev. Lett.*, 97:252002, 2006.

[42] Magdalena Djordjevic, Miklos Gyulassy, Ramona Vogt, and Simon Wicks. Influence of bottom quark jet quenching on single electron tomography of au+ au. *Physics Letters B*, 632(1):81–86, 2006.

[43] Néstor Armesto, Matteo Cacciari, Andrea Dainese, Carlos A Salgado, and Urs Achim Wiedemann. How sensitive are high-pt electron spectra at rhic to heavy quark energy loss? *Physics Letters B*, 637(6):362–366, 2006.

[44] Adamczyk. et al. Elliptic flow of electrons from heavy-flavor hadron decays in au + au collisions at $\sqrt{s_{NN}}$ = 200, 62.4, and 39 GeV. *Phys. Rev. C*, 95:034907, 2017.

[45] Aggarwal. et al. Measurement of the bottom quark contribution to nonphotonic electron production in $p+p$ collisions at $\sqrt{s}$ = 200 GeV. *Phys. Rev. Lett.*, 105:202301, 2010.

[46] Jan Uphoff, Oliver Fochler, Zhe Xu, and Carsten Greiner. Elliptic flow and energy loss of heavy quarks in ultrarelativistic heavy ion collisions. *Phys. Rev. C*, 84:024908, 2011.

[47] Jan Uphoff, Oliver Fochler, Zhe Xu, and Carsten Greiner. Open heavy flavor in pb + pb collisions at within a transport model. *Physics Letters B*, 717(45):430 – 435, 2012.

[48] Adare. Heavy-quark production in $p + p$ and energy loss and flow of heavy quarks in au + au collisions at $\sqrt{s_{NN}}$ = 200 GeV. *Phys. Rev. C*, 84:044905, 2011.

[49] Hendrik van Hees, Vincenzo Greco, and Ralf Rapp. Heavy-quark probes of the quark-gluon plasma and interpretation of recent data taken at the bnl relativistic heavy ion collider. *Phys. Rev. C*, 73:034913, 2006.

[50] M. Harrison, T. Ludlam, and S. Ozaki. RHIC project overview. *Nuclear Instruments and Methods in Physics Research Section A: Accelerators, Spectrometers, Detectors and Associated Equipment*, 499(23):235 – 244, 2003. The Relativistic Heavy Ion Collider Project: RHIC and its Detectors.

[51] The rhic accelerator. *Annual Review of Nuclear and Particle Science*, 52(1):425–469, 2002.

[52] Vadim Ptitsyn, Peter D Barnes, Martin D Cooper, Robert A Eisenstein, Hubert van Hecke, and Gerard J Stephenson. erhic—future electron-ion collider at bnl. In *AIP Conference Proceedings*, volume 842, pages 1046–1048. AIP, 2006.

[53] E. C. Aschenauer et al. The RHIC Spin Program: Achievements and Future Opportunities. 2013.

[54] K.H. Ackermann, , et al. STAR detector overview. *Nuclear Instruments and Methods in Physics Research Section A: Accelerators, Spectrometers, Detectors and Associated Equipment*, 499(23):624 – 632, 2003. The Relativistic Heavy Ion Collider Project: RHIC and its Detectors.

[55] M. Anderson, , et al. The STAR time projection chamber: a unique tool for studying high multiplicity events at RHIC. *Nuclear Instruments and Methods in Physics Research Section A: Accelerators, Spectrometers, Detectors and Associated Equipment*, 499(23):659 – 678, 2003. The Relativistic Heavy Ion Collider Project: RHIC and its Detectors.

[56] Hao Qiu, STAR Collaboration, et al. STAR heavy flavor tracker. *Nuclear Physics A*, 931:1141–1146, 2014.

[57] D Beavis et al. The STAR heavy flavor tracker technical design report. 2011.

[58] Hao Qiu, STAR Collaboration, et al. Open charm hadron measurements at STAR. *Nuclear and Particle Physics Proceedings*, 276:213–216, 2016.

[59] Amilkar Quintero. *Measurements of charm meson production in Au+Au collisions at* $\sqrt{s} = 200$ GeV. PhD thesis, Kent State University, 2016.

[60] Yifei Zhang, Jonathan Bouchet, Xin Dong, Spyridon Margetis, and Hans Georg Ritter. Study of bottom production with the STAR heavy flavor tracker. *Journal of Physics G: Nuclear and Particle Physics*, 41(2):025103, 2014.

[61] L. Adamczyk et al. Measurement of D^0 azimuthal anisotropy at mid-rapidity in Au+Au collisions at $\sqrt{s_{NN}} = 200$ GeV. 2017.

[62] KH Ackermann, N Adams, C Adler, M Aluyshin, MA Ananeva, M Anderson, G Averichev, A Bacher, J Balewski, O Balrannikova, et al. The STAR time projection chamber. *Nuclear Physics A*, 661(1-4):681–685, 1999.

[63] M. Anderson et al. The Star time projection chamber: A Unique tool for studying high multiplicity events at RHIC. *Nucl. Instrum. Meth.*, A499:659–678, 2003.

[64] M Anderson, J Berkovitz, W Betts, R Bossingham, F Bieser, R Brown, M Burks, M Calderón de la Barca Sánchez, D Cebra, M Cherney, et al. The STAR time projection chamber: a unique tool for studying high multiplicity events at rhic. *Nuclear Instruments and Methods in Physics Research Section A: Accelerators, Spectrometers, Detectors and Associated Equipment*, 499(2):659–678, 2003.

[65] F Bergsma, CO Blyth, RL Brown, W Dieffenbach, A Etkin, KJ Foley, P-A Giudici, WJ Leonhardt, W Love, JA Mills, et al. The STAR detector magnet subsystem. *Nuclear Instruments and Methods in Physics Research Section A: Accelerators, Spectrometers, Detectors and Associated Equipment*, 499(2):633–639, 2003.

[66] Hans Bichsel. A method to improve tracking and particle identification in {TPCs} and silicon detectors. *Nuclear Instruments and Methods in Physics Research Section A: Accelerators, Spectrometers, Detectors and Associated Equipment*, 562(1):154 – 197, 2006.

[67] WJ Llope, STAR Collaboration, et al. Multigap rpcs in the STAR experiment at rhic. *Nuclear Instruments and Methods in Physics Research Section A: Accelerators, Spectrometers, Detectors and Associated Equipment*, 661:S110–S113, 2012.

[68] WJ Llope, STAR TOF Group, et al. The large-area time-of-flight upgrade for STAR. *Nuclear Instruments and Methods in Physics Research Section B: Beam Interactions with Materials and Atoms*, 241(1):306–310, 2005.

[69] WJ Llope, F Geurts, JW Mitchell, Z Liu, N Adams, G Eppley, D Keane, J Li, F Liu, L Liu, et al. The tofp/pvpd time-of-flight system for STAR. *Nuclear Instruments and Methods in Physics Research Section A: Accelerators, Spectrometers, Detectors and Associated Equipment*, 522(3):252–273, 2004.

[70] W. J. Llope et al. The STAR Vertex Position Detector. *Nucl. Instrum. Meth.*, A759:23–28, 2014.

[71] M. Beddo, , et al. The STAR barrel electromagnetic calorimeter. *Nuclear Instruments and Methods in Physics Research Section A: Accelerators, Spectrometers, Detectors and Associated Equipment*, 499(23):725 – 739, 2003. The Relativistic Heavy Ion Collider Project: RHIC and its Detectors.

[72] Lawrence D Brown, T Tony Cai, and Anirban DasGupta. Interval estimation for a binomial proportion. *Statistical science*, pages 101–117, 2001.

[73] A. Adare et al. Heavy Quark Production in $p+p$ and Energy Loss and Flow of Heavy Quarks in Au+Au Collisions at $\sqrt{s_{NN}} = 200$ GeV. *Phys. Rev.*, C84:044905, 2011.

[74] Adare. and others (PHENIX Collaboration). Transverse momentum dependence of j/ψ polarization at midrapidity in $p+p$ collisions at $\sqrt{s} = 200$ GeV. *Phys. Rev. D*, 82:012001, 2010.

[75] Abelev. and others (STAR Collaboration). j/ψ. *Phys. Rev. C*, 80:041902, 2009.

[76] R. E. Nelson, R. Vogt, and A. D. Frawley. Narrowing the uncertainty on the total charm cross section and its effect on the j/ψ cross section. *Phys. Rev. C*, 87:014908, 2013.

[77] Xiaozhi Bai. Measurements of open heavy flavor production in semi-leptonic channels at STAR. *Nuclear Physics A*, 956:513 – 516, 2016.

[78] Magdalena Djordjevic, Miklos Gyulassy, Ramona Vogt, and Simon Wicks. Influence of bottom quark jet quenching on single electron tomography of au + au. *Physics Letters B*, 632(1):81 – 86, 2006.

[79] Rishi Sharma, Ivan Vitev, and Ben-Wei Zhang. Light-cone wave function approach to open heavy flavor dynamics in qcd matter. *Phys. Rev. C*, 80:054902, 2009.

[80] Min He, Rainer J. Fries, and Ralf Rapp. Heavy-quark diffusion and hadronization in quark-gluon plasma. *Phys. Rev. C*, 86:014903, 2012.

[81] Shanshan Cao, Guang-You Qin, and Steffen A. Bass. Heavy-quark dynamics and hadronization in ultrarelativistic heavy-ion collisions: Collisional versus radiative energy loss. *Phys. Rev. C*, 88:044907, 2013.

[82] P B Gossiaux, J Aichelin, T Gousset, and V Guiho. Competition of heavy quark radiative and collisional energy loss in deconfined matter. *Journal of Physics G: Nuclear and Particle Physics*, 37(9):094019, 2010.

[83] P. B. Gossiaux and J. Aichelin. Toward an understanding of the single electron data measured at the bnl relativistic heavy ion collider. *Phys. Rev. C*, 78:014904, 2008.

[84] J. Aichelin, P. B. Gossiaux, and T. Gousset. Radiative and Collisional Energy Loss of Heavy Quarks in Deconfined Matter. *Acta Phys. Polon.*, B43:655–662, 2012.

[85] Alessandro Buzzatti and Miklos Gyulassy. Jet flavor tomography of quark gluon plasmas at rhic and lhc. *Phys. Rev. Lett.*, 108:022301, 2012.

[86] Yichun Xu, Olga Barannikova, Hans Bichsel, Xin Dong, Patricia Fachini, Yuri Fisyak, Adam Kocoloski, Bedanga Mohanty, Pawan Netrakanti, Lijuan Ruan, Maria Cristina Suarez, Zebo Tang, Gene van Buren, and Zhangbu Xu. Improving the calibration of the STAR {TPC} for the high- hadron identification. *Nuclear Instruments and Methods in Physics Research Section A: Accelerators, Spectrometers, Detectors and Associated Equipment*, 614(1):28 – 33, 2010.

[87] David J. Lange. The evtgen particle decay simulation package. *Nuclear Instruments and Methods in Physics Research Section A: Accelerators, Spectrometers, Detectors and Associated Equipment*, 462(12):152 – 155, 2001. BEAUTY2000, Proceedings of the 7th Int. Conf. on B-Physics at Hadron Machines.

[88] Marina Artuso, Elisabetta Barberio, and Sheldon Stone. B meson decays. *PMC Physics A*, 3(1):3, 2009.

[89] Zhenyu Ye. Implement evtgen into STAR experiment. *STAR collaboration internal documentation.*

[90] S. Agostinelli. et al. Geant4—a simulation toolkit. *Nuclear Instruments and Methods in Physics Research Section A: Accelerators, Spectrometers, Detectors and Associated Equipment*, 506(3):250 – 303, 2003.

[91] J. Allison. et al. Geant4 developments and applications. *IEEE Transactions on Nuclear Science*, 53(1):270–278, 2006.

[92] J. Allison. et al. Recent developments in geant4. *Nuclear Instruments and Methods in Physics Research Section A: Accelerators, Spectrometers, Detectors and Associated Equipment*, 835:186 – 225, 2016.

[93] The STAR simulation framework. *STAR internal document.*

[94] Mykhailo Lisovyi, Andrii Verbytskyi, and Oleksandr Zenaiev. Combined analysis of charm-quark fragmentation-fraction measurements. *Eur. Phys. J.*, C76(7):397, 2016.

[95] H. Akopian Abe, F. Akimoto and et al. Observation of the B_c meson in $p\overline{p}$ collisions at $\sqrt{s} = 1.8$ TeV. *Phys. Rev. Lett.*, 81:2432–2437, 1998.

[96] Marco Masetti and Francesca Sartogo. Perturbative predictions for bc meson production in hadronic collisions. *Physics Letters B*, 357(4):659 – 665, 1995.

[97] M. Kreps and Y. Kwon. production and decay of b-flavored hadrons. *Particle Data Group.*

[98] Centrality dependence of low-momentum direct-photon production in Au + Au collisions at $\sqrt{s_{NN}} = 200$GeV. *Phys. Rev. C*, 91:064904, 2015.

[99] Xin-Nian Wang and Miklos Gyulassy. hijing. *Phys. Rev. D*, 44:3501–3516, 1991.

[100] Xin-Nian Wang and Miklos Gyulassy. Gluon shadowing and jet quenching in a+a collisions at $\sqrt{\mathrm{s}}$ =200 GeV. *Phys. Rev. Lett.*, 68:1480–1483, 1992.

[101] Xin-Nian Wang and Miklos Gyulassy. Systematic study of particle production in p+ p (p$^-$) collisions via the hijing model. *Physical Review D*, 45(3):844, 1992.

[102] William Templeton Eadie, Daniel Drijard, and Frederick E James. Statistical methods in experimental physics. *Amsterdam: North-Holland, 1971*, 1971.

[103] A. Adare et al. Single electron yields from semileptonic charm and bottom hadron decays in Au + Au collisions at $\sqrt{s_{NN}} = 200$ GeV. *Phys. Rev. C*, 93:034904, 2016.

[104] Zhang Shenghui. Measurements of electron production from open heavy flavor decays in Au+Au collisions at $\sqrt{s_{NN}} = 200$ GeV by the STAR experiment. *Quark Matter 2017 Poster.*

[105] Shanshan Cao, Guang-You Qin, and Steffen A. Bass. Energy loss, hadronization, and hadronic interactions of heavy flavors in relativistic heavy-ion collisions. *Phys. Rev. C*, 92:024907, 2015.

[106] STAR Collaboration. Physics opportunities with STAR in 2020+. *STAR internal documentaion*, 2015.

[107] Jiechen Xu, Jinfeng Liao, and Miklos Gyulassy. Long wavelength perfect fluidity from short distance jet transport in quarkgluon plasmas. *Nuclear Physics A*, 956:617 – 620, 2016.

Presentations and publication List

Presentations

1. Sep. 2015, Measurements of Open Heavy Flavor Production in Semi-leptonic Channels in p+p, U+U and Au+Au collisions at STAR, **Oral presentation, Quark Matter**, Kobe Fashion, Kobe, Japan

2. Apr. 2015, Non-photonic electron production in p+p collisions at $\sqrt{s}$=200 GeV, **Oral presentation, American Physical Society April Meeting**, Baltimore, MD, USA

3. May 2014, High-p_{T} non-photonic electron production in p+p collisions at $\sqrt{s}$=200 GeV, **Poster presentation, Quark Matter**, Darmstadtium, Darmstadt, Germany

4. Sep. 2015, Measurements of electrons from semileptonic decays of open heavy flavor hadrons in p+p and Au+Au collisions at $\sqrt{s_{NN}}$=200 GeV, **Poster presentation, Quark Matter**, Kobe Fashion, Kobe, Japan

5. Jul. 2012, Measurements of charm and bottom production via semi-leptonic decays in Au+Au collisions at $\sqrt{s_{NN}}$ GeV by the STAR experiment **Poster presentation, Quark Matter**, Chicago, IL, USA

Publication list

1. **X. Bai**, Measurements of Open Heavy Flavor Production in Semi-leptonic Channels in p+p, U+U and Au+Au collisions at STAR,
Nuclear Physics A **956**, 513516 (2016)

2. **X. Bai**, C. B. Yang, Influence of long-range correlation on the scaling properties of the normalized factorial correlators in relativistic heavy-ion collisions.
International Journal of Modern Physics E, **22**, 1350059 (2013)

3. **X. Bai**, *et al*, Measurements of electron production from heavy flavor hadron decays in p+p and Au+Au collisions at 200 GeV,
   Targeted Journal: Phys. Rev. C, (Currently in STAR heavy flavor PWG)

4. **X. Bai**, Bingchu Huang, Zhenyu Ye, J/ψ cross section and event activities in p+p at 200 GeV at STAR,
   Targeted Journal: Physics Letter B, (Currently in STAR GPC)

Selected STAR Collaboration Publication list

1. Charge-dependent directed flow in Cu+Au collisions at $\sqrt{s_{NN}} = 200$ GeV,
   L. Adamczyk *et al.* (STAR Collaboration) Phys. Rev. Lett. **118**, 12301 (2017)

2. Upsilon production in U+U collisions at $\sqrt{s_{NN}}$=193 GeV with the STAR experiment,
   L. Adamczyk *et al.* (STAR Collaboration) Phys. Rev. C **94**, 64904 (2016)

3. Jet-like Correlations with Direct-Photon and Neutral-Pion Triggers at $\sqrt{s_{NN}}$=200 GeV,
   L. Adamczyk *et al.* (STAR Collaboration) Phys. Lett. B **760**, 689 (2016)

4. Near-side azimuthal and pseudorapidity correlations using neutral strange baryons and mesons in d+Au, Cu+Cu and Au+Au collisions at $\sqrt{s_{NN}}$=200GeV,
   L. Adamczyk *et al.* (STAR Collaboration) Phys. Rev. C **94**, 14910 (2016)

5. J/psi production at low transverse momentum in p+p and d+Au collisions at $\sqrt{s_{NN}}$=200 GeV,
   L. Adamczyk *et al.* (STAR Collaboration) Phys. Rev. C **93**, 64904 (2016)

6. Measurement of elliptic flow of light nuclei at $\sqrt{s_{NN}}$= 200, 62.4, 39, 27, 19.6, 11.5, and 7.7 GeV at RHIC,
   L. Adamczyk *et al.* (STAR Collaboration) Phys. Rev. C **94**, 34908 (2016)

7. Beam Energy Dependence of the Third Harmonic of Azimuthal Correlations in

Au+Au Collisions at RHIC

L. Adamczyk *et al*. (STAR Collaboration) Phys. Rev. Lett. **116**, 112302 (2016)

8. Measurement of the transverse single-spin asymmetry in p+p → W±/Z0 at RHIC, L. Adamczyk *et al*. (STAR Collaboration) Phys. Rev. Lett. **116**, 132301(2016)

9. Centrality dependence of identified particle elliptic flow in relativistic heavy ion collisions at $\sqrt{s_{NN}}$= 7.7-62.4 GeV,
L. Adamczyk *et al*. (STAR Collaboration) Phys. Rev. C **93**, 14907(2016)

Acknowledge

This thesis includes many efforts and contributions from whom helped and worked with me. It is impossible that I can finish this project if without your support and help. I would never forget you.

Firstly, I would like to express my deepest gratitude to my supervisor Prof. Chunbin Yang and Prof. Zhenyu Ye. Chunbing introduced me to the high energy physics, especially gave me the opportunities and resources to work with Prof. Zhenyu Ye at UIC, who is working at the STAR experiment. In particular thanks Prof. Zhenyu who supervised me in my data analysis and thesis, and support me almost four years working at UIC. He gave me a very good starting on the experiment high energy physics and continue to supervise me to finish my analysis, helped me a lot not only in my research but also living in the US. I would like to thank Prof. Yaping Wang for many helpful suggestions and discussions for my thesis, supporting me to many conferences when i was in UIC in the last two years.

I would like to thank the STAR collaboration and Heavy Flavor physics working group especially the conveners. I would like to thank Prof. Nu Xu, Dr. Zhangbu Xu, Dr. Xin Dong for many helpful suggestions and discussions.

I would especially thank Dr. Mustafa, Bingchu Huang, and Zach miller, helped me on the data analysis in details, and the graduate students Guanglei Li, Zefang Jiang, Pengfei Xu, Zaochen Ye, Siwei Luo, Shenghui Zhang, and all of you helped me not only in research but also in life, thanks all of you, we are together at CCNU and UIC in last 6 years, I would never forget all of you.

Finally, I would like to give my deep gratitude to my family for their love and always support in my life. I'll never forget tens of years of sacrifices from my parents, I would not be where I am today if without them. My special thanks goes to my wife Shan Lin, who continuous understanding and encouraging me to overcome the challenges in the life, especially will give a baby, it is really a surprise to me.